Non-destructive measurement of internal fruit quality using SQUID-NMR techniques

by

Jean Frederic Isingizwe Nturambirwe

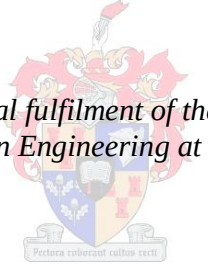

Thesis presented in partial fulfilment of the requirements for the degree Master of Science in Engineering at Stellenbosch University

Supervisors: Prof. W.J. Perold — Department of Electrical & Electronic Engineering
Prof. L.Opara — Department of Horticultural Science

December 2012

Declaration

By submitting this thesis electronically, I declare that the work contained therein is my own, original work, that I am the sole author thereof (save to the extent explicitly otherwise stated), that reproduction and publication thereof by Stellenbosch University will not infringe any third party rights and that I have not previously in its entirety or in part submitted it for any qualification.

Date: December 2012

Abstract

Non-destructive measurement of internal fruit quality using SQUID-NMR techniques.

J.F. ISINGIZWE NTURAMBIRWE

Department of Electrical and Electronics Engineering,
University of Stellenbosch
Private Bag X1, Matieland 7602, South Africa.

Thesis: MScEng (Electrical and Electronic Engineering)

December 2012

The SQUID-NMR technique has been increasingly recommended by many researchers as holding a lot of potential, and it is believed it will become an invaluable tool for non-destructive evaluation in the future. Most of its potential is yet to be exploited. Non-destructive quality control of food products is one of the applications where such a system is being tried.

Much of the progress that has been made in improving such a system to the present degree of user friendliness and cost effectiveness shows that, with more effort, it would be possible to implement the technology for on-line sorting, and possibly to reduce it down to hand-held devices.

The goal was to investigate the feasibility of the internal fruit quality measurements using the NMR technique, and to develop a SQUID system suitable for SQUID-NMR application, intended for a later integration in a full SQUID-NMR system.

A working dc SQUID was manufactured on an YBCO ($YBa_2Cu_3O_{7-\delta}$) thin film deposited on a 10 mm x 10 mm MgO substrate. The SQUID was made of microbridge Josephson junctions, patterned by using the double resist laser lithography method, implemented during the course of this manufacturing process. The test of the SQUID showed a non-hysteretic current-voltage characteristic. Under the action of bringing a magnet closer to the SQUID under test, and then retracting it, the modulation of the I-V curve was observed. The critical current of the SQUID was $20\mu A$ and the resistance was 5.5Ω

A series of experiments were performed on destructive measurements of the sugar content in table grapes using NMR, in order to evaluate the feasibility of this technique. The total sugars(TSS) measurements of the same samples were carried out by refractometry, chosen as a conventional method for validation. The NMR measurements were evaluated to be 5.4% precise and have an accuracy of 9.3% relative to the refractometry measurements.

A further series of experiments were carried out on a high-Tc SQUID-NMR system.

A high correlation coefficient (0.85) of the increasing values of the T_1 and T_2 relaxation times to the decreasing concentration of sugar (sucrose) in water was obtained. Non-destructive measurements T_1 and T_2 in table grapes suggested a possible prediction of sugar content in table grapes from the values of T_1 or T_2. This technique also presented many advantages compared to the conventional high field NMR technique, such as the fast measurements that do not require spectral processing, the ease of sample preparation, and its non-destructive nature.

Uittreksel

Nie-vernietigende bepaling van interne vrugtekwaliteit met gebruik van SQUID-NMR tegniek

J.F. ISINGIZWE NTURAMBIRWE

Departement Elektrikiese en Elektronic Ingenieurswese,
Universiteit van Stellenbosch,
Privaatsak X1, Matieland 7602, Suid Afrika.

Tesis: MScIng (Electrical and Electronic Engineering))

Desember 2012

Die SQUID-NMR tegniek word al hoe meer aanbeveel deur navorsers oor die groot potensiaal, en dit beloof om in die toekoms van onskatbare waarde te wees in nie vernietigende evaluering. Die potensiaal moet grotendeels nog ontgin word, en die nie vernietigende kwaliteitsbeheer van voedselprodukte is een van die toepassings wat hier getoets word.

Die vooruitgang tot dusver om die stelsel te verbeter wat die gebruikersvriendelikheid en koste-effektiwiteit betref, toon dat met effens meer moeite dit moontlik sal wees om die tegnologie aan te pas vir lynsortering van vrugte, en om dit dalk ook as handtoestel beskikbaar te stel. Die vooruitgang tot dusver om die stelsel te verbeter wat die gebruikersvriendelikheid en koste-effektiwiteit betref, toon dat met effens meer moeite dit moontlik sal wees om die tegnologie aan te pas vir lynsortering van vrugte, en om dit dalk ook as handtoestel beskikbaar te stel.

Die doel is om die uitvoerbaarheid van interne vrugtekwaliteit metings deur hierdie tegniek te ondersoek en om 'n SQUID stelsel te ontwikkel wat gepas is vir SQUID-NMR toepassing, met die doel om dit later in 'n volledige SQUID-NMR stelsel te kan integreer.

'n Werkende GS-SQUID is vervaardig op 'n YBCO dunfilm wat op 'n 10 mm x 10 mm MgO substraat gedeponeer is. Die SQUID is van mikro-brug Josephson aansluitings/voegvlakke, waarop in die loop van die vervaardigingsproses 'n patroon m et dubbelweerstand laser litografie neergelê is. Toets van die SQUID het 'n niehisterese stroom-spanning as kenmerkend getoon. Die nader bring en terugtrekking van 'n magneet het gelei tot waarneming van die modulasie van die I-V kurwe. Die kritieke stroom van die SQUID was $20\mu A$ en die weerstand was 5.5Ω.

'n Reeks eksperimente is uitgevoer oor vernietigende metings van die suikerinhoud van tafeldruiwe met gebruik van NMR, om die gangbaarheid van hierdie tegniek te evalueer. Totale suikers (TSS) metings van dieselfde monsters is uitgevoer deur refraktometrie, wat gekies is as gebruiklike metode vir geldigheidsbepaling. Die NMR metings is as 5.4% presies/noukeurig evalueer, en met 'n akkuraatheid van 9.3% teenoor die refraktometrie metingsyfers.

'n Verdere reeks eksperimente is uitgevoer op 'n hoë-Tc SQID-NMR stelsel. 'n Hoë korrelasiekoëffisiënt van 0.85 van die toenemende waardes van T_1 en T_2 ontspantye teenoor die afname in konsentrasie van sukrose in water is waargeneem. Nie-vernietigende metings van T_1 eb T_2 in tafeldruiwe het gelei tot die moontlikheid van gebruik van hierdie tegniek om suikerinhoud van tafeldruiwe te voorspel. Die tegniek het ook baie voordele getoon in teenstelling met die gebruiklike hoëveld NMR tegniek, onder andere dat hierdie metings vinniger is, nie verdere verwerking van die spektrum benodig nie, die maklike voorbereiding van die monsters en die nie-vernietigende aard van die proses.

Acknowledgements

Firstly, my expression of sincere gratitude and appreciation go to my supervisor, Professor W. J. Perold, for his guidance, encouragement, positivity, kindness, understanding, for keeping me going and for being such a wonderful supervisor.

Secondly, I would like to thank my co-supervisor, Professor U. L. Opara, for keeping me on high standards and urging me to keep up a good work for excellence and for his support.

AIMS and SUN for providing financial support.

Fellows students for making the work environment enjoyable, for helping in the lab, and for their educational sharing of ideas.

Ulrich and Graham for always being there to provide technical support, and for their invaluable ideas.

Finally, I give thanks to the Almighty God, for granting me courage to keep up with the hard work and completing this thesis.

Dedication

This thesis is dedicated to my parents, Laetitia Bankundiye and Jean Bosco Nturambirwe.

Contents

i

Declaration **ii**

Abstract **iii**

Uittreksel **v**

Acknowledgements **vii**

Dedication **viii**

Contents **ix**

List of Figures **xii**

List of Tables **xvi**

Nomenclature **xvii**

1 Introduction **1**
1.1 Motivation 1
1.2 Aims and objectives 2
1.3 Structure of the thesis 3

2 NMR measurement and prediction of fruit quality **5**
2.1 Principles of NMR Technology 5
2.1.1 Nuclear Magnetic Resonance 5
2.1.2 Nuclear spin and magnetic field 6
2.1.3 Theory of NMR 7
2.1.4 NMR spectroscopy 9
2.1.5 Interpretation of the spectrum 14
2.1.6 NMR hardware 15
2.1.7 Applications 16
2.2 Fruit quality measurements 16
2.2.1 Analysis of fruit quality attributes 16
2.2.2 Destructive measurement: Methods and attributes that can be evaluated 17

2.2.3 Non-destructive measurement instrumentation 18
2.3 NMR application in fruit quality measurement and control 19
2.3.1 Modes of operation 20
2.3.2 Types of NMR devices 20
2.3.3 Summary of current studies of fruit quality using NMR . . . 21
2.4 Summary 24

3 Superconducting circuit building blocks and simulations 25
3.1 Superconductivity 25
3.1.1 General aspects 25
3.1.2 High-temperature superconductors 26
3.1.3 Theory development 26
3.2 Josephson junctions 31
3.2.1 Josephson superconductor tunnelling 32
3.2.2 Magnetic fields effect 34
3.2.3 RCSJ model 35
3.3 SQUID theory 40
3.3.1 Macroscopic quantum interference 41
3.3.2 Noise and sensitivity 45
3.4 Josephson junction simulations 47
3.5 Dc SQUID simulations 50
3.6 Flux locked loop simulations 52
3.7 Summary 54

4 Design, Fabrication and Testing of a DC SQUID 56
4.1 Design of the DC SQUID 56
4.1.1 Choice of Josephson junction type 58
4.1.2 Maskless SQUID design for laser lithography 59
4.2 Fabrication of a dc SQUID 59
4.2.1 Thin film deposition 59
4.2.2 Characterization of the $Y_1Ba_2Cu_3O_{7-\delta}$ surface deposited on an MgO substrate by using the sputter deposition technique . 64
4.2.3 Lithography 69
4.2.4 Etching of the circuits 70
4.2.5 Deposition of contact pads 72
4.2.6 Wire bonding and packaging 72
4.2.7 Fabrication of Josephson junctions on a SQUID template using AFM nanolithography 73
4.2.8 Nano-bridge based SQUID patterned using a Double-Resist Laser Lithography Method 74
4.3 Testing 78
4.4 Summary 79

5 Application of SQUID to NMR 81
5.1 Low-field NMR/MRI 81
5.2 Aspects of SQUID-NMR system development 82
5.3 Prepolarizing field 82

5.4 Configuration of the coils for magnetic fields. . . . 83
5.5 Noise considerations . . . 83
5.6 Design of the pickup coils . . . 84
5.7 Permanent magnets . . . 85
5.8 Pulse sequences . . . 85
5.9 Sample state considerations . . . 86
5.10 Summary . . . 86

6 NMR fruit quality measurements 88
6.1 NMR measurements of sugar content in table grapes . . . 88
6.1.1 Quantitative NMR (QNMR) . . . 88
6.1.2 Sample preparation . . . 89
6.1.3 Conditions for experiments . . . 90
6.1.4 Processing of the NMR spectra . . . 91
6.1.5 Visual analysis of ^{1}H NMR spectra . . . 91
6.1.6 Identification of metabolites . . . 93
6.1.7 Quantification of total sugars . . . 94
6.1.8 Quantification of total acids . . . 95
6.1.9 Quantification using an internal standard . . . 95
6.2 ^{1}H NMR vs standard measurements . . . 96
6.3 Validation of the method . . . 96
6.3.1 Selectivity and specificity . . . 97
6.3.2 Linearity . . . 98
6.3.3 Precision . . . 98
6.3.4 Accuracy . . . 98
6.3.5 Repeatability and comparability . . . 98
6.4 ^{13}C NMR experiments . . . 99
6.5 Relaxometry measurements by SQUID-NMR . . . 101
6.5.1 T_1 measurements . . . 101
6.5.2 T_2 measurements . . . 102
6.6 Summary . . . 103

7 Summary and conclusions 105
7.1 Summary of the thesis . . . 105
7.2 Conclusions . . . 106

Appendices 110

A Lab equipment 111

B EMC2 114

C Simulation codes 124

D Pulse sequences 129

List of References 132

List of Figures

2.1 Precession of a spin magnetization (left) and Zeeman splitting: quantization of a spin state under the effect of magnetic field (right). The energy gap between the split levels is equivalent to the resonant energy ΔE, where $\nu = \omega/2\pi$ is the resonance frequency, and it depends on the applied magnetic field strength 7
2.2 An illustration of the generation and collection of the NMR signal. . . . 9
2.3 The splitting into multiplets as it appears in a spectrum (right), and the energy diagram of a two spin system showing the J-coupling effect (left) 11
2.4 Spin-lattice and spin-spin relaxations. The evolution of the magnetization after it has been flipped by a 90° pulse 12
2.5 The FID (time dependent) is converted to a spectral graph of intensity versus frequency, by using the Fourier transform 13
2.6 An illustration of the signal averaging effect on the SNR of the NMR spectrum 13
2.7 The ^{13}C NMR spectrum of ethanol 14
2.8 The ^{1}H NMR spectrum for ethanol 15
2.9 The apparatus of an NMR system 15

3.1 The equivalent circuit of the two-fluid model 29
3.2 Schematic representation of a Josephson junction 32
3.3 The I-V curve for a Josephson junction. The current at zero voltage represents the Josephson current. 33
3.4 Interference pattern of a single junction without self-fields. 34
3.5 Circuit model of the RCSJ model 35
3.6 Circuit model of an overdamped junction. The current source is interchangeable with a voltage source. 36
3.7 The current-voltage characteristic of an overdamped junction. The curve is single-valued for an increasing and decreasing current. 37
3.8 The current-voltage characteristic of a critically damped junction. The curve is hysteretic. 38
3.9 The voltage-current characteristic of an underdamped junction. For a decreasing current from above I_c, the the characteristic is totally resistive. 38
3.10 Dc and ac voltage sources applied to a RSJ circuit. The junction voltage V is given by (3.2.5) 39
3.11 Ac response I-V curves when both dc and ac voltage driving sources are used (left), and an ac current source is driving the junction (right) . . . 40

3.12 A schematic representation of a dc SQUID. 41
3.13 I-V characteristic of a SQUID corresponding to applied fluxes of $n\Phi_0$ and $(n + 1/2)\Phi_0$, with n, an integer (left). SQUID voltage V versus applied flux (normalized with the fluxon) for a constant bias current (right). δV is the change in voltage as a result of a small change $\delta\Phi$ in flux 41
3.14 Two Josephson junctions connected in parallel in a superconducting loop. 42
3.15 Two resistively shunted Josephson junctions connected in parallel in a superconducting loop. 43
3.16 Spice equivalent circuit of a Josephson junction. 47
3.17 The average current $< i >$ versus voltage V curve for a junction driven by a dc voltage source for a) $\beta_c << 1$ (=0.1), b) $\beta_c = 1$ and c) $\beta_c >> 1$ (=10). 48
3.18 The $< v >$ versus I curve when the input to the junction is given by a constant current I_o for a) $\beta_c << 1$ (=0.1), b) $\beta_c \simeq 1$ (=4) and c) $\beta_c >> 1$ (=20). 49
3.19 The $< v >$ versus I curve when the input to the junction is an oscillating current of the form $I_o + I_s \sin(\omega t)$, with $\beta_c << 1$. The frequency of the oscillating source is 2GHz and the amplitude is 60μA. 49
3.20 Equivalent circuit of a dc SQUID as simulated in NGSpice. 50
3.21 Current-voltage characteristic for applied flux values of $(n+1/2)\Phi_0$, where n is an integer. 51
3.22 Current-voltage characteristic for applied flux values of $n\Phi_0$, where n is an integer. 51
3.23 Voltage versus flux characteristic for a dc SQUID. The flux is normalized with the flux quantum. 52
3.24 Circulating current versus SQUID flux. 52
3.25 Included flux of the SQUID versus applied flux. The curve is hysteretic. 53
3.26 The flux locked loop simulated with NGSpice, with the applied flux linearly swept from 0 to Φ_0, then down to $-\Phi_0$, and back up to 0. 53
3.27 Flux locked loop simulations with a small input signal at 500 MHz. The applied flux (left) and the output voltage (right) are plotted against time. 53
3.28 NGSpice small signal ($\Phi_0/4\pi$) simulations of a flux locked loop at 50 MHz. The figures show the applied flux (left) and the output voltage (right) versus time. 54
3.29 Flux locked loop simulations of a sinusoidal input signal with a single fluxon amplitude at 10 MHz. The figures show the included flux in the SQUID loop (left) and the voltage at the output of the flux locked loop (right), both as function of time. 54

4.1 A schematic representation of a Dayem-bridge with its dimensional parameters 58
4.2 Sputtering deposition temperature profile 62
4.3 PLD interior at rest (left) and in action (right) showing plume projection focused on the sample 63
4.4 PLD deposition temperature profile 64

4.5 Schematic diagram of a diffraction grating of a crystalline material. The horizontal lines represent the atomic planes (Bragg planes) that reflect the incident X-ray after diffraction into the material 65
4.6 Orthorhombic primitive cell of an YBCO crystal structure. The cell dimensions of $YBa_2Cu_3O_7$ are a=3.88 Å, b=3.84 Å, and c=11.63 66
4.7 X-ray diffraction characterization of *c*-axis $Y_1Ba_2Cu_3O_{7-\delta}$ thin films deposited on MgO by a dc sputtering technique. 67
4.8 The susceptance versus temperature characteristics of a $Y_1Ba_2Cu_3O_{7-\delta}$ thin film deposited on MgO by PLD. The critcal temperature is T_c=89K and the transition width δT=0.25K. 68
4.9 AFM picture of an YBCO film deposited by ICM sputtering, showing the roughness of the surface (left). The cross section of the surface of a superconducting YBCO thin film, with the surface roughness strictly less than 18 nm (middle). PLD YBCO film surface, showing a surface roughness much worse than the ICM sputtered case, with noticeable big boulders (right). 69
4.10 SQUID fabrication process using UV lithography. The chrome mask was designed at Stellenbosch University. 70
4.11 Left: A dc SQUID structure patterned by UV lithography and etched by wet solution of citric acid. The optical microscope picture shows no significant reduction of the YBCO lines in width. Right: Large area SQUID patterned by UV lithography and etched by Argon ion milling. Picture taken with a Scanning Electron Microscope from the microelectronic lab at the University of Stellenbosch. 71
4.12 Annealing profile used for the films after deposition of the contact pads. 73
4.13 DC SQUID mounted and wire bonded onto a PCB for testing. 73
4.14 AFM-scratched bridges on the legs of a washer SQUID. The constrictions are of the order 0.9 and 1μm wide (left). Topographic cross section of a scratch by the diamond coated silicon AFM tip (right). 74
4.15 Lithography process using the laser system and the method described in Section 4.2.8. 75
4.16 a) Micro-constrictions fabricated by laser lithography along a loop of superconducting $Y_1Ba_2Cu_3O_{7-\delta}$ film. The constriction widths are of the size 1.2μm and 0.8μm. b) AFM picture of nano-bridges defined by laser lithography. 76
4.17 SQUID loop with bridges as junctions, fabricated by a laser lithography, double resist combination. 77
4.18 Laser lithography system 77
4.19 Setup of the apparatus used to test the SQUID in this project. The dc SQUID tested had $I_c = 20$ μA, and $R_n = 5.5\Omega$. 78
4.20 V-I curve of the tested SQUID at extreme positions during flux modulation: a) no magnetic field applied ($n\Phi_0$), b) magnet in the proximity of the device under test. 79

6.1 ^{1}H NMR spectrum of a grape berry: a) Predominantly sugars, b) Aliphatic components. 92
6.2 Comparison of total sugars measured by refractometry and NMR 97

6.3 QNMR values versus TSS values by refractometry. 98
6.4 NMR ^{13}C spectrum of a table grape powder 101
6.5 Correlation of T_1 values measured on solutions of sugar versus the dilution factor 102
6.6 Correlation of T_2 values measured in solutions of sugar versus the dilution factor 103
6.7 Screen capture of the FID(top) and Fourier transformed spectrum (bottom). The figure at the right shows spin echoes for the T_1 measurement. 104

A.1 PLD system and accessories: deposition chamber(A), control unit (B) and the laser unit (C) 111
A.2 The sputtering unit showing the deposition chamber (A), the control unit (B), and the vacuum pumps (C) 111
A.3 The aligner system for UV photolithography (left) and the wire bonder (right). 112
A.4 The thermal evaporator used to deposit the silver pads on the SQUID chip. 112
A.5 Equipment for testing the SQUID: Mr. SQUID system (A), power supply (B) for an external heater of the cold finger (F) during warm up, Oscilloscope (C), cryogenic measurement system (D), computer monitor for digital display (E), vacuum pump (G) to evacuate the cold finger while cooling down with the cryogenic system (H) operated with liquid helium. 113

B.1 SQUID chip circuitry, showing the external loop (pickup loop : A) and areas for contact pads (B) 114
B.2 Mask for the contact pads evaporation 122
B.3 The Mr. SQUID chip and circuitry adapted to test the SQUID fabricated in this project. Dimensions are not to scale. 123

D.1 Full ^{1}H NMR spectrum of a table grape. 129
D.2 An example of pulse sequence used for measuring the T_1 relaxation time 130
D.3 Single-shot pulse sequence on-line determination of sugar content in fruit 130
D.4 Pulse sequence used in three dimensional imaging 131

List of Tables

2.1 An example of the elements accessible by NMR 6

4.1 Deposition parameters for ICM sputtering 62
4.2 Deposition parameters for PLD 63

6.1 ^{1}H NMR chemical shifts of grape metabolites and integral of peaks in one of the samples used in experiments. Compounds were identified by references and using 1D NMR spectra (CD_3OD-KH_2PO_4 in D_2O, pH 6.0) 94
6.2 Total sugar concentration measured by refractometry and NMR on the same samples. The measurements were carried out on the same batch of grapes 96
6.3 Values of total sugar concentrations measured by refractometry and NMR on samples bought from different shops in Stellenbosch. The abbreviations are explained as follows: sb: **B**lack grapes from **S**hoprite, srg: **R**ed **g**lobe grapes from **S**hoprite, sw: **W**hite grapes from **S**hoprite, pr: **R**ed grapes from **P**ick and pay, pw: **W**hite grapes from **P**ick and pay, wr: **R**ed grapes from **W**oolworth 100

Nomenclature

Constants

$\Phi_0 =$ 2.07×10^{-15}(Wb)
$\pi =$ 3.141 592 654
e = 2.718 281 828
$h =$ 6.626×10^{-34}(J-sec)
$k_B =$ 1.38×10^{-23}(J/K)

Abbreviations

HBCCO Mercury-Barium-Calcium-Copper-Oxide($HgBa_2Ca_2Cu_3O_{8+\delta}$,)
YBCO Yttrium-Barium-Copper-Oxide($YBa_2Cu_3O_{7-\delta}$)
LBCO Lanthanum-Barium-Copper-Oxide(LaBaCuO)

Symbols

E Vector electric field
H Vector magnetic field
D Vector electric displacement
B Vector magnetic flux density
J Vector current density
ρ Charge density

Chapter 1

Introduction

1.1 Motivation

Nowadays, human lifestyle is characterised by a climate of interdependence. It is dominated by an exchange system, where means are exchanged for goods, and vice versa. This is also called the trade system, or market. When it comes to agricultural products, the exchange takes place between growers, vendors and consumers.

In the next sections, the term product will be used to designate horticultural products, specifically fruits.

Consumers value these products depending on different quality attributes, both internal and external. Vendors are then required to present products with acceptable quality. This always returns to the role of the growers, as they are the starting point of the exchange chain. Growers are always required to do the sorting and grading of their products before delivering them to the vendors.

Various techniques and methods are used for sorting and grading products, and they can be either destructive or non-destructive. Destructive methods result in a loss of that part of the harvest that has been used as samples for the evaluation of the quality. Non-destructive methods do not require any sample pre-treatment, there is no waste after measurements, and often the measurements are relatively fast, making them the preferred testing method. Some non-destructive methods already in use [1] are X-ray computed tomography (X-ray CT) for internal defects, impact analysis for firmness, headspace fingerprinting mass spectrometry (HFMS) for aroma, near infrared spectroscopy(NIRS) for taste, and nuclear magnetic resonance (NMR) [2], amongst others.

The NIR method exposes fruits to near-infrared rays and measures desired quality attributes based on the reflectance and/or transmittance of the radiation. Though this method is widely used, it presents some drawbacks, such as the inaccuracy of internal quality attributes of thick-skinned fruits like citrus due to limited penetration depth, the need for recalibration, the difficulty of model transfer between two different spectrophotometers, expensive technology, and poor reliability[3], [4].

X-ray computed tomography, though a powerful technique from a horticultural point of view, for its 2- and 3-dimensional images and better resolution than NMR, still presents a greater degree of underestimation compared to the latter (12% versus 6%) [5].

The NMR method on the other hand, turns out to be the most sensitive, is easily operated, provides a wide variety of operational modes (see Section 2.3.1) and, hence, various types of information are accessible through it. The fact that an NMR system is built with very big superconducting electromagnets in order to provide strong and homogeneous fields, makes it extremely expensive (the cost of an NMR system ranges from $120 000 to $3 000 000). In conventional high-field NMR, strong magnetic fields are a requirement for an NMR signal to be detectable [3].

In order to reduce the cost of an NMR spectrometer, intensive research in the low-field range has been carried out. Many researchers have tried different possibilities [6], [7] to overcome the constraints encountered at low-field, and the best was the use of a Superconducting Quantum Interference Device (SQUID) as the sensor, instead of the conventional coils [8], [9]. By using this extremely sensitive magnetometer (the SQUID), only small magnets are required, or even coils, to polarize the material, The cost of such a system can thus be significantly reduced.

1.2 Aims and objectives

NMR systems have proven their potential, but are very costly and thus cannot be used in the fruit industry without being modified. Therefore, it is essential to develop systems that are easier to use and financially affordable. In horticultural industries where fruits are sorted on conveyors, one would need an NMR system that allows analysis of large sample sizes, and taking the high speed of the conveyors and the materials they are made of into account. Growers also prefer hand held devices that can be used in the field. All these requirements are still a long way off from becoming a reality.

The aim of this project is primarily to fabricate a Superconducting Quantum Interference Device, prior to the development of a SQUID-NMR system for the exploration of the internal quality of fruits. Such a system would comprise a mini-NMR system, where the NMR signal is detected by a SQUID, instead of a conventional coil system. A second goal is the investigation of the applicability of the NMR technique to internal fruit quality evaluation.

- The design will incorporate the full structure of the SQUID chip, with parameters chosen for optimal performance.
- The fabrication section will mostly focus on the design and manufacture of a working SQUID. The fabrication of a SQUID is a series of processes that have to be carried out one after the other. All the steps will be followed, and when alternative methods are possible, the best will be chosen.

- When the SQUID is tested, it should work according to the theoretical principles of SQUIDs, and give results in agreement with the simulations that were performed in this thesis.
- The investigation of the NMR technique will be carried out in order to practically probe the extent of its applicability. It is also important to gain insight into the connection between the design and manufacture, and the expected outputs of NMR usage.
- It is within this scope that fruit quality measurements will be done, using high-field NMR as comparison to standard validation measurement techniques.
- The data to be analysed will be acquired in the context of Quantitative NMR (QNMR).
- Standard measurements will be done utilising a conventional technique, °Brix spectrometry, and will be carried out on the same samples.
- Furthermore, non-invasive measurements of fruit quality were done on a commercial SQUID-NMR system, and correlated with sugar concentration in water.
- Finally, conclusions will be drawn on the preferability, feasibility, and the limits of these techniques.
- A comparison between conventional NMR and SQUID-NMR measurements will conclude the investigation.

The techniques that are used in this thesis are explained in different chapters, as mentioned in the next section.

1.3 Structure of the thesis

This thesis is divided into seven chapters and is structured as follows:

- Chapter 1 serves as an introduction by explaining what the thesis contains, what had to be done to complete it, and how.
- Chapter 2 explains the principles of NMR spectroscopy, its applications, the concept of fruit quality and its evaluation and exploration, and especially the use of NMR to this end.
- Chapter 3 introduces the theory of superconductivity, Josephson junctions and SQUIDs. Simulation results of different features of these basic superconducting circuits are presented, using a SPICE circuit simulator (NGSpice, Version 21).
- Chapter 4 reports in detail on the steps followed during the fabrication of a SQUID that can be used in the context of this project.

- Chapter 5 talks about the most important factors to take into account when developing a SQUID-NMR system. The system comprises of a system of coils that generate different magnetic fields, the readout electronics of the SQUID, the rf signal generator, the control board, the cryogenic system, etc.
- Chapter 6 presents the methods and results of the measurements carried out on fruits.
- Chapter 7 summarizes the project, concludes and gives recommendations for future work.

Chapter 2

NMR measurement and prediction of fruit quality

NMR technology finds application in various areas, including testing and prediction of the quality of fruits. Understanding the principles of nuclear magnetic resonance is key to knowing its functionality, its limits, its advantages, and the information accessible from it.

Understanding the NMR signal is also of key importance when it comes to correlating the NMR signatures of different types of fruit with the internal quality attributes, such as sugar content and acidity. This enables us to establish a meaningful interpretation within context, in laymen's terms (conversion of spectral data to sugar concentrations, from which the maturity index is derived).

Many researchers have investigated and used NMR technology in evaluating the quality of agricultural products [10]. Many publications, from different authors, have confirmed that the technique is a very powerful tool for this application [4], [2]. In this chapter we describe the principles of NMR spectroscopy and of fruit quality measurements, both destructively and non-destructively, and the different technologies behind them, that are currently in use in conjunction with the NMR technique. An overview of the actual successes of the NMR technique for the evaluation of fruit quality, is also surveyed in this chapter.

2.1 Principles of NMR Technology

2.1.1 Nuclear Magnetic Resonance

Nuclear magnetic resonance (NMR) is a quantum mechanical phenomenon that was discovered by scientists in the late 1930s. Historically, it is noted that in 1938 Isidor Rabi successfully designed an experiment to detect and measure the magnetic spin of atomic nuclei in gases. This proved the idea suggested earlier by Pauli, in 1924, that atomic nuclei have magnetically related spins [11]. It was in 1946 that Rabi's discovery related to gases was also independently confirmed in liquids and solids by two physicists, Edward Purcell and Felix Bloch, who published their observations in

the same year. In 1949 the chemical shift phenomenon was observed and in 1966, for the first time, the Fourier Transform technique was introduced into NMR by Ernst and Anderson [12]. Further developments have been achieved for novel applications like solid and solution state NMR in the late 1960s. Nowadays, NMR imaging has become a major tool in radiological medical diagnostics.

NMR is applied to non-destructive techniques, which makes it a method widely used to investigate the structure of various materials in different fields of science and medicine. Some of these materials are organic molecules, fresh and processed produce in the food industry, living tissue, etc.

This section presents the concept of NMR, ranging from its basic principles and the concept of nuclear spin relaxation, the detected NMR signal, to NMR spectroscopy.

2.1.2 Nuclear spin and magnetic field

The nucleons in any atomic nucleus have an intrinsic quantum property, known as spin. This property is responsible for the rotation of nucleons (protons and neutrons) around their individual axes. The spins confer to the nucleus as a whole, with an overall spin quantum number S equivalent to 0 if the number of both the protons and the neutrons is even. Otherwise, S will be non zero in accordance with Pauli's principle [13].

Isotope	Z	Spin	NMR freq. at 1 T(MHz)	Rel. sensitivity	Abundance(%)
^{1}H	1	1/2	42.577	1.000	99.98
^{11}B	5	3/2	13.660	0.165	81.17
^{13}C	6	1/2	10.705		1.1
^{14}N	7	1	3.076	0.001	99.635
^{15}N	7	1/2	4.315	0.001	0.365
^{19}F	9	1/2	40.055	0.834	100
^{29}Si	14	1/2	8.460	0.079	4.7
^{31}P	15	1/2	17.23	0.066	100

Table 2.1: An example of the elements accessible by NMR

.

In nuclei that have a spin of one-half, like ^{1}H and ^{13}C (see Table 2.1), which are the commonly studied nuclei, only two spin states are possible: $m = 1/2$ or $m = -1/2$, where m is the magnetic quantum number associated with the spin angular momentum S, as explained in (2.1.1). These states have the same energy (or are degenerate).

When such a nucleus is placed in a magnetic field, the magnetic moment of the spinning nucleus precesses with a characteristic angular frequency $\omega = \gamma B_0$, hence it is dependent on the applied magnetic field. The factor γ is a characteristic property of nuclei and is called the gyromagnetic ratio. The interaction between the nuclear magnetic moment and the magnetic field leads to a quantization of the above mentioned spin states [14]. This means that the two states no longer have the same

energy. This results in an alignment of the magnetic moment with the direction of the magnetic field. Two orientations are thus possible, namely parallel or anti-parallel.

Consider a magnetic field B_0 oriented in the z-direction. The angular momentum associated with the nuclear spin is quantized (in magnitude and direction). Therefore, m can take values only from $+S$ to -S in integer steps which turn in $2S+1$ states of angular momentum for any given nucleus [3].

The z-component of the magnetic moment is given by

$$\mu_z = \gamma m\hbar = \gamma S_z, \tag{2.1.1}$$

where S_z is the z-component of the vector S, γ is the gyromagnetic ratio, and $\hbar$ is the reduced Planck constant.

The energy difference between the two orientations is given by the relation [14]

$$\Delta E = 2\mu_z B_0. \tag{2.1.2}$$

The quantization of nuclear spin states in a magnetic field is illustrated in Fig. 2.1.

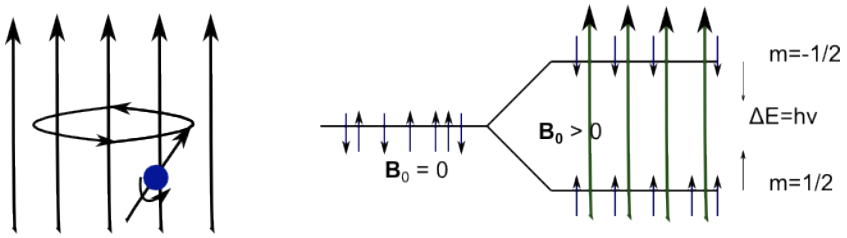

Figure 2.1: Precession of a spin magnetization (left) and Zeeman splitting: quantization of a spin state under the effect of magnetic field (right). The energy gap between the split levels is equivalent to the resonant energy ΔE, where $\nu = \omega/2\pi$ is the resonance frequency, and it depends on the applied magnetic field strength

.

2.1.3 Theory of NMR

Nuclear magnetic resonance is a property that nuclei manifest when exposed to a magnetic field and electromagnetic (EM) pulse(s), which consists in the EM absorption of the pulse energy by the nuclei, followed by the back radiation of the absorbed energy at a specific resonance frequency.

The principle of NMR comprises three consecutive steps [15]:

1. The polarization (lining up) of the nuclear magnetic spins within a constant magnetic field.

2. The disruption of this adjustment of the nuclear spins by applying an EM pulse (usually rf pulse). The latter is preferably applied perpendicular to the magnetic field for optimal signal results.

3. The back radiation, recorded as the relaxation of the flipped total magnetization.

As seen previously, all stable isotopes that contain an odd number of protons and/or neutrons, have a non zero spin, and consequently an intrinsic magnetic moment and angular momentum. They can thus be studied by NMR spectroscopy.

Only specific pulse frequencies can be absorbed by the nuclei, depending on the static magnetic field strength and the type of nuclei. When the frequency of the EM radiation is applied, the resonant absorption will occur only at the correct frequency (resonance frequency) $\nu = \Delta E/h$, to match the energy difference between the nuclear spin levels in a constant magnetic field of the appropriate strength [14]. This resonance radio frequency has to be equal to the Larmor precession frequency of the nuclear magnetization in the constant field. It is this magnetic resonant absorption that is detected in NMR. Details of the detection process are provided in Section 2.1.4. A global illustration of the NMR signal production is shown in Fig. 2.2.

Before application of the rf pulse, the nuclei in both spin states are oriented around the z-axis and precessing with characteristic frequency. The xy-component of the total magnetization is zero ($M_{xy} = 0$). $M = M_z$, and is aligned with the z-axis.

Upon application of the rf pulse, all the individual nuclear magnetic moments are coherent in phase. The net magnetization starts to precess around the z-axis, M_{xy} is no longer zero, and is given by $M_{xy} = M \sin \alpha$. The tip angle α is determined by the power and duration of the electromagnetic irradiation. For a 90° pulse, $\alpha = 90$ and $M_{xy} = M$.

The net nuclear magnetization starts to reduce in the xy-plane and to increase along the z-axis. Loss of phase coherence and reversion of the states populations occur when irradiation ceases. The individual nuclear magnetic moments return to their random arrangement around z, in a Boltzmann distribution [12].

Fig. 2.2(a) and (b) show the polarisation of spin magnetizations and the application of the rf pulse. In (c) the flipping of the total magnetization into the xy-plane is shown. Stage (d) and (e) are the progression of decay of the transverse magnetization, whereas (d) and (e) are about the regrowth of the longitudinal magnetization. The last stage in (e) displays the conversion of the relaxation into the NMR signal in the time domain (FID). The process starting from (d) to (g) is called a "relaxation process" and it is recorded by NMR spectroscopy.

There are two types of relaxation processes, namely T_1 (spin-lattice relaxation) and T_2 (spin-spin relaxation).

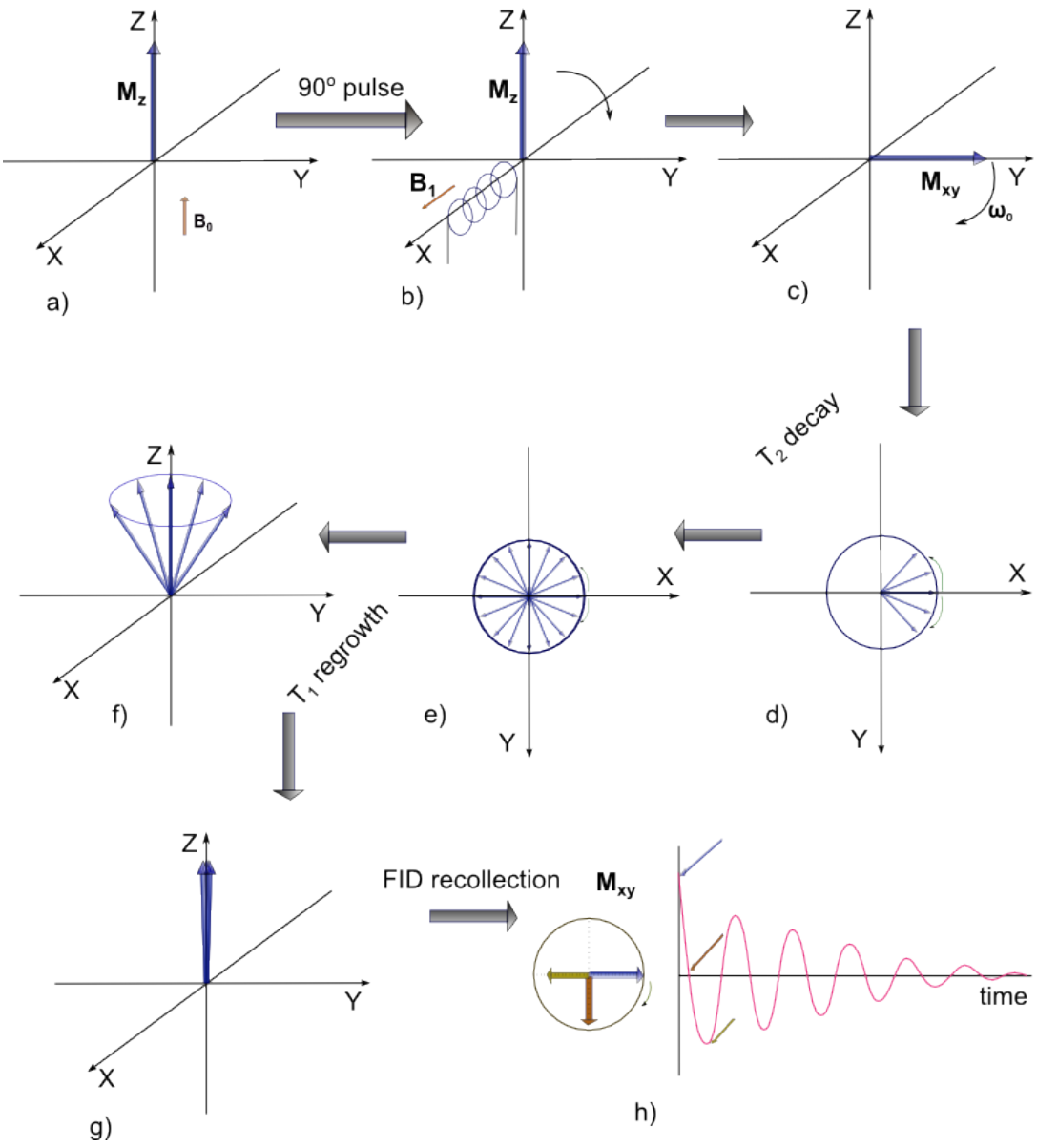

Figure 2.2: An illustration of the generation and collection of the NMR signal.

2.1.4 NMR spectroscopy

The signal produced by NMR is not ready for interpretation. It needs to be detected and processed to provide useful information [15].

When an RF magnetic pulse of appropriate frequency and duration is applied, the net magnetic moment can be rotated by $\pi/2$ radians, and thus becoming perpendicular to the applied magnetic field. This does not, however, affect the precession of the particles [16].

If a coil is placed perpendicular to the direction of the magnetic moment, a si-

nusoidal current is induced in the coil as the net magnetic moment sweeps through it. This kind of detector is called a Faraday detector [3], and the oscillating electric current is known as the Free Induction Decay (FID), which is the NMR signal.

The stage at which the NMR signal is collected, is illustrated in Fig. 2.2(h).

NMR uses a number of parameters to measure different properties of materials. These parameters are listed and explained below:

1. Chemical shift indices
   The chemical shift is the change in the resonance frequency of a nucleus due to the position of the atom within a molecule (the chemical environment). The bonding electrons create their own magnetic field, which modifies the external magnetic field in the vicinity of the nucleus. It is this behaviour that is responsible for the chemical shift. The chemical shift consists in a subtle variation, which is measured in parts per million (ppm), and provides detailed information about the structure of molecules [16]. Different atoms within a molecule can be identified based on molecular symmetry and the predictable effects of nearby electronegative atoms and unsaturated groups [15]. The ppm scale is a relative unit and has the advantage that it is characteristic to a nucleus irrespective of the field, as long as the reference is the same.

   The chemical shift, denoted by δ is given by the relation

   $$\delta = (\nu - \nu_{ref}) \times 10^6/\nu_{ref}, \tag{2.1.3}$$

   where ν_{ref} is the frequency of the reference, such as tetramethylsilane ($S_i(CH_3)_4$).

   The resonant frequency for a particular nucleus at a specific position within a molecule is given by

   $$\nu = \nu_0(1.0 + \delta \times 10^{-6}), \tag{2.1.4}$$

   where ν_0 is the fundamental resonant frequency of the isotope. As an example, in a 5 T field, for ^{13}C at C-4 position of cycloheptanone (δ=23.3 ppm), the resonant frequency is $50.000(1.0+23.3\times10^{-6})$ MHz = 50.001160 MHz [15].

   In Fig. 2.7 the effect of the chemical shift in the NMR spectrum is shown.

2. J-coupling
   Also called spin-spin coupling, this is the influence of a nucleus on its neighbor's effective magnetic field. This effect is observable if the distance between non-equivalent nuclei is less than or equal to three bond lengths [16]. This will result in each spin seeming to have two energy 'sub-levels', depending on the state of the spin it is coupled to, as shown in Fig. 2.3.

   The magnitude of the separation is called the coupling constant, J, and is expressed in Hertz. The value of J (peak separation) provides information on the dihedral angles, which is useful in determining the structure of molecules, such as their conformation. In general, when neighboring spins are available

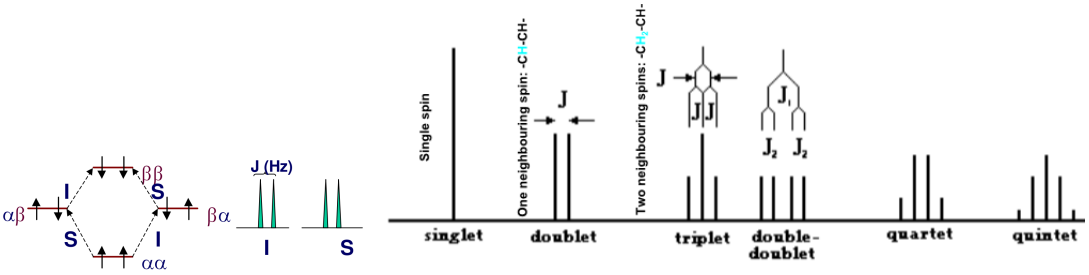

Figure 2.3: The splitting into multiplets as it appears in a spectrum (right), and the energy diagram of a two spin system showing the J-coupling effect (left) [12]

the splitting results in $n+1$ split peaks with relative intensities determined by Pascal's triangle [15].

3. Nuclear Overhauser Effect (NOE)
   This effect is useful to determine inter-atomic distances, which are important for accurate determination of structures of proteins and nucleic acids in three-dimensions. It consists in a direct through-space interaction of two nuclei. As an effect of the irradiation of one nucleus with a weak radio-frequency signal at its resonant frequency, the equation of the populations in its two energy levels disturbs the populations of nearby nuclei, enhancing the intensity of absorbency at the resonant frequency of the latter [11], [12]. This effect is uniquely distance-dependent, even if the two nuclei are far apart in the bonding network. It varies in intensity as the inverse sixth power of the distance. It is only detectable between ^{1}H nuclei separated by a distance of 5Å or less.

4. Further useful information regarding the determination of molecular structures is the bond orientations, and this is provided by another effect called residual dipolar coupling. Information about the latter can be found in [17].

5. Relaxation rates (T_1 and T_2)

   a) After an external magnetic field is applied to a sample (at t_{on}), the macroscopic nuclear magnetization increases exponentially from zero, as given by

$$M_z(t) = M_{eq}(1 - e^{-(t-t_{on})/T_1}). \tag{2.1.5}$$

   T_1 characterizes the time taken by a system of nuclear moments to reach equilibrium orientation in a magnetic field (see Fig. 2.4) [12], [3]. 63% of the equilibrium state magnetization is recovered after a time equal to T_1 [18].

   The T_1 time constant depends on the nuclear isotope, and on the physical properties of the sample, such as its viscosity and temperature. T_1 is usually in the milliseconds to seconds range, but can extend to years.

b) After the macroscopic magnetization of the sample is rotated by $\pi/2$ radians (at t_{flip}), the magnetization will not rotate in the xy-plane for ever, but will decay exponentially as given by

$$\begin{aligned} M_x(t) &= -M_{eq}cos(\omega_0 t)(1 - e^{-(t-t_{flip})/T_2}) \\ M_y(t) &= M_{eq}sin(\omega_0 t)(1 - e^{-(t-t_{flip})/T_2}). \end{aligned} \tag{2.1.6}$$

T_2 (spin-spin/transverse relaxation time) is associated with the phase of the precessing nuclear moments, and is a measure of how fast the macroscopic transverse nuclear magnetization loses strength after being rotated by $\pi/2$ radians [3]. T_2 is the time within which the transverse magnetization M_{xy} drops 37% of its initial magnitude [18].

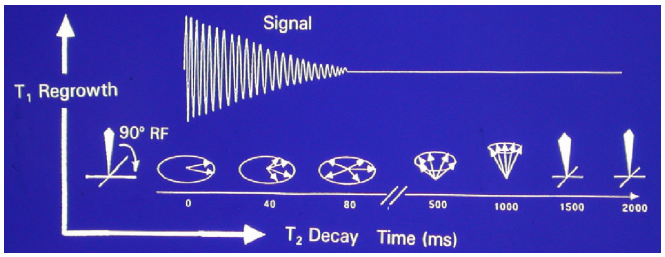

Figure 2.4: Spin-lattice and spin-spin relaxations. The evolution of the magnetization after it has been flipped by a 90° pulse [12]

2.1.4.1 Fourier transform

In modern NMR spectrometers, the entire spectrum can be recorded in 2-3 seconds, rather than 5 minutes. This is made possible by the 'Fourier-Transform' (FT) technique. The sample is given a strong radio frequency pulse, which aligns the nuclei so that their precession is synchronized. The result of this synchronization is a measurable rotating magnetic field, which induces an electrical voltage in a coil placed next to the sample. Over a period of a second or two this macroscopic signal dies down. This observed "echo" in the coil (FID), contains all the resonant frequencies of the sample nuclei combined in one cacophonous reply [14], [19].

The FT consists in a fast conversion, by a computer, of this data from an FID signal, as a function of time, to a graph of intensity versus frequency. This 'spectrum' has one peak for each resonant frequency in the sample. This is based on the mathematical relation

$$f(\omega) = \int_{-\infty}^{+\infty} f(t)e^{-i\omega t}dt = \int_{-\infty}^{+\infty} f(t)[\cos(\omega t) - i\sin(\omega t)]dt \tag{2.1.7}$$

and is illustrated in Fig. 2.5.

Here, the function of time used represents the total nuclear magnetization.

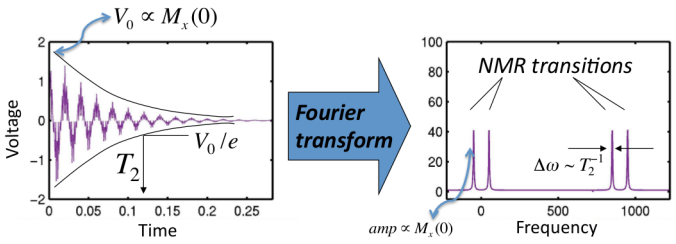

Figure 2.5: The FID (time dependent) is converted to a spectral graph of intensity versus frequency, by using the Fourier transform [20].

2.1.4.2 Signal averaging

Usually, the NMR signal is very weak and contains unwanted noise that can mask the desired signal. In order to overcome this problem, signal averaging is used to enhance the signal. The process of pulse excitation and recording the new FID is repeated many times, each time appending the FID data (Fig. 2.6) to a sum previously stored in the computer.

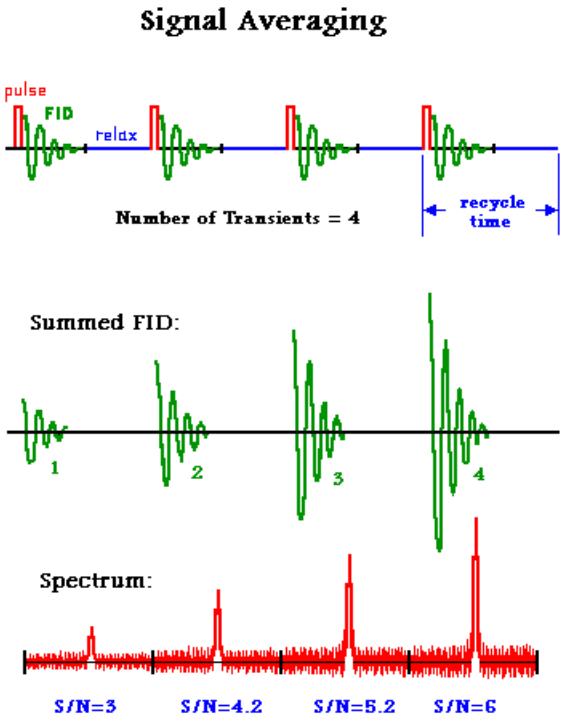

Figure 2.6: An illustration of the signal averaging effect on the SNR of the NMR spectrum [19].

The signal-to-noise ratio (SNR) thus increases proportionally to the square root of the number of transients, and is given by

$$SNR_{1+2+...+N} = \sqrt{N}\frac{\sigma_{NMR}}{\sigma_{noise}}, \tag{2.1.8}$$

where, N is the total number of repetitions, and σ is the rms value of the signal indicated by its index.

This signal averaging process results in a sensitivity which is a great improvement over the old frequency sweep method [19].

2.1.5 Interpretation of the spectrum

The NMR spectrum appears as a series of vertical peaks distributed along the frequency or ppm-axis of the spectrum. Every peak represents an atom in the molecule that is being observed. The position of the peak in the spectrum gives information about the local structural environment of the atom producing the signal [21]. Examples of the ^{13}C and ^{1}H spectra of ethanol (CH_3CH_2OH) are given in Fig. 2.7 and Fig. 2.8 respectively.

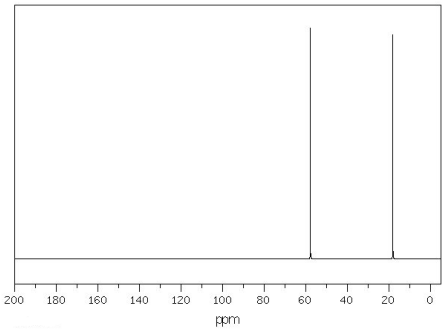

Figure 2.7: The ^{13}C NMR spectrum of ethanol [21].

The two carbons in ethanol are in different structural environments and hence each produces a signal in the NMR spectrum. The carbon attached to oxygen is deshielded due to the electronegative nature of oxygen and this shifts its signal towards the left in the spectrum. The carbon, on the other hand, bonded only to hydrogens and appears at the right of the spectrum [21].

In the case of the ^{1}H NMR spectrum of ethanol, the two protons of the CH_2 group neighboring the oxygen are further to the left in the spectrum, whilst the hydrogens of the CH_3 group that is most remote from the oxygen produce a signal towards the right of the spectrum. The signals in the ^{1}H NMR spectrum do not necessarily appear as a single line. The splitting pattern seen in these signals gives information as to how many hydrogens are present on the neighboring carbon. Also, integration

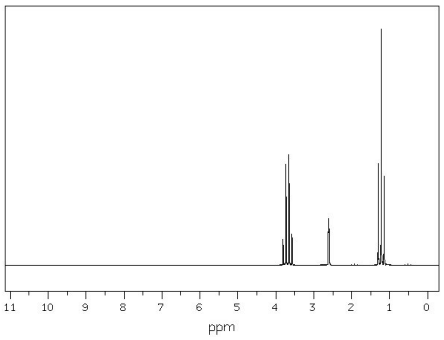

Figure 2.8: The ^{1}H NMR spectrum for ethanol [21]

of the ^{1}H NMR signals allows the number of hydrogens in each environment to be determined [21].

2.1.6 NMR hardware

The need for a very strong magnetic fields, which is generated using superconducting electromagnets (Section 1), was mentioned previously. This implies the necessity for very low temperatures.

The coils of the magnet are surrounded by liquid helium (at ∼4K). A layer of liquid nitrogen (at 77K) surrounds the helium to prevent it from boiling off quickly, and both are contained in a double layer of steel, with a vacuum between them as an insulator. A narrow hole through the middle of the magnet allows for the introduction of the sample tube in the rf coils [21].

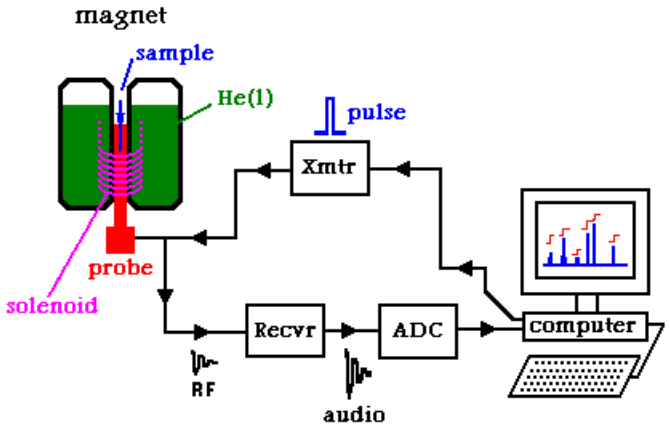

Figure 2.9: The apparatus of an NMR system [19]

2.1.7 Applications

The NMR technique is used for the identification of detailed structural information about chemical compounds, such as:

- Identifying contaminants in food, cosmetics, or medication;
- Determining the purity of medicines for accurate delivery;
- Identifying drugs seized by police and customs agents;
- Helping research chemists discover whether a chemical reaction has occurred at the correct site on a molecule [21];
- Checking the structure of plastics, to confirm the desired properties;
- Determination of the internal quality and defects of horticultural products [4];
- Determination of adulteration of dairy products and fruit juices [22];
- Studying human tissue (MRI) [23], etc.

2.2 Fruit quality measurements

Fruit quality is seen as a combination of fruit attributes or characteristics that have significance in determining the degree of consumer acceptance. The acceptability is influenced mainly by three elements [3]:

- The intrinsic properties of the fruit (e.g. colour, firmness, acidity, etc.), which are the base on which the consumer assigns a quality value to a fruit.
- The market situation, depending on the cost and the competitiveness of the other products on the same market.
- The consumers' preferences, which depend on the intended use of the fruit by the consumer.

This thesis draws attention to only the intrinsic properties, that we will simply call fruit quality. Fruit quality may be based on internal or external attributes [5]. Many methods of measurement are in use, depending on the attributes to be evaluated.

2.2.1 Analysis of fruit quality attributes

Considering the process of analysis and the principles involved, the quality attributes can be grouped into three categories [5], [2]:

1. Physical attributes of quality can be measured by evaluating the response of the subject to physical phenomena, such as light transmission/reflection, gravity, etc. Here we can measure the total soluble solids, firmness, fruit weight, juice percentage, rind color and thickness, fruit size, shape and volume, and specific gravity.

2. Chemical attributes, on the other hand, are evaluated from the reaction of internal parts of the fruits to the action of specific chemicals. The total titratable acidity, ascorbic acid, total sugars, reducing and non-reducing sugars, and pH can be measured through these means.

3. Physiological parameters determine the shelf life of the fruit, particularly the stage of maturity. We can list CO_2 evolution, rate of respiration, rate of transpiration, growth regulator (hormonal) content, etc.

2.2.2 Destructive measurement: Methods and attributes that can be evaluated

A number of quality attributes can be measured by means of destructive methods. Only the attributes that fall within the scope of this thesis will be considered:

1. The firmness of the fruit, which is a mechanical property, and gives an indication of maturity and the condition of the fruit in general. It can be measured in terms of puncture resistance, compression, creep, impact, and sonic properties. A penetrometer can be used to measure the firmness, and when one is used it is important to specify the type of instrument used, and the working parameters, such as dimensions and shape of the plunger, penetration distance and loading speed [2]. Other more advanced computer operated texture analysing systems or Stable Micro-system are also in use. They are software controlled and can display all the parameters mentioned above, and also the measured force.

2. The total soluble solids (TSS), which in mandarin, sweet oranges, grapefruit and pomelo juice are 80% to 85% constituted by sugars, are estimated in °Brix. The remaining part is composed of citric and other acids, and their salts, nitrogenous compounds, and other minor soluble substances such as water soluble vitamins [4]. Soluble solids can be identified by their refractive indices by using refractometers. These are calibrated to give °Brix or percentage TSS values directly. The refractometer needs to be calibrated with distilled water first. There is also a built-in auto-compensation system to correct for the increase in the refractive index of sugars with an increase in temperature [2].

3. The total acids, of which 80% to 95% consists of citric acid in various citrus fruits, also constitute most of the TSS in most of the acidic citrus fruits (lime, lemon, etc.). The sugar content in these cases are very low. Total acidity of juice and concentrates is determined as anhydrous citric acid and expressed as percentage per weight. The titration can be done by normal titration using NaOH and a pH meter to ascertain the endpoint (at pH 8.2), and calculated by

$$\begin{aligned}\text{Acidity}(\%) = &\frac{\text{Titre} \times \text{Normality of alkali} \times \text{Volume made up}}{\text{Volume of sample taken for estimation}} \\ &\times \frac{\text{Equivalent weight of citric acid } (64) \times 100}{\text{Weight or Volume of juice/pulp taken} \times 1000},\end{aligned} \tag{2.2.1}$$

or titrated directly by using a titrosampler.

4. The ratio of sugars to acids in fruit determines its relative sweetness or sourness. This is the maturity index for especially oranges, mandarines, grapefruit, pomelos, etc. Note that this index does not work for limes and lemons. At a ratio of 8 to 10 a grapefruit is relatively sweet, whereas an orange would be relatively sour to many people.

   As an example of relative sweetness/sourness two different cases are consider:
   ed 1. For 14% TSS against 1% acidity, the ratio is 14.
   2. For 14% TSS against 0.8% acidity, the ratio is 17.5.

   The fruit in the second case would be sweeter, because it has a higher sugar content compared to the acid. It should, however, be mentioned that the TSS:acid-ratio provides a better picture when presented with the TSS value (%). A ratio of 12 can be expressed as 12% TSS : 1% acid or 10% TSS : 0.83% acid, but the fruit in the first case would be tastier.

5. The pH of the juice is the hydrogen-ion concentration, and provides an estimate of the extent of acidity in the juice. A pH meter is used to measure the juice pH.

6. To measure ascorbic acid, the 2.6-dichlorophenol indophenol dye is reduced by ascorbic acid. In the same way the ascorbic acid in fruit juice can be estimated. A spectrophotometer uses the light to measure the absorbance of light in a solution of juice, dye and metaphosphoric acid (MPA). This enables one to deduce the concentration of ascorbic acid from the standard curve pre-established.

2.2.3 Non-destructive measurement instrumentation

Several methods and technologies are in use for the non-destructive testing of fruit quality. Both external and internal quality can be evaluated. Cameras are used to study the fruit colour, electromagnetic waves (visible light, X-ray radiation and tomography) and nuclear magnetic imaging to check internal defects. The degree of maturity can be measured on the basis of sugar content, firmness, and aroma by means of different on-line instruments [2].

2.2.3.1 External quality evaluation

These are external physical characteristics like color, shape, defects like malformation, etc. These characteristics have a psychological effect on consumers, who mistakenly think that the better a fruit looks from the outside, the better it is on the inside. These quality attributes are very important in automated sorting on commercial packing lines, where cameras and other means are used [2], [24], [25].

2.2.3.2 Internal quality evaluation

The internal quality is referred to as a combination of intrinsic properties based on chemical composition of the fruit and internal defects. The internal abnormalities

(such as internal breakdown, presence of seeds, granulation, rot, dehydration, worm holes, etc.) are the factors to be most careful of to preserve a product's reputation [5]. A number of techniques are available and amongst them are:

- Electromagnetic wave based techniques, which are sometimes used, and the transmittance and/or reflectance studied to extract information about the fruit quality. The frequencies exploited here are the visible spectrum, X-rays, sound, etc.

  X-ray transmittance detects variations in water density. It is successful in the case of large voids, freeze injury, and dehydration in fruit. Three-dimensional information can be obtained by performing a large number of radiographs on a rotating sample, and by reconstructing the volume of the sample by using filtered back-projection algorithms. This is called X-ray computed tomography (X-ray CT). A resolution of a few microns can be attained without sample preparation or chemical fixation [2].

  The visible light spectrum, coupled with intensified cameras or focused lasers, is likely to lead to future innovations. Light transmission measures internal fruit composition, and light fluorescence allows identification of damage.

  Near Infrared Radiation (NIR) spectroscopy, in transmittance mode, has been developed and can be used in packing houses. The transmittance spectra are taken through the equator of the fruit and maximum absorption is between 770 and 990 nm. It has been used to measure the TSS in Satsuma mandarines [26]. This system can also be used to measure citric acid concentration, but with less accuracy.

- NMR imaging (MRI) gives images that can be processed as visible ones. It detects differences in viscosity of liquids, such as oil and water. Worm holes, granulations and dry regions resulting from frost can also be visualised. MRI is the most successful technique for internal defect detection. It is the most suitable to view the depth of bruising or the location and presence of small seeds deep inside the fruit. Its use in industry at present remains impossible though, due to its high cost and the high level of technical expertise needed [18].

2.3 NMR application in fruit quality measurement and control

The NMR technique is sensitive to factors such as concentration, chemical environment, mobility and diffusion, related to certain nuclei. The first reported applications focused on the quantification of the main components, such as water and fat content, by NMR spectrometry [4]. Subsequent reports treated more complex analyses based on NMR relaxometry. MRI allows internal tomography, where tissue contrast arises mainly from differences in relaxation times and proton density [27].

2.3.1 Modes of operation

The derivatives or application study aspects of NMR are spectrometry, relaxometry and imaging [2].

- NMR spectrometry: The resonance frequency encodes the chemically equivalent nuclei populations at different electronic and chemical environments, so that the outcome is an NMR spectrum where intensity is plotted versus frequency [11].
- NMR relaxometry: Identifies nuclei populations distinguishable due to the different signal decay time constants, that is, relaxation times.
- NMR imaging: A devoted spatial codification of the signal intensity that produces a two- or three-dimensional image [28].

2.3.2 Types of NMR devices

Different types of devices have been developed by many scientists and have been used for a number of applications, amongst which are plant pathology, physiology, and quality evaluation of horticultural products [29].

1. Compact Nuclear Magnetic Resonance Microscope (CMRM): The MRM has been used for many studies in plant science, amongst which are studies of growth stages and growth conditions, effect of stresses, infection, storage, water transport and water balance, carbohydrate metabolism and secondary metabolites, and morphology and inner structure, etc. [30].
2. One-sided NMR System (NMR Mole): The NRM mole (MObile Lateral/Liquid Explorer) gets its inspiration from the NMR MOUSE (see below), but this uses a smaller magnetic field. It is specifically made for the exploration of solution samples. It is built on an array of barrel magnets with a central magnet positioned to provide a region of homogeneity.

   A set of discrete magnets are equidistantly spaced in a circular arrangement, tilted at an angle α to the normal of the ring plane. The adjustment of the tilt angle has a direct influence on the position or the strength of the homogeneous region, the size of which can be increased by an appropriate choice of the central magnet's dimensions. This configuration of tilted discrete magnets, instead of a continuous ring, reduces the cost. A compromise is, however, made on the field strength [31].

   Typical characteristics of such a system [31], within a rf bandwidth of 50 kHz, are as follows:

   > The magnet array gave a homogeneous field of 76.7 mT, centred at 15 mm from the array surface. The radius of the array of 8 cylindrical bar magnets (Macmill International, Nigbo, China) was 58.4 mm and the angle α was 11.5°. The diameter of the magnet array was 162 mm, the homogeneous region was approximately spherical in shape with a diameter of 20 mm. However, the volume contributing

to the overall signal depends on the sensitivity of the rf coil. The bar magnets were 50 mm long, 36 mm in diameter and the residual induction of the array was approximately 1.3 T. A central magnet of diameter 44 mm and length 4.5 mm was chosen to achieve the desired homogeneity. Further details of the specifications of this system can be found in [31], and a lot more about one-sided NRM systems in [32].

3. NMR-MOUSE (MObile Universal Surface Explorer): This design is described as a hand-held device with potential for on-line usage. It is a 5kg system composed of two permanent magnets, separated by a surface coil, which allows for high volume samples. It has been used for relaxation measurements and, by means of magnetic field gradients, spatially resolved characteristics of materials are obtainable in inhomogeneous magnetic fields of about 0.5T [4]. This system presents a disadvantage in that the sampling region is quite close to the surface, making it difficult to detect those properties that are distributed far from the surface of the fruit.

4. Open-access Halbach NMR: The Halbach system, in addition to being open access and hand-held like the MOUSE, does have another advantage in that it penetrates deeply into the sample and, like conventional NMR, acquires signals from the interior of the sample [24]. This is possible, because it is built on an array of permanent magnets in the "Halbach" configuration. Although moving the magnets apart presents the disadvantage of reduction of the field homogeneity, this is overruled by a number of advantages, such as [33]:

    - The open access configuration allows for the possibility of conducting the NMR measurements in parallel with other spectroscopic techniques such as FTIR, microscopy, X-ray, etc.
    - The relative ease of construction and low cost of the magnet.
    - Ease of portability of the magnet, which requires no steel yoke to carry flux lines.
    - Ease of access allows micro manipulation of the sample during measurements and allows special studies like rheology.
    - More space is available and this allows for moving samples in pipes.

There are many more NMR systems [34], [7], either conventional or with different particular designs. The NMR systems are designed depending on the intended use, and at present not a single all purpose NMR system exists. The overall concern is the need to improve the technology for industrial applications and the reduction of cost.

2.3.3 Summary of current studies of fruit quality using NMR

Fruit and vegetable NMR technique studies are mainly related to maturity and ripeness, internal damage and defects, and physiological disorders appearing during storage and caused by pre- and post-harvest conditions (see Table 2.3.3).

Product	**NMR type**	**Method**	**Attribute**	**Field**	**Ref**
Blueberry		T_1Null imaging	Freeze injury	7.1T	[35]
Grape	CMRM	MPI	Embryonic axis		[36]
		T_1-& T_2-weight,3D	Anatomy, Fungal inf.		[36]
		Sugar content	FID T_2-CPMG	0.2T	
Strawberry	CMRM	MPI	vasculature		[37], [10]
		Chemical shift image	sugars and oils		[38]
		T_1-weight, spin echo	Anatomy		[39]
		T_1-& T_2-weight,3D	Fungal infection		[37]
		IR se imaging		4.7T	[39]
		T_1-,PD-w. im.			
Stone fruits(drupes)					
Cherry	CMRM-	T_1-weight, diff. weight	Change of water status		[40]
		FID T_2-CPMG	Sugar content	0.2T	[41],[42]
		MRI	Bruises/voids/seeds		
		1-D se imaging	Quality eval(pits)	2T	[43]
Olive		MRI	Sugar content		
		Quality eval(pits)	1-Dse im.(250mm/s)	2T	[44]
Plum/prunes		MRS	Sugar content		
		FID spectrum		2T	[45]
Red raspberry		T_1-& T_2-weight, 3D	vascular bundles		[46]
Apple	–	MRR/MRI	Maturity/sugar content		
		MRI	Bruises/voids/seeds		
		se, ge imaging	Bruising	2T	[29], [47]
		T1, T2, PD(se)	Internal browning	0.6T	[48]
		T2-CPMG	Internal browning	0.13T	[49]
		se imaging	Superficial scald	4.7T	[50]
		MRI/MRR PD maps	Tissue breakdown		
		Proton image	Watercore formation		[28]
	CMRM	MPI	Watercore		[51]
	CMRM	3D, volume rendering	Watercore dissipation		
			Watercore	0.5T	[51], [28]
		T2-CPMG, PFGSE	Watercore	0.13T	[52]
		T2-CPMG, D_w	Ripeness(Brix)	0.13T	[52], [53]
		T2	Mealiness	2.3T	[54]
	CMRM	T_2 weight	Mealiness		
Avocado		MRS/MRI	Maturity/Brix		
		FID(0-250mm/s),MRS-T1	Dry matter	2T	[55], [56]
		FID T2-CPMG	Dry matter	0.13T	[57]
Banana		MRR	Maturity/Brix		
		T_2-CPMG, D_w	Ripening		[58]
Cherimoya		MRR(T1-IR)/T2-se im.	Matur./sugar cont.	4.7T	[59]
Coconut	CMRM	T_1-& T_2-weight	water & oils distribution		[60]

Durian	se imaging	Maturity-rots	0.5T	[61]
	MRS(FIDspec.300mm/s)	Maturity/Brix	2T	[62]
	MRI	Tissue breakdown		
Kiwifruit	T_1-& T_2-weight,3D	Vascular bundle rendering		[63]
	FID T1 and T2	Sugar content	Earth's field	[64]
	MRI/MRR	Chill injury		
	MRI	Infections		
	T1, T2(se mapping)	Maturity	2T	[65]
Mandarin	T1, T2, PD maps	Maturity	4.7T	[66]
	MRI	Bruises/voids/seeds		
Mango	T2(se mapping)	Maturity	4.5T	[1]
	FID spec 300mm/s	Maturity	2T	[62]
	se imaging	Infections	4.5T	[67]
	se imaging	Heat injury	4.5T	[68]
Mangosteen	se imaging	Maturity-rots	0.5T	[61]
	MRI	Infections		
Melon	se,ge imaging	Internal necrosis	2.0T	[69]
	single pulse, IRFT	Sugar content	4.7T	[70]
Nectarine	se,ge imaging	Wooly breakdown	0.5T	[71]
	MRR,PD maps	Fungal infection	4.7T	
Orange	se imaging	Bruises	2T	[29]
	FID, T_2-CPMG	sugar content	0.13T	[57]
	MRI	chill injury		
Papaya	se T1-,T2-,PD weigh.im.	heat injury	1.5T	
Pear -	T1-,se,Proton image	Core breakdown	0.5T,4.7T	[27]
	se imaging	Bruising	2T	[29]
	FID spec.(300mm/s)	Firmness	2T	[62]
Peach	se imaging	Bruising	2T	[29],[69]
		Mealiness	4.7T	[72]
	MRR/MRI	Chill injury		
Persimmon	Proton image	Chilling injury		[73]
Pineapple	T2& se imaging	Maturity/Ripening	2T	[29],[69]
Tangerine	se imaging	Quality disorders	0.5T	[74]
	MRI	Maturity		
Watermelon	1D-proj.,se im.(350mm/s)	Voids	0.5T	[75]
	T_1& T_2 vol-selected	Sugar content	0.5T	[75]
Zucchini Squash	T^1-& T^2-weight	Chilling injury		[76]
Courgette/Zucchini	T1& T2 w. se im.	Chill injury	4.7T	[76]
Cucumber	T_1se mapping	Chill injury	0.6T	[77]
	se imaging	Pathogen invasion	2T	[69]
Mushroom	T^1-& T^2-weight	Air space in tissues, structure		[78]
Onion	se imaging	Bruises	2T	[29]
Potato	1-D& se imaging	Hollow heart	4.7T	[79]
	T_1-IR,T_2-CPMG	Dry matter	7T	[80]
	T_2	Sensory texture	0.5T	[81]
	se,ge imaging	Disease	7T	[82]

Tomato	CMRM	T1-weight,localized	Change of water status		[83]
		T_2-weight	Water content		[84]
		se image	Maturity	2T	[29],[85]
		T_1& imaging		6.3T	[86],[83]
		MRI-se,ge	Firmness	0.2T	[87]
		MRS-T_1 IR,T_2		0.6T	

Table 2.2: An overview of applications of the NMR to fruits and vegetables

2.4 Summary

This chapter outlined the theoretical background of the NMR technique. The theoretical principles of nuclear magnetic resonance, the applications of NMR, in general and in particular to horticultural products, are presented. The concept of fruit quality testing and control is reviewed and a summary of the application of NMR to fruits, at both high- and low field, is given.

NMR is based mainly on the response of nuclear spins to an externally applied magnetic field and an rf pulse, which is at the origin of the generated signal. The NMR signal is converted to an interpretable spectrum, where every peak represents a specific resonance frequency, in order to provide the necessary information. The relaxation times and the chemical shifts play a big role in the interpretation of the spectrum and the images obtained by NMR.

The many applications of the NMR range from agriculture, material science, to medical science and have proved to be a very powerful tool.

Chapter 3

Superconducting circuit building blocks and simulations

Like any other superconducting circuits, SQUIDs are built by building blocks known as Josephson junctions. To understand the working principles of SQUIDs, one has to understand how the Josephson junctions functions. In this chapter a brief theoretical background on superconductivity, the Josephson junction, and the theory of SQUIDs is given.

The fabrication of a SQUID requires an understanding of its operational flexibilities, the choice of parameters, and the prediction and meaning of experimental results. This is possible through the simulation of the equivalent circuits of the Josephson junction and the SQUID.

Simulations have been done using the analogue behavioural modelling facility of the NGSpice circuit simulator, together with Matlab software for plotting the results. All the simulation results are reported in this chapter, and are compared to the expected theoretical behaviour of the respective circuits.

3.1 Superconductivity

3.1.1 General aspects

In 1911 Kamerlingh Onnes observed, for the first time, that some metals and alloys showed a sharp drop in resistivity when cooled down in liquid helium (4.2K). In a conductor, below a critical temperature (T_c), the resistance becomes zero, so that a current can flow indefinitely with an immeasurable attenuation (perfect conductivity) [88]. Typical critical temperatures vary between 135K (HBCCO) and 0.001K (Rh), [89], [90]. This phenomenon is known as superconductivity. A superconducting material is also characterized by a critical current density (J_c) and a critical magnetic field strength (H_c), above which the superconductivity disappears. Some superconductors display two values of critical magnetic field, H_{c1} and H_{c2}, between which the material state is a mixture of a normal state and a superconducting state. In this state the material is threaded by vortices of magnetic flux. Below H_{c1} the

material is superconducting and above H_{c2} it is in the normal state. Materials of this type are called Type II superconductors, while pure/conventional superconductors are of Type I.

In addition to perfect conductivity, superconductivity is also characterized by perfect diamagnetism, where a material in its superconducting state will expel all the magnetic field applied to it. This is known as the Meissner effect [88].

The conduction electrons in a superconductor are in an ordered state, such that the electrons pair up in doublets (Cooper pairs), which behave coherently in such a manner that they can be described by a single quantum wave function.

3.1.2 High-temperature superconductors

Before 1986 it was believed that 23.2K (T_c of Nb_3Ge) was the maximum value of the critical temperature of superconductors, until J.G. Bednorz and K.A. Muller [91] discovered the first high-temperature superconductor LBCO ($La_{1.85}Ba_{0.15}CuO_4$), with $T_c = 30$K. Higher critical temperatures are attained nowadays and many HTSs, like YBCO ($YBa_2Cu_3O_{7-\delta}$), with $T_c = 92$K, reach their critical temperature in liquid nitrogen. Extensive research is ongoing though, in the hope of finding room temperature superconductors.

High-T_c superconductors are anisotropic and this can result in weak links, where the lattice is misoriented. Controlled misorientation can be exploited to make Josephson junctions. Most HTSs have perovskite crystal structures with CuO_2 planes (see Fig. 4.6), the primary contributing factor to superconductivity. The layered structure of HTS materials leads to anisotropic conductivity, higher along the *ab*-plane than in the *c*-axis direction. Other parameters like Λ and ξ are also anisotropic (dependent on the orientation). Anisotropy is important in the manufacture of planar superconducting devices, especially in the case of Josephson junctions [91].

3.1.3 Theory development

A number of models have been developed to explain all aspects of the phenomenon of superconductivity, from the apparent behaviour to the physical reasons for the occurrence of superconductivity.

3.1.3.1 Classical model

This model is derived from the electrodynamic equations of Maxwell, and explains some aspects of superconductivity, such as perfect conductivity and perfect diamagnetism.

Maxwell's equations in free space, in their differential form, are given by

$$\nabla \times \mathbf{E} = -\frac{\partial \mathbf{B}}{\delta t} \quad \text{(Faraday's law)} \tag{3.1.1}$$

$$\nabla \times \mathbf{H} = \frac{\partial \mathbf{D}}{\partial t} + \mathbf{J} \quad \text{(Ampere's law)} \tag{3.1.2}$$

$$\nabla \cdot \mathbf{D} = \rho \quad \text{(Gauss's law for the electric field)} \tag{3.1.3}$$

$$\nabla \cdot \mathbf{B} = 0 \quad \text{(Gauss's law for the magnetic field),} \tag{3.1.4}$$

where $\mathbf{B} = \mu\mathbf{H}$ and $\mathbf{D} = \epsilon\mathbf{E}$, ϵ is the permitivity and μ is the permeability of the material.

Considering that the dimensions of a structure is much less than the wavelength of the electromagnetic field interacting with it, the coupling between the two fields becomes very weak, and the quasistatic approximation is allowed [92]. Such approximations can be adopted to simplify the difficulties encountered in solving equations involving second-order derivatives in wave functions. In superconductors the current flows freely, and a magnetoquasistatic (MQS) approximation can be assumed.

In this approximation Maxwell's equations are expressed as

$$\nabla \times \mathbf{E} = -\frac{\partial \mathbf{B}}{\delta t} \tag{3.1.5}$$

$$\nabla \times \mathbf{H} \approx \mathbf{J} \tag{3.1.6}$$

$$\nabla \cdot \mathbf{J} = \nabla \cdot (\nabla \times \mathbf{H}) = 0 \text{(Currents circulate in closed loops)} \tag{3.1.7}$$

$$\nabla \cdot \mathbf{B} = 0. \tag{3.1.8}$$

Ohm's law in field theory and the classical equation for an electron moving in an electromagnetic field are respectively given by

$$\mathbf{J} = \sigma\mathbf{E} \tag{3.1.9}$$

and

$$m\frac{d\mathbf{v}}{dt} = e[\mathbf{E} + (\mathbf{v} \times \mathbf{B})] - \frac{m}{\tau}\mathbf{v}. \tag{3.1.10}$$

Combining (3.1.9) and (3.1.10), and considering that the scattering time constant $\tau \to \infty$ for a perfect conductor, and that the supercurrent density is given by $\mathbf{J} = e^* n^* \mathbf{v}^*$, we get the relationship

$$\mathbf{E} = \frac{d}{dt}[\frac{m^*}{n^* e^{*2}}\mathbf{J}^*] = \frac{d}{dt}(\Lambda \mathbf{J}^*). \tag{3.1.11}$$

The * means that the quantity refers to superelectrons, and Λ is the inertia of the superelectrons. This equation (3.1.11) is known as London's first equation (London I), and is Ohm's law applied to the limit, and thus describes perfect conductivity [92].

To describe perfect diamagnetism, the time derivative of the curl of Ampere's law is taken, and Faraday's law is applied to get a representation of a magnetic field inside a uniform, non-dispersive material. The expression

$$\left(\frac{\mu_0}{\Lambda} - \nabla^2\right)\frac{\partial}{\partial t}\mathbf{H} = 0 \tag{3.1.12}$$

is obtained.

From the quantity $\frac{\mu_0}{\Lambda}$ a penetration depth, $\lambda = \sqrt{\frac{\Lambda}{\mu_0}}$, also called the London penetration depth, is derived. This is the distance that the magnetic field can penetrate into a superconducting material. It is similar to the skin depth (δ), but it is frequency independent.

Simple manipulation of (3.1.12) in a static field leads to the relationship

$$\nabla \times (\Lambda \mathbf{J}) = -\mathbf{B}, \tag{3.1.13}$$

known as London's second equation (London II). London II postulates that flux expulsion will always occur in a superconductor [92].

A consideration that has been ignored thus far is that superconductivity is a thermodynamic process. The penetration depth was experimentally shown to be temperature dependent [93], and given by

$$\lambda(T) = \frac{\lambda_0}{\sqrt{1-(T/T_c)^4}}, \text{for} \quad T \leq T_c. \tag{3.1.14}$$

Once a superconductor is cooled down below its critical temperature, two types of "fluids" (electron gases) appear, namely normal electrons and superelectrons. From (3.1.11) and (3.1.14) it is apparent that n^* depends on the temperature. The proportions of the two fluids deduced from (3.1.14), are given by

$$n^*(T) = n_0^* \left(1 - (\frac{T}{T_c})^4\right) = \frac{1}{2} n_{tot} \left(1 - (\frac{T}{T_c})^4\right), \tag{3.1.15}$$

and

$$n(T) = n_{tot} \left(\frac{T}{T_c}\right)^4, \tag{3.1.16}$$

with $n_{tot} = n(T) + 2n^*(T)$ for all T, and $n(T)$ the temperature dependent number of normal electrons. It is assumed that, at 0K, no electron is unpaired.

The current thus flows in two branches, so that the total current density would be given by

$$\mathbf{J} = \mathbf{J}_n + \mathbf{J}_s, \tag{3.1.17}$$

with $\mathbf{J}_n$ and $\mathbf{J}_s$ being, respectively, the normal and the supercurrent densities.

Orlando and Delin [93] showed the equivalence of a series RL circuit and an ohmic conductor. In the limit, a perfect conductor is modelled as a simple inductor L. Consequently the channels of currents can be represented in a **two-fluid model** as a series RL combination (normal channel) in parallel with a single inductor for the supercurrent channel. Figure 3.1 illustrates such a circuit.

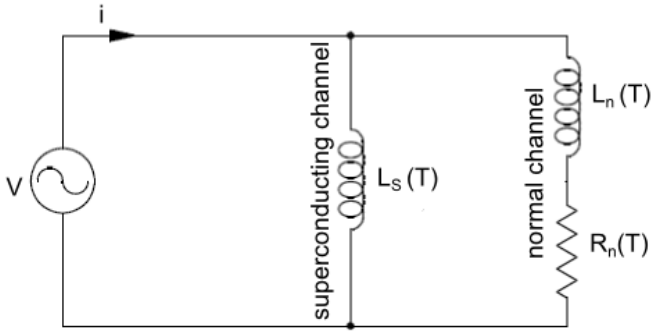

Figure 3.1: The equivalent circuit of the two-fluid model [92]

3.1.3.2 Macroscopic Quantum Model

Though the classical model is useful, it does not explain the phenomenon of superconductivity in depth, as it does not incorporate a number of properties and it formulates a quantum phenomenon in a classical way.

The Macroscopic Quantum Model (MQM) is built on the hypothesis that all the Cooper pairs are described by a single wave function $\Psi(\mathbf{r},t) = \widehat{\Psi}e^{i(\mathbf{k}.\mathbf{r}-\omega t)}$. This is due to the fact that, once the electrons pair up, they all behave in a coherent way.

The macroscopic quantum model encompasses the classical model and includes a self-consistent description of more properties of superconductivity. For example, it allows magnetic flux quantization of vortices threading the superconductor, especially encountered in Type II superconductors in the mixed state, which is a violation of the Meissner effect [93]. In this model the electromagnetic and thermodynamic properties of superelectrons are combined.

To establish the MQM model one starts with the Schrödinger equation, given by

$$i\hbar\frac{\partial\Psi}{\partial t} = -\frac{\hbar^2}{2m}\nabla^2\Psi + V(\mathbf{r})\Psi. \tag{3.1.18}$$

The square of the wave function magnitude is known as the probability of a quantum particle to be located at a point $\mathbf{r}$ in space at a time t, and is given by

$$\wp = \Psi^*(\mathbf{r},t)\Psi(\mathbf{r},t) = |\Psi(\mathbf{r},t)|^2 = n^*(\mathbf{r},t), \tag{3.1.19}$$

where n^* is the local density of superelectrons, $\Psi^*(\mathbf{r},t)$ is the conjugate of the wave function, and $\int \wp dv = 1$.

$\wp$ can only flow from one point to another, and its time-space evolution is derived from (3.1.18) as

$$\frac{\partial\wp}{\partial t} = -\nabla\cdot\mathbf{J}_p, \tag{3.1.20}$$

where the probability current is given by

$$\mathbf{J}_p \equiv \frac{\hbar}{2im}(\Psi^*\nabla\Psi - \Psi\nabla\Psi^*) = Re\Psi^*\frac{\hbar}{im}\nabla\Psi. \tag{3.1.21}$$

From Lorentz's law, Faraday's law and Gauss' law, we can rewrite the probability current of a charged particle in an electromagnetic field as

$$\mathbf{J}_p = \mathrm{Re}\Psi^* \left(\frac{\hbar}{im} \nabla - \frac{q}{m} \mathbf{A} \right) \Psi, \tag{3.1.22}$$

with $\mathbf{A}$ the magnetic vector potential.

In analogy to (3.1.22) the supercurrent can now be derived as

$$\mathbf{J}_s = e^* n^*(\mathbf{r}, t) \left(\frac{\hbar}{m^*} \nabla \theta(\mathbf{r}, t) - \frac{e^*}{m^*} \mathbf{A}(\mathbf{r}, t) \right). \tag{3.1.23}$$

Schrödinger's equation for the superelectrons can now be expressed as

$$i\hbar \frac{\partial}{\partial t} \Psi \mathbf{r}, t = \frac{1}{2m^*} \left(\frac{\hbar}{i} \nabla - e^* \mathbf{A} \right)^2 \Psi(\mathbf{r}, t) + e^* \phi(\mathbf{r}, t) \Psi(\mathbf{r}, t), \tag{3.1.24}$$

where the real part of the expression is known as the energy-phase relationship, given by

$$-\hbar \frac{\partial \theta}{\partial t} = \frac{1}{2n^*} \Lambda \mathbf{J}_s^2 + e^* \phi, \tag{3.1.25}$$

with ϕ the scalar potential.

Replacing the expression for Λ, as previously defined, in the equation above, and taking the curl of the gauge invariant current expression, we recover London II,

$$\nabla \times \Lambda \mathbf{J}_s = -\mathbf{B}. \tag{3.1.26}$$

By taking the time derivative instead and replacing (3.1.25), we get

$$\frac{\partial (\Lambda \mathbf{J}_s)}{\partial t} = \mathbf{E} - \frac{1}{n^* e^*} (\frac{1}{2} \Lambda \mathbf{J}_s^1) \tag{3.1.27}$$

which closely resembles London I , but with an additional non-quantum term due to the fact that a magnetic term was ignored in the original derivation of London I [92].

Another aspect of the MQM is **flux quantization** as a quantum mechanical consequence of the model. If the supercurrent (3.1.23) is integrated along a closed loop C, covering a surface S, and if Stokes' theorem is applied, we get the expression

$$\oint_c (\Lambda \mathbf{J}_s) \cdot dl + \int_s \mathbf{B} \cdot ds = \frac{\hbar}{e^*} \oint_c \nabla \theta \cdot dl. \tag{3.1.28}$$

As $\oint_c \nabla \theta \cdot dl$ can only take values that are multiples of 2π, the expression becomes

$$\oint_c (\Lambda \mathbf{J}_s) \cdot dl + \int_s \mathbf{B} \cdot ds = 2\pi n \frac{\hbar}{e^*} = n \Phi_0. \tag{3.1.29}$$

If the path of integration is chosen deeper than the London penetration depth, the current will be zero, due to the Meissner effect. The flux in a hole surrounded by a superconducting material will thus always be quantized.

3.1.3.3 BCS theory

In 1957 Bardeen, Cooper and Schrieffer (BCS) laid the foundation for a quantum theory of superconductivity. The BCS theory explains the pairing of electrons as follows:

> "An electron interacts with the lattice, which results in a phonon. The latter makes a neighbouring electron interact accordingly, and in the end the two electrons team up. An attractive interaction between two electrons can lead to a ground-excited states energy gap, which results in the characteristic properties, such as the critical field, thermal and most of the electromagnetic properties."

The coherence length introduced in (3.1.3.4) and the penetration depth emerge as natural consequences of the BCS theory [88], and all the other properties described in the previous sections are obtained under different approximations.

3.1.3.4 Ginzburg-Landau theory

Ginzburg and Landau (GL) formulated a phenomenological theory of the superconducting state and its spatial variation of the **order parameter** $\Psi(\mathbf{r})$. They extended the Abrikosov theory to describe the vortex state, which is practically exploited in superconducting magnets. The introduction of the coherence length (ξ) and the wave function used in the Josephson effect constitute the attractive aspects of the GL theory [88]. The coherence length is a measure of the distance within which the superconducting electron concentration cannot change drastically in a spatially changing magnetic field. A dimensionless ratio, $\kappa = \lambda/\xi$, is used to classify the superconductors as Type I ($\kappa < 1/\sqrt{2}$) or Type II ($\kappa > 1/\sqrt{2}$).

Though the BCS theory and its extensions successfully describe conventional superconductors, they fail when it comes to explaining some mechanisms, such as the electron pairing in high-temperature superconductors [94].

3.2 Josephson junctions

A Josephson junction is generally represented by two superconductors separated by a very thin layer of insulating material, constituting a weak link, as shown in Fig. 3.2. These junctions can be either extrinsic or intrinsic. Extrinsic Josephson junctions are mainly made of "non-superconducting" materials, such as insulators (I), normal conductors (N), semiconductors (Se) or a superconductor with a different I_c (S'), sandwiched between two superconductors. Some examples are SIS, SNS, SSeS and SS'S structures.

In intrinsic Josephson junctions weak links are made from the inherent properties of the superconductor, such as microbridges, grain boundaries, etc.

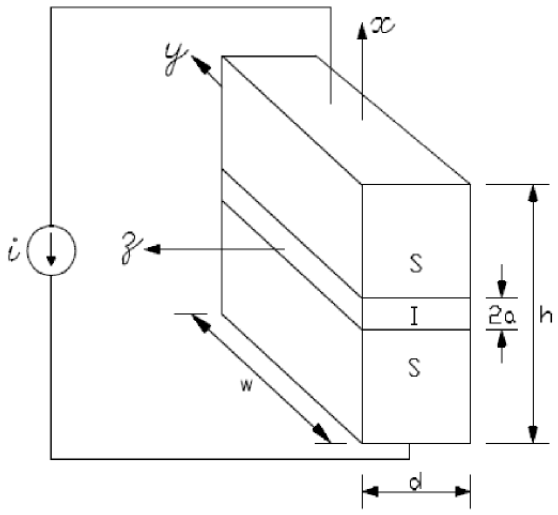

Figure 3.2: Schematic representation of a Josephson junction

3.2.1 Josephson superconductor tunnelling

The principle property exploited in Josephson junctions is the switching of the junction to a resistive state and vice versa under specific conditions. For the junction to exhibit resistive behaviour, normal electrons need to tunnel. This requires breaking Cooper pairs, which is achieved at an energy of at least 2Δ, the energy gap of the superconductor. The junction thus needs to be at a voltage $v > 2\Delta/e$. In order to describe the behaviour of the Josephson junction, one needs to derive the current-phase relationship.

3.2.1.1 DC Josephson effect

In 1962 the phenomenon of Cooper pair tunnelling through a thin insulating layer intercalated between two superconductors was announced. As Brian Josephson predicted, superelectron tunnelling resulted in a dc current in absence of voltage. This is known as the dc Josephson effect.

Let the respective wave functions on the two sides of a Josephson junction be given by Ψ_1 and Ψ_2. Assuming that the potential is zero on both sides of the junction, the time dependent Schrödinger equation is applied to render

$$i\hbar\frac{\partial\Psi_1}{\partial t} = \hbar T\Psi_2 \quad \text{and} \quad i\hbar\frac{\partial\Psi_2}{\partial t} = \hbar T\Psi_1, \tag{3.2.1}$$

where T is a measure of the leakage of the probability amplitudes to the other side of the junction, and T=0 for a thick insulator. Recall that $|\Psi|^2 = n^*$. It is then appropriate to write that $\Psi_i = \sqrt{n_i^*}e^{i\theta_i}$. The current-phase relationship can then be derived as

$$\mathbf{J} = \mathbf{J}_c \sin\phi, \tag{3.2.2}$$

where $\phi = \theta_2 - \theta_1$, the phase difference between the two interfaces of the junction. In this case a dc current flowing through the junction is bound between $\mathbf{J}_c$ and $-\mathbf{J}_c$, depending on the value of ϕ [88]. $\mathbf{J}_c$ is the maximum current density allowed through the junction without a voltage being generated. It is proportional to the transfer interaction and given by $\mathbf{J}_c = 2T\sqrt{n_1^* n_2^*}$.

3.2.1.2 AC Josephson effect

When a dc voltage (V) is applied over a Josephson junction, the potential can no longer be zero. A superelectron experiences a potential energy difference of -2eV upon crossing the junction. A Cooper pair would thus be at $\pm e$V on one of the sides. Figure 3.3 shows the phenomenon of tunnelling in terms of current and voltage.

The equations of motion consequently become

$$i\hbar\frac{\partial\Psi_1}{\partial t} = \hbar T\Psi_2 - eV\Psi_1 \quad \text{and} \quad i\hbar\frac{\partial\Psi_2}{\partial t} = \hbar T\Psi_1 + eV\Psi_2. \tag{3.2.3}$$

The applied voltage will induce a change in the phase difference, the current will oscillate at a frequency $\omega_j = 2eV/\hbar$ and the supercurrent becomes

$$\mathbf{J} = \mathbf{J}_c \sin\left(\phi(0) - \frac{2eV}{\hbar}t\right) = \mathbf{J}_c \sin\left(\phi(0) - 2\pi f_j V t\right), \tag{3.2.4}$$

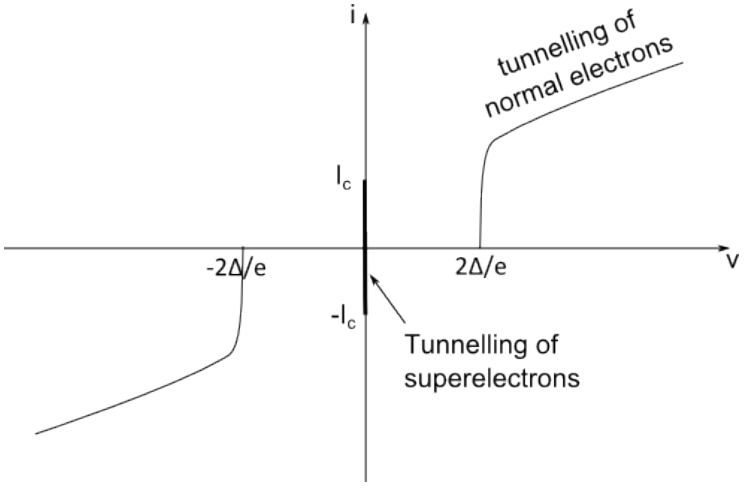

Figure 3.3: The I-V curve for a Josephson junction. The current at zero voltage represents the Josephson current.

where $f_j = \omega_j/2\pi$ is called the Josephson frequency and is equivalent to 483.60×10^{12} V.Hz. The current through a Josephson junction thus oscillates at 483.6 MHz per μV applied. From (3.2.4) we find that the phase is given by $\phi = \phi(0) + \frac{2eV}{\hbar}t$, and the voltage-phase relationship thus becomes

$$V = \frac{\Phi_0}{2\pi}\frac{\partial\phi}{\partial t}. \tag{3.2.5}$$

The energy ε_j in the junction is given by

$$\varepsilon_j = \int_0^{t_0} iV dt = \varepsilon_j(0) - \frac{\Phi_0 I_c}{2\pi} cos\phi \tag{3.2.6}$$

where $\varepsilon_j(0) = \Phi_0 I_c/2\pi$ is the coupling energy between the two electrodes with no applied current.

3.2.2 Magnetic fields effect

When a magnetic field is applied perpendicular to the junction, and threading the junction, the dc critical current of the junction is sinusoidally modulated along the junction interface. The magnetic field induces a linear gradient in the gauge invariant phase difference, and the critical current is reduced accordingly [95]. The total flux that would thread a junction of width W, length d, exposed to a perpendicular magnetic flux density B, is given by

$$\Phi_B = W(d + 2\lambda)B. \tag{3.2.7}$$

In (3.2.7) the penetration depth of the material is taken into account and the effective length thus becomes $d + 2\lambda$. For simplicity the self-induced field from the current is ignored and only the applied component (B) [93] is considered. The maximum current is then derived as

$$i_{max}(\Phi_B) = I_c(B) = I_c(0) \left| \frac{\sin\left[\pi(\frac{\Phi_B}{\Phi_0})\right]}{\pi(\frac{\Phi_B}{\Phi_0})} \right|, \tag{3.2.8}$$

where $I_c(0)$ is the critical current when no magnetic field is applied. Figure 3.4 shows the dependence of if the junction total current to the magnetic flux threading the junction.

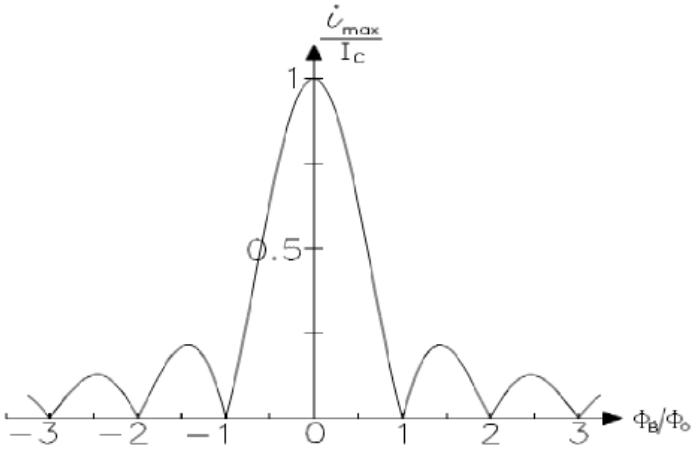

Figure 3.4: Interference pattern of a single junction without self-fields.

3.2.3 RCSJ model

Given the differences in the types of Josephson junction, there is no common universal current-voltage relation for an arbitrary junction. Models are required to solve the dynamics problems, providing an approximation of the real properties of the junction. One of these models, the resistively and capacitively shunted junction (RCSJ) model, has become important, because it quantitatively describes the behaviour of all junction types with consideration of secondary effects, such as resistance/inductance shunting and capacitance [96], [91]. This model splits the normal channel of (3.1.17) into a resistive channel and a capacitive channel.

Low-T_c multilayer Josephson junctions have non-negligible intrinsic capacitance and the RCSJ model is appropriate for this purpose, and the equivalent circuit of such a junction is illustrated in Fig. 3.5. On the other hand, for some high-T_c single junctions, where the capacitance is zero, the RSJ model for resistively shunted junctions is suitable.

The normal conductance of the entire junction is given by

$$G_n = \frac{1}{R_n} = \frac{2\hbar}{\Phi_0 \Delta} I_c, \tag{3.2.9}$$

where Δ is the gap energy. The product $V_c = I_c R_n$ is an important parameter for characterising Josephson junctions and SQUIDs.

The capacitive channel results from the capacitor effect between two parallel plates, and the capacitance is usually given by $C = \frac{\epsilon A}{2a}$, where A is the area of the electrode, $2a$ the thickness of the junction, and ϵ the dielectric constant of the insulating layer of the junction.

The total current due to the three parallel channels can be written as

$$\begin{aligned} i &= I_j + I_R + I_d & (3.2.10)\\ &= I_c \sin\phi + V G_n + C\frac{dV}{dt}. & (3.2.11) \end{aligned}$$

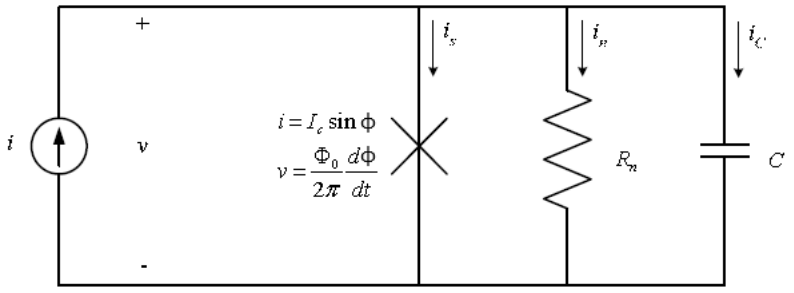

Figure 3.5: Circuit model of the RCSJ model

Substitution of (3.2.5) into (3.2.10) leads to

$$\frac{i}{I_c} = \sin\phi + \frac{\Phi_0}{2\pi}\frac{1}{I_c R_n}\dot{\phi} + \frac{\Phi_0}{2\pi I_c}C\ddot{\phi} \tag{3.2.12}$$

$$= \sin\phi + \tau_j\dot{\phi} + \frac{\Phi_0}{2\pi I_c}\frac{\tau_{RC}}{R_n}\ddot{\phi}. \tag{3.2.13}$$

The value of the ratio of the time constants $\tau_j = 1/\omega_j = \frac{\Phi_0}{2\pi}\frac{1}{I_c R_n}$ and $\tau_{RC} = R_n C$ determine the response of the junction. This is known as the Stewart-McCumber parameter or the damping parameter, and denoted by β_c

$$\beta_c = \frac{\tau_{RC}}{\tau_j} = \frac{2\pi I_c R_n^2 C}{\Phi_0} \tag{3.2.14}$$

The value of β_c determine the characteristic behaviour of the Josephson junction.

3.2.3.1 Overdamped junction

When $\beta_c << 1$, the junction has a zero capacitance, but there will always be a shunt normal resistance. The RSJ model is thus appropriate to adopt.

The current now becomes

$$i = I_c \sin\phi + \frac{\Phi_0}{2\pi}\frac{1}{R_n}\dot{\phi}, \tag{3.2.15}$$

and the equivalent circuit corresponding to this case is shown in Fig. 3.6.

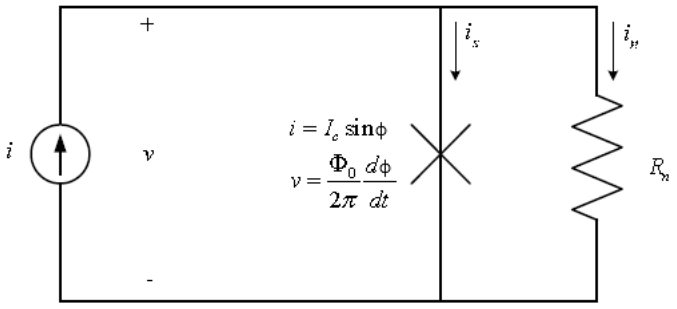

Figure 3.6: Circuit model of an overdamped junction. The current source is interchangeable with a voltage source.

For $I < I_c$, no voltage drop appears across the junction. In the case of $I > I_c$ the voltage changes in time due to the change in the phase, and the oscillating time dependent voltage is given by

$$v(t) = V_c \frac{\left(\frac{I}{I_c}\right)^2 - 1}{\left(\frac{I}{I_c}\right) + \cos\omega t}. \tag{3.2.16}$$

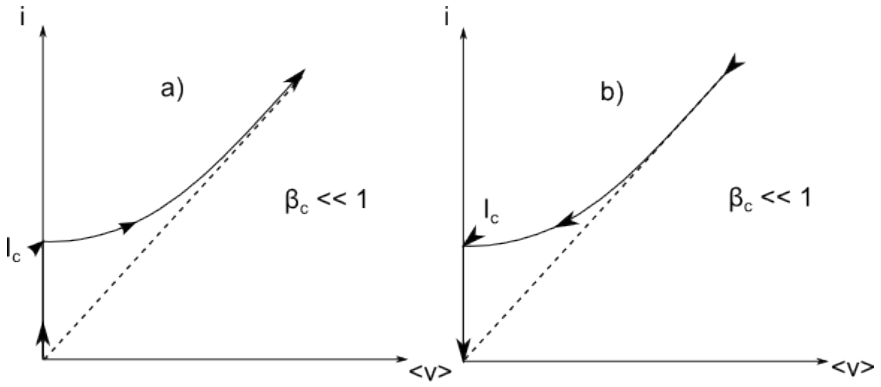

Figure 3.7: The current-voltage characteristic of an overdamped junction. The curve is single-valued for an increasing and decreasing current.

The time averaged voltage is thus deduced as

$$\langle v(t)\rangle = V_c\sqrt{\left(\frac{I}{I_c}\right)^2 - 1}. \tag{3.2.17}$$

The frequency of the voltage across the junction is given by $f = \langle V(t)\rangle/\Phi_0$.

The voltage response to a rising current in overdamped junctions overlaps with that of the falling current, thus no hysteresis is observed, as shown by Fig. 3.7. This is common in intrinsic high-T_c Josephson junctions and they are preferable for SQUID applications [97].

3.2.3.2 Damped junction

A non-limiting damping case occurs when $\beta_c \sim 1$ and the RC part of the junction circuit is taken into account.

When no current is flowing through the shunt resistor, the time-average voltage across the junction remains at zero, while the current flowing through the junction remains below the critical current $I < I_c$. When the current rises above I_c, a voltage drop appears across the junction, and the junction switches at a voltage $2\Delta/e$.

The system transits into a nonlinear dc response, and will only return to zero potential when the current flowing through the junction drops below the minimum return current threshold, $I < I_r$, and the RC circuit has dissipated all of its energy. For certain values of β_c the damped junction will exhibit hysteretic I-V behaviour, as shown in Figure 3.8.

As β_c increases from 0, the return current (I_r) will decrease from I_c down to 0, resulting in a larger hysteresis response. The value of β_c can be approximated in terms of I_r as

$$\beta_c = 2\left(\frac{I_c}{I_r}\right)^2 + (2-\pi)\frac{I_c}{I_r}. \tag{3.2.18}$$

In multilayered devices a secondary shunt resistor can be used to reduce β_c to get a non-hysteretic junction.

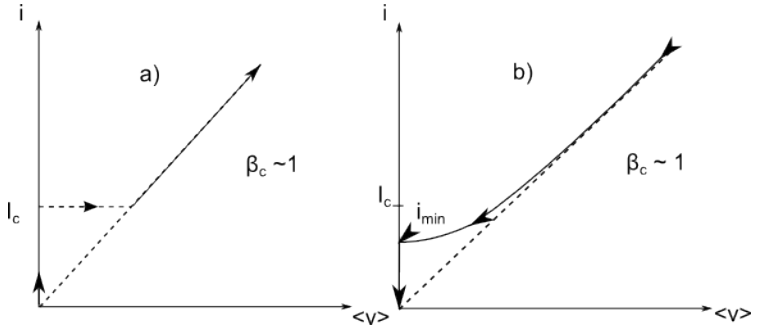

Figure 3.8: The current-voltage characteristic of a critically damped junction. The curve is hysteretic.

3.2.3.3 Underdamped junction

In underdamped junctions, the RC channel is dominant, determining the junction dynamics. The capacitance C is very large, which results in $\beta_c >> 1$. This is commonly encountered in layered junction structures, or junctions with an interface [91]. For currents less than the critical current, no voltage drop appears across the junction. The dc component of the junction's voltage response to the current, when the value of I exceeds I_c, is expressed as

$$\langle v(t) \rangle = IR_n. \tag{3.2.19}$$

Figure 3.9 shows the curve of the voltage response to the current in an underdamped junction. The junction displays hysteretic behaviour.

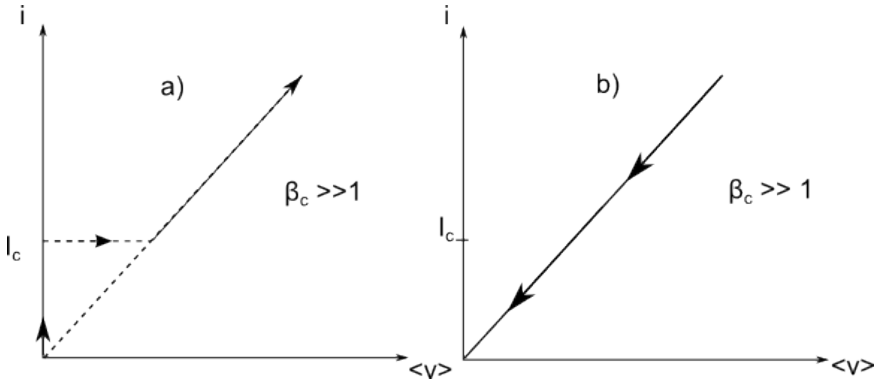

Figure 3.9: The voltage-current characteristic of an underdamped junction. For a decreasing current from above I_c, the the characteristic is totally resistive.

3.2.3.4 Response to AC driving sources

The junction behaviour described thus far, has been in a context where a dc source is used to drive the junction. When a dc voltage source is used, the time-averaged current is just that voltage divided by the resistance. This resistance is the slope of the I-V curve, which is linear [93].

When an ac driving source is used the scenario becomes different. Here we start with an ac voltage source given by

$$v(t) = V_0 + V_s \cos(\omega_s t). \tag{3.2.20}$$

The resulting current across the junction is given by

$$i_j(t) = I_c \Sigma_{n=-\infty}^{+\infty} (-1)^n J_n \left(\frac{2\pi V_s}{\Phi_0 \omega_s} \right) \sin[(2\pi f_j - n\omega_s)t + \varphi(0)], \tag{3.2.21}$$

and the total current i can be expressed as

$$i = i_j + i_R = i_j + \frac{V_0}{R} + \frac{V_s}{R} \cos(\omega_s t). \tag{3.2.22}$$

The average current is thus given by

$$\langle i \rangle = \frac{V_0}{R} + I_c \Sigma_{-\infty}^{+\infty} (-1)^n J_n \left(\frac{2\pi V_s}{\Phi_0 \omega_s} \right) \sin \varphi(0) \delta_{2\pi f_j, n\omega_s}. \tag{3.2.23}$$

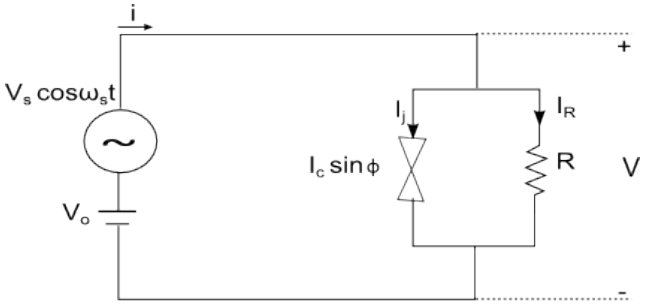

Figure 3.10: Dc and ac voltage sources applied to a RSJ circuit. The junction voltage V is given by (3.2.5)

The I-V curve is the sum of a straight line and current spikes corresponding to the effect of the resistor and the basic Josephson junction respectively [93]. The current spikes will appear at voltage steps of

$$V_0 = n(\frac{\Phi_0}{2\pi})\omega_s. \tag{3.2.24}$$

The voltage source in Fig. 3.10 is interchangeable with a current source. When a current source is used, such that

$$i(t) = I_o + I_s \sin \omega_s t, \tag{3.2.25}$$

the average dc voltage will remain zero as the dc component of the driving current I_0 is increased from zero to the height of the current spike. As the latter is exceeded, the voltage increases at a rate of the slope of the resistance, up to the next spike, and so on. The result is an I-V curve in the shape of a staircase, called Shapiro steps. Figure 3.11(b) shows the graph in such a situation. It is important to note that (3.2.24) also holds in this case.

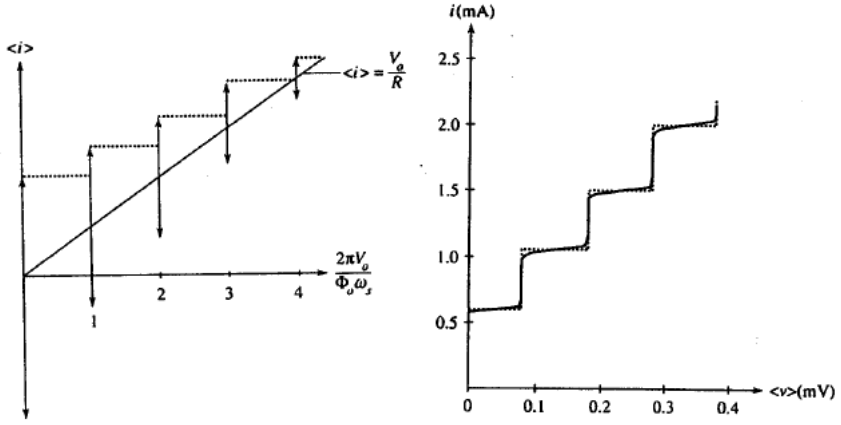

Figure 3.11: Ac response I-V curves when both dc and ac voltage driving sources are used (left), and an ac current source is driving the junction (right) [93].

For a generalized junction (adjusted to $\beta_c << 1$) driven by an ac current source, the current of the driving source is given by

$$\frac{d}{dt}i(t) = L_J v(t) + \frac{1}{R}\frac{d}{dt}v(t), \tag{3.2.26}$$

where L_j is the Josephson inductance and approximately given by

$$L_J = \frac{\Phi_0}{2\pi I_c\sqrt{1-(I_0/I_c)^2}}. \tag{3.2.27}$$

The generalized junction acts like an inductor (L_J) connected in parallel with an equivalent resistance R, for small driving ac currents. For larger driving currents, the equivalent Josephson inductance depends on their frequency and magnitude [93].

3.3 SQUID theory

The SQUID is a highly sensitive magnetic flux sensor and detectors based on it can detect various physical quantities, such as voltage, current, magnetic field, etc. It is known for high-sensitivity, low-noise and low power consumption [98].

The operation of a SQUID is governed by two effects, observable only in the superconducting state, namely the Josephson effect and flux quantization. A SQUID consists of a superconducting loop interrupted by one or two Josephson junctions.

A SQUID with one junction is biased with an alternating current in the radio frequency range, and is known as an rf SQUID. A SQUID with two junctions is biased with a direct current and is thus called a dc SQUID. The ultimate sensitivity of an rf SQUID is an order of magnitude smaller than that of a dc SQUID [99]. Only the dc SQUID will be discussed here as it was the intended device to be manufactured. Figure 3.12 illustrates a SQUID with two junctions biased with a direct current.

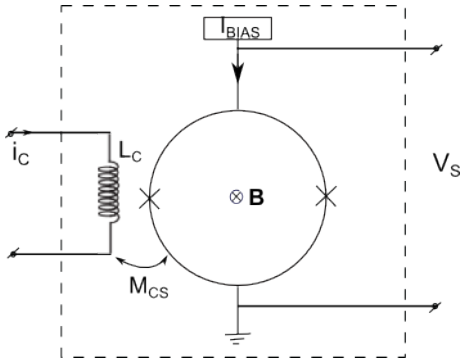

Figure 3.12: A schematic representation of a dc SQUID.

The junctions are indicated by the cross signs on the loop. The current (i_c) through the signal coil (L_c) generates the the flux that is coupled to the SQUID with a mutual inductance M_{CS}. I_{BIAS} is the dc bias of the SQUID and V_S is the SQUID output voltage. $M - CS$ is given by the relation in (5.6.1).

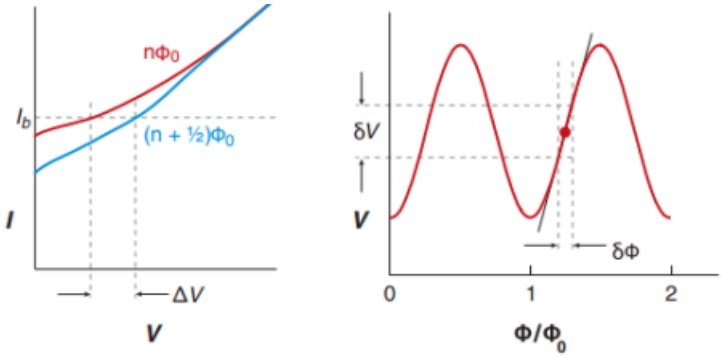

Figure 3.13: I-V characteristic of a SQUID corresponding to applied fluxes of $n\Phi_0$ and $(n + 1/2)\Phi_0$, with n, an integer (left). SQUID voltage V versus applied flux (normalized with the fluxon) for a constant bias current (right). δV is the change in voltage as a result of a small change $\delta\Phi$ in flux [8].

3.3.1 Macroscopic quantum interference

When two identical Josephson junctions are connected in parallel, the phenomenon of macroscopic quantum interference comes into play. This is based on the the gauge

invariant phase difference, given by the expression

$$\phi(y,z,t) = \theta_1(y,z,t) - \theta_2(y,z,t) - \frac{2\pi}{\Phi_0}\int_1^2 \mathbf{A}(\mathbf{r},t)\cdot dl. \tag{3.3.1}$$

Let us consider a superconducting loop interrupted by two Josephson junctions, connected in parallel, as shown in Fig. 3.14.

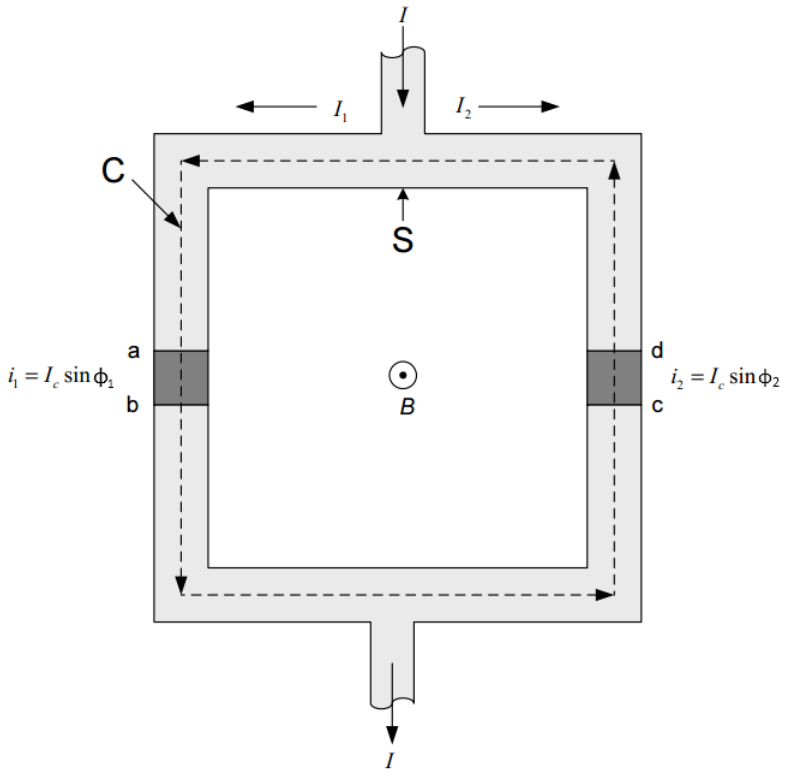

Figure 3.14: Two Josephson junctions connected in parallel in a superconducting loop.

The total current in the loop is given by the current flowing through both branches of the circuit. Assuming basic lumped Josephson junctions, it can be written as

$$I = I_1 + I_2 = I_c \sin\phi_1 + I_c \sin\phi_2 = 2I_c \cos\left(\frac{\phi_1 - \phi_2}{2}\right)\sin\left(\frac{\phi_1 + \phi_2}{2}\right). \tag{3.3.2}$$

The phase difference can be integrated along the closed path as

$$\oint \nabla\theta \cdot dl = 2\pi n = (\theta_b - \theta_a) + (\theta_c - \theta_b) + (\theta_d - \theta_c) + (\theta_a - \theta_d). \tag{3.3.3}$$

By involving (3.1.23), and using (3.3.1) in (3.3.3), the relationship

$$2\pi n = \phi_2 - \phi_1 - \frac{2\pi}{\Phi_0}\oint_C \mathbf{A}\cdot dl - \frac{2\phi}{\Phi_0}\int_{C'} \Lambda\mathbf{J}\cdot dl \tag{3.3.4}$$

is obtained, where C' is the sum of the open paths bc and da. Assuming a wire that is thicker than a few London penetration depths, and the integration path to be deep inside the wire, the term involving $\mathbf{J}$ can be omitted, to give

$$\phi_2 - \phi_1 = 2\pi n + \frac{2\pi\Phi}{\Phi_0}. \tag{3.3.5}$$

The current in the loop is then given by

$$I = 2I_c \cos\left(\frac{\pi\Phi}{\Phi_0}\right) \sin\left(\phi_1 + \frac{\pi\Phi}{\Phi_0}\right), \tag{3.3.6}$$

which resembles the expression for a single junction, with the critical current and phase dependent on the magnetic flux.

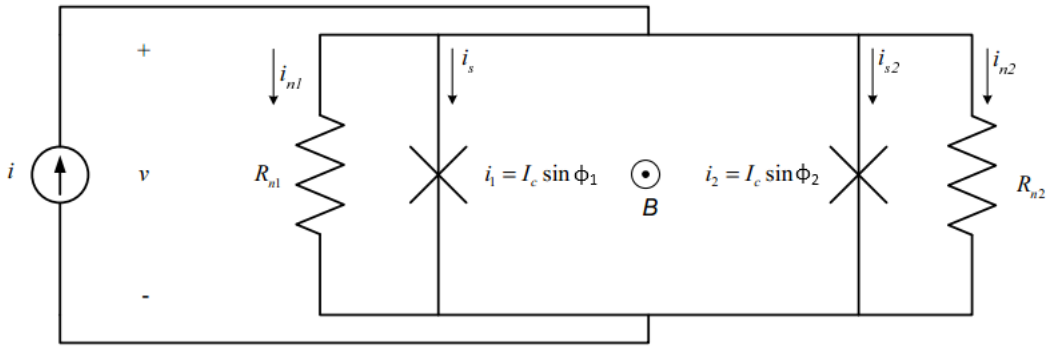

Figure 3.15: Two resistively shunted Josephson junctions connected in parallel in a superconducting loop.

When the inductance of the loop is taken into consideration, the total flux is given by the sum of the applied flux and the flux induced by the circulating current. With $\overline{I} = (I_1 + I_2)/2$ the average current on each side, the currents can be rewritten as:

$$I_1 = \overline{I} + I_{cir} \tag{3.3.7}$$
$$I_2 = \overline{I} - I_{cir}, \tag{3.3.8}$$

and thus the circulating current as

$$I_{cir} = \frac{I_1 - I_2}{2}. \tag{3.3.9}$$

This will induce a flux equal to LI_{cir}, and the total flux can be written as

$$\Phi = \Phi_{ext} + LI_{cir}. \tag{3.3.10}$$

Substitution of (3.3.9) and (3.3.5) into (3.3.10) gives

$$\Phi = \Phi_{ext} - LI_c \sin\left(\frac{\pi\Phi}{\phi_0}\right) \cos\left(\phi_1 + \frac{\pi\Phi}{\Phi_0}\right). \tag{3.3.11}$$

For large loop inductances ($LI_c >> \Phi_{ext}$), the flux generated by the circulating current tend to cancel the applied flux, and the total flux in the loop tend to be quantized [93]. Equation 3.3.9 can thus be rewritten as

$$I_{cir} = \frac{n\Phi_0 - \Phi_{ext}}{L}. \tag{3.3.12}$$

For negligible flux in the SQUID loop ($LI_c << \Phi_{ext}$), the total flux is the externally applied flux Φ_{ext}. An important SQUID parameter is i_{max}, which is a measure of the maximum current that can flow in the SQUID without causing the junctions to be resistive. It is obtained by maximizing (3.3.9) with respect to ϕ_1, and it is given by

$$i_{max} = 2I_c - \frac{2\left|\Phi_{ext} - n\Phi_0\right|}{L}, \tag{3.3.13}$$

for large inductances [91], and by:

$$i_{max} = 2I_c \left|\cos\left(\frac{\pi\Phi_{ext}}{\Phi_0}\right)\right|, \tag{3.3.14}$$

under the assumption that $LI_c << \Phi_{ext}$. In a case where the two junctions have different critical currents the maximum biasing current is given by:

$$i_{max} = \sqrt{I_{c1}^2 + I_{c2}^2 + 2I_{c1}^2 I_{c2}^2 \cos\frac{2\pi\Phi}{\Phi_0}} \tag{3.3.15}$$

Further details can be found in [92], [91].
Another consideration that has been ignored until now is the resistive channels of the junctions, as shown in Figure 3.15. Once taken into account, the current can be expressed as

$$i = I_c \sin\phi_1 + I_c \sin\phi_2 + \frac{v}{R_1} + \frac{v}{R_2}. \tag{3.3.16}$$

In the same way that was used in the previous case, the equation above can be written as

$$i = I_{c_{eff}} \sin\phi + \frac{1}{R}\frac{\Phi_0}{2\pi}\frac{d\phi}{dt}, \tag{3.3.17}$$

where ϕ is a the new phase term given by

$$\phi = \phi_1 + \frac{\pi\Phi_{ext}}{\Phi_0}. \tag{3.3.18}$$

R is the equivalent resistance for both junctions, $I_{c_{eff}} = i_{max}$ is the flux dependent effective critical current of two identical basic junctions connected in parallel and threaded by a flux Φ_{ext}.

With a driving current i higher than the the critical current, a voltage is created across the junctions and the average voltage can be rewritten from (3.2.17) as

$$\langle v(t)\rangle = iR\sqrt{1 - \left(\frac{i_{max}}{i}\right)^2}. \tag{3.3.19}$$

Both $\langle v(t)\rangle$ and i_{max} are periodic in a flux quantum ($\Phi_\circ$) and this feature is exploited in measuring flux. The number of times the dc component of the voltage oscillates is counted as the number of flux quanta applied, for a flux swept from zero. For a constant flux, a flux to null out the applied flux is used [93].

3.3.2 Noise and sensitivity

One of the main things that can impair the performance of a SQUID is noise. Noise in superconductors has many origins, which can be either intrinsic or extrinsic (e.g. the device's electronic environment). In this thesis, only the main types of noise encountered in dc SQUIDs will be looked at, namely white noise and $1/f$ noise.

3.3.2.1 White noise

White noise in dc SQUIDs emanates mainly from the shunt resistance R and is called Nyquist noise. This is explained by random processes like thermal vibrations, or flow of charges at a temperature above 0 K, which result in a noise voltage $V_N(t)$ and a noise current $J_N(t)$ across the device and around the loop respectively. These can also be expressed in terms of their spectral densities S_v (in units of V^2/Hz) or $S_i = S_v/R^2$ (in units of I^2/Hz) [91].

The noise voltage spectral density of a junction is given by

$$S_v(\omega) = \frac{2\hbar\omega R}{e^{\hbar\omega/k_BT} - 1} = 4k_BTR, \tag{3.3.20}$$

where $\omega = 2\pi f$ with f the centre of the bandwidth in Hz, $\hbar = h/2\pi$ is the reduced Planck's constant, T is the absolute temperature and R is the shunt resistance.

The noise voltage of a dc SQUID is expressed as

$$S_v = 16k_BTR, \tag{3.3.21}$$

and the flux noise spectral density, as calculated from S_v/V_Φ^2, for a SQUID with optimal screening parameters is given by

$$S_\Phi = \frac{16k_BTL^2}{R}, \tag{3.3.22}$$

where V_Φ is the voltage-to-flux transfer coefficient. Its minimal value is given by

$$V_\Phi = \frac{\delta V}{\delta\Phi_{ext}} \cong \frac{R}{L} \tag{3.3.23}$$

when the dc SQUID bias current is slightly higher than $2I_c$ [99]. $S_\Phi^{1/2}$ is not frequency dependent, but at a frequency lower that 1Hz, it scales as $1/f$. The approximations given by (3.3.21) and (3.3.22), for white noise region, are widely used for dc SQUIDs with $\beta_l \simeq 1$ (see 4.1), $\beta_c < 1$, and $\Gamma \ll 1$ [100] .

Another important quantity that is derived from the relations above is the energy resolution [101], which is useful in checking the relative performance of SQUIDs. It is approximated as

$$\epsilon = \frac{S_\Phi}{2L} \approx 9k_BT\frac{L}{R}. \tag{3.3.24}$$

3.3.2.2 Low-frequency noise

For applications that require high resolution at low frequencies (about 1Hz and less), SQUIDs are impaired by flicker noise, which is abundant at such frequencies. Flicker noise scales as $1/f$ and it originates mainly, on the one hand, from hopping of the flux vortices between pinning sites in the SQUID body due to temperature, and on the other hand, from the fluctuation in the critical current due to electrons stuck on defects during tunnelling.

Critical current noise can be reduced by the electronics, but noise generated by flux vortices cannot, because it is very dependent on the properties of the superconductor [99], [91].

3.3.2.3 Sensitivity

The inductance of a SQUID can be estimated from the magnetic energy stored in the loop (W_s) and the thermal energy (ϵ_T). For the thermal noise not to have a negative effect on the performance of the device, one needs to have $W_s > \epsilon_T$. This is equivalent to

$$1/2\Phi_0^2/L > 1/2k_BT \Leftrightarrow L < \frac{\Phi_0^2}{k_BT}. \tag{3.3.25}$$

The relation above shows that the inductance will depend on the temperature, and typical values of L are such that $L < 10^{-10}$H at 100K and $L < 10^{-9}$H at 4K. Conversely, one should note that at a fixed inductance, the lower the temperature the lower the thermal energy [93].

The sensitivity of a SQUID firstly depends on its inductance L. Upon application of an external flux, the variation of i_{max} between its boundaries (i_{max}^+ and i_{max}^-) corresponds to a change of half a fluxon, which is equivalent to half a period in the averaged voltage $\langle v \rangle$. For $LI_c > \Phi_0$, we have that

$$i_{max}^+ - i_{max}^- \approx \frac{\Phi_0}{L}. \tag{3.3.26}$$

The sensitivity of the voltage to the applied flux is derived as

$$\frac{\delta\langle v \rangle}{\delta\Phi_{ext}} = \frac{R(i_{max}^+ - i_{max}^-)}{\Phi_0/2} = 2R/L. \tag{3.3.27}$$

If the junction resistance R is taken as 1Ω, with an inductance of about 1nH, the typical sensitivity of a dc SQUID is found to be a microvolt per fluxon.

For better measurement of very small magnetic fields using dc SQUIDs as magnetometers, one would need to have a SQUID loop that is as large as possible, such that a small change of the applied magnetic field (δB) will result in the largest possible flux change $\delta\phi = A.\delta B$. This will result in a large SQUID inductance, which is contrary to optimal parameter requirements.

An alternative way to achieve that is to make the SQUID area A as large as possible, while keeping the SQUID loop small. This is applied in structures known as large area SQUIDs or washer SQUIDs, also known as "Ketchen SQUIDs".

3.4 Josephson junction simulations

The simulation results reported below were achieved using the analogue behavioural modelling facility of the NGSpice circuit simulator, together with Matlab software for ease of labelling and plotting the results. The script is provided in Appendix C. The Josephson junction circuit behaviour under different circumstances (bias type, value of the Stewart-McCumber parameter, etc.) has been simulated. The current-voltage (I-V) relationships are shown in graphs. The NGSpice circuit model of a Josephson junction is given in Fig. 3.16.

Three junctions have been simulated, with $\beta_c << 1$, $\beta_c \simeq 1$, and $\beta_c >> 1$.

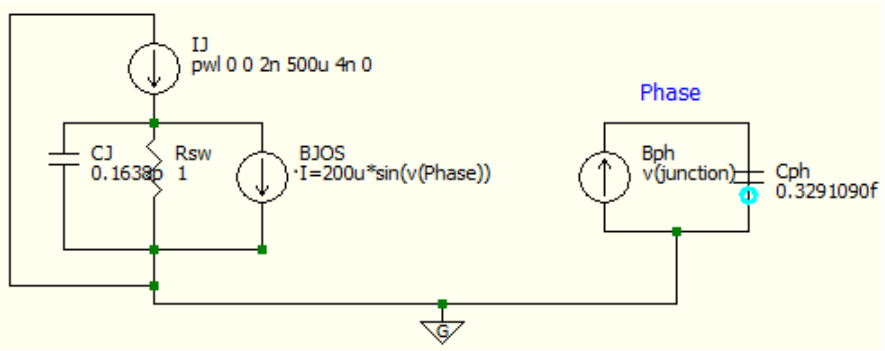

Figure 3.16: Spice equivalent circuit of a Josephson junction.

The simulations of Josephson junctions are based on two relations, the current-phase relationship (3.2.10) and the voltage-phase relationship (3.2.5). These equations can be rewritten, for clarity, as

$$i = I_c \sin(\phi) + \frac{V}{R} + i_C \tag{3.4.1}$$

and

$$V = \frac{d\phi}{dt}\frac{\Phi_0}{2\pi}, \tag{3.4.2}$$

where the subscript C refers to the capacitive channel. Hence,

$$i_C = C\frac{dV}{dt}. \tag{3.4.3}$$

The resistance was taken as unity for simplicity, the capacitance of the junction was calculated according to the desired value of β_c. In order to implement the junction phase, an analogy between (3.4.2) and (3.4.3) was used, allowing also to define a non-linear dependent source Bph as in Fig. 3.16.

The junction was simulated for a critical current of $I_c = 200\mu$A, the shunt resistance of $R = 1\Omega$, the input current is $2.5I_c$ and a switch model is used to implement the junction resistance, with a threshold voltage of 2.6mV. The junction was implemented as a subcircuit and used in the SQUID simulations reported in Section 3.5.

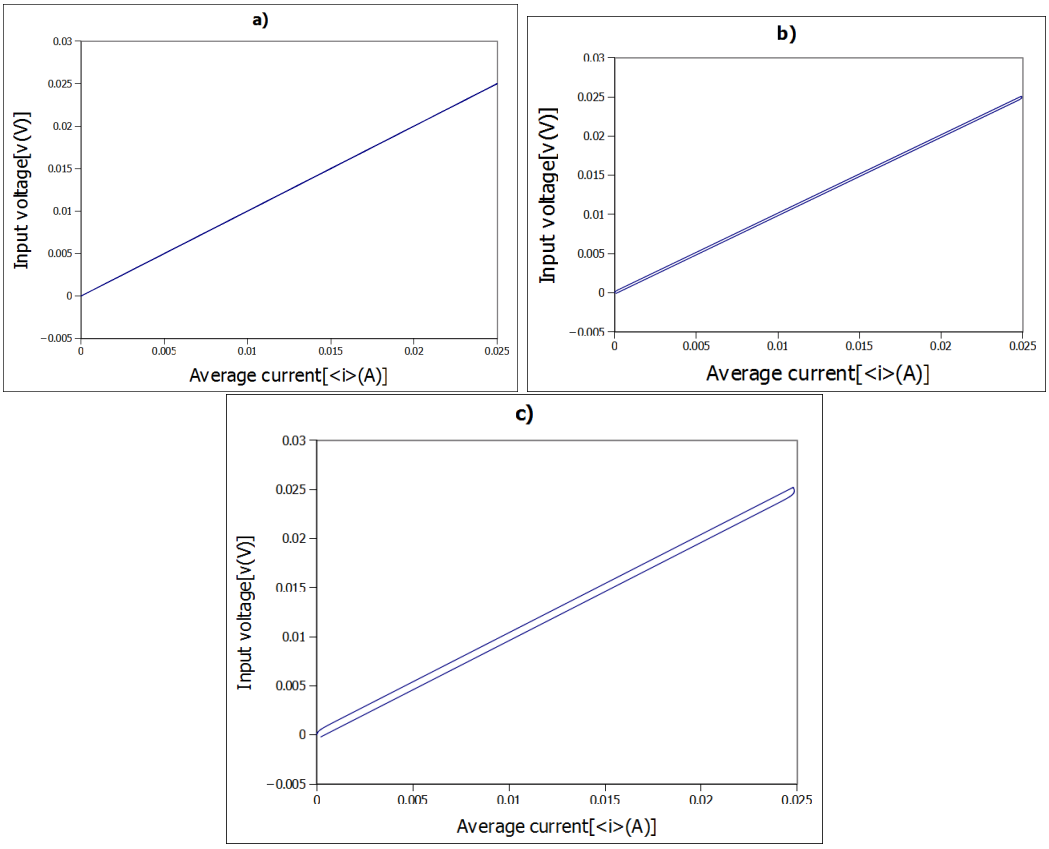

Figure 3.17: The average current $< i >$ versus voltage V curve for a junction driven by a dc voltage source for a) $\beta_c << 1$ (=0.1), b) $\beta_c = 1$ and c) $\beta_c >> 1$ (=10).

The time averaged current for a dc voltage driven junction is equivalent to the voltage divided by the resistance of the junction. With $\beta_c = 0.1, \beta_c = 1$ and $\beta_c = 10$, as the applied voltage is increased from $V = 0$ and decreased form $V > 0$, the curve follows the same path up and down. The characteristic is a straight line and non-hysteretic, as shown in Fig. 3.17.

Figure 3.18 shows the time averaged voltage $< v(t) >$ versus the current I. When $\beta_c = 0.1$, as the driving current is increased from $I = 0$ and decreased from $I > I_c$, both characteristics are the same. The curve follows the same path up and down. For values of $\beta_c \simeq 1$ and $\beta_c >> 1$ the V-I characteristics are hysteretic.

For large capacitance values ($\beta_c >> 1$ i.e. $\tau_{RC} >> \tau_j$), the time it takes for the phase (ϕ) to change, is nearly instantaneous compared to the time for the charge to relax from the capacitor. The average voltage across such a dc current driven junction is $< v(t) >= iR$. For a current decreasing from $i > I_c$, the I-V characteristic is thus a straight line whose slope is the conductance of the junction.

The response of a Josephson junction to an AC current source was simulated in accordance to the circuit displayed in Fig. 3.10. The relation in (3.2.25) was used

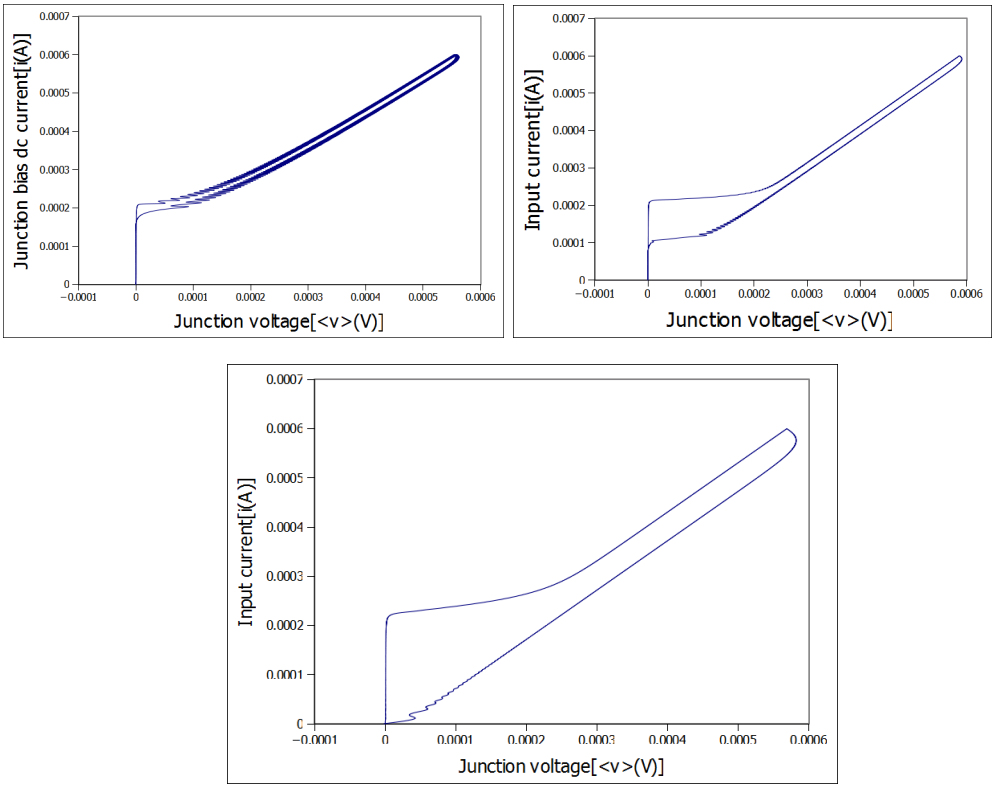

Figure 3.18: The $< v >$ versus I curve when the input to the junction is given by a constant current I_o for a) $\beta_c << 1$ (=0.1), b) $\beta_c \simeq 1$ (=4) and c) $\beta_c >> 1$ (=20).

to define an oscillating current source with a frequency of 2GHz, $I_0 = 2$mA, and the junction has $I_c = 100\mu$A and $\beta_c = 0.1$.

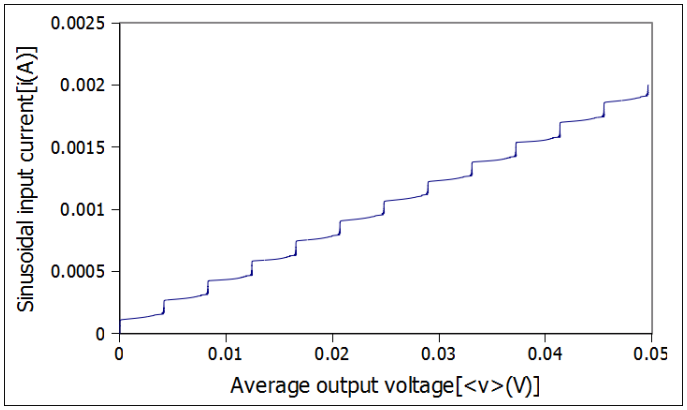

Figure 3.19: The $< v >$ versus I curve when the input to the junction is an oscillating current of the form $I_o + I_s \sin(\omega t)$, with $\beta_c << 1$. The frequency of the oscillating source is 2GHz and the amplitude is 60μA.

We expect the average dc voltage to remain zero as the dc component of the driving

current I_0 is increased from zero. As the current I_0 exceeds the height of the current spike at zero voltage, the voltage increases with the slope of the resistance until the voltage reaches the next spike. At this point the current sharply increases, while the voltage remains relatively fixed. As the current increases, the voltage will continue this pattern and trace out the staircase shown in the graph in Fig. 3.19. The rises in the voltage will occur precisely in voltage steps given by $V_0 = n(\Phi_0/2\pi)\omega_s$.

3.5 Dc SQUID simulations

The simulations of the dc SQUID involve the Josephson junctions as its main component. The junction, that was modelled earlier (see section 3.4), is included as a subcircuit in the SQUID simulation. The applied flux is implemented by coupling an external coil to the SQUID loop. The coupling factor is taken as one, and the mutual inductance, given by (5.6.1), is considered in the expression of the flux.

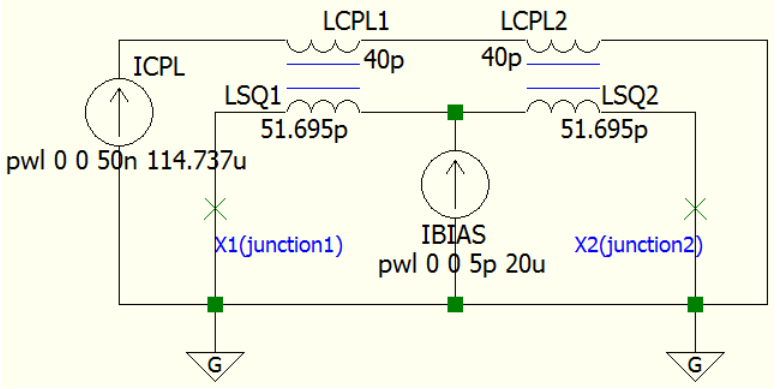

Figure 3.20: Equivalent circuit of a dc SQUID as simulated in NGSpice.

Figure 3.20 shows the NGSpice circuit used to simulate the dc SQUID in this work. The external coil is divided into two equivalent inductors each of which is coupled to one of the SQUID loop's, also represented by two equivalent inductors. The coupling constant in (5.6.1) is chosen to be k = 1. The SQUID inductance, calculated from (4.1.2) for the optimum value of the screening parameter ($\beta_l = 1$) and $I_c = 10\mu A$ is $L = 103.4pH$, and the coil has inductance $L_C = 80pH$. The McCumber parameter was chosen to be $\beta_c = 0.1$, and the SQUID was biased at just above its critical current ($I_{BIAS} \geq 2I_c$).

The obtained I-V curves oscillate between values of current corresponding to an applied flux equal to integer multiples of half a fluxon and a full fluxon. The simulation of the I-V characteristics were particularly done with a critical current of $2Ic = 400\mu$A. Recall that, in this thesis, I_c has been referred to as the critical current of a single Josephson junction.

The flux-to-voltage conversion by the SQUID is shown in Fig. 3.23. The voltage versus flux curve is oscillating almost sinusoidally as the applied flux is swept up to

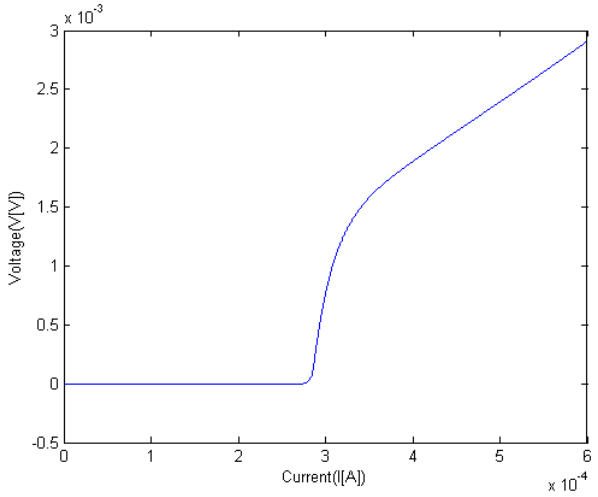

Figure 3.21: Current-voltage characteristic for applied flux values of $(n + 1/2)\Phi_0$, where n is an integer.

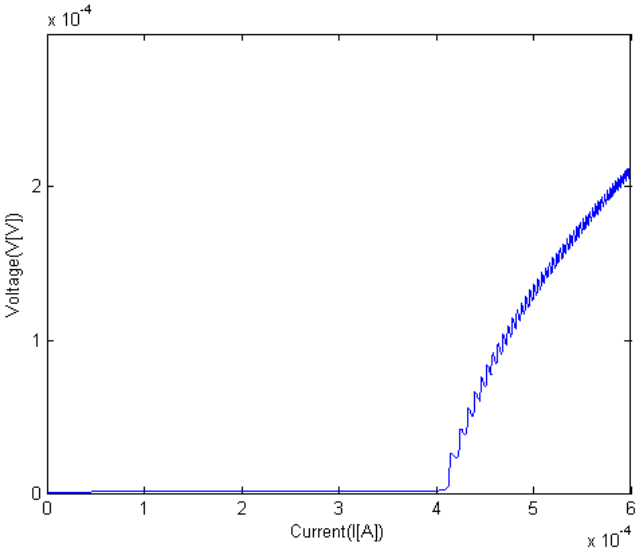

Figure 3.22: Current-voltage characteristic for applied flux values of $n\Phi_0$, where n is an integer.

five flux quanta. The output voltage of the dc SQUID is periodic in the applied flux, and has a period of one fluxon.

In Fig. 3.24 the circulating current in the SQUID loop is plotted in terms of the applied flux. The curve is periodic in the flux quantum.

The current circulating in the SQUID loop was simulated from (3.3.9) and the included flux is given by (3.3.10).

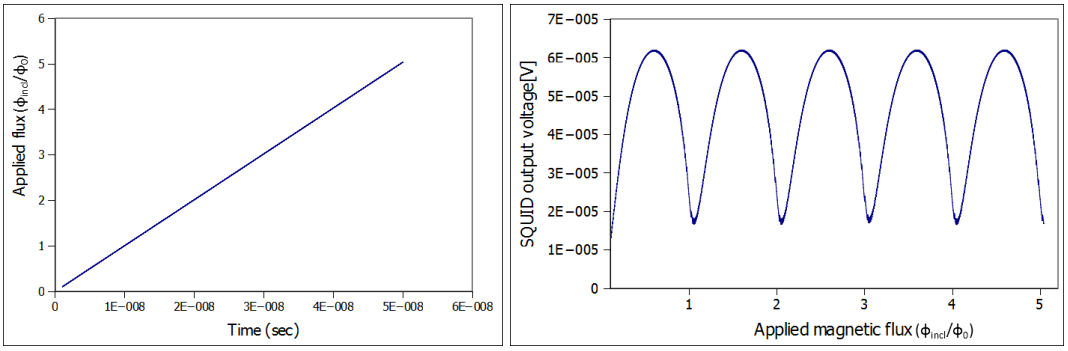

Figure 3.23: Voltage versus flux characteristic for a dc SQUID. The flux is normalized with the flux quantum.

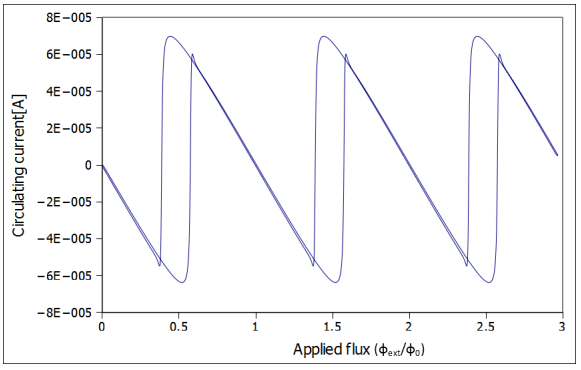

Figure 3.24: Circulating current versus SQUID flux.

Figure 3.25 shows the total flux included in the SQUID loop plotted against the applied flux; the curve is periodic in a flux quantum.

3.6 Flux locked loop simulations

In practice SQUIDs are normally operated in a flux locked loop (FLL) configuration, in order to linearise the periodic output signal when excited by a linear ramp flux input. The output signal is fed back to the SQUID loop to cancel the applied flux and is thus a true representation of the input flux. The flux locked loop simulated here had the same parameters as the one previously designed in [91]. The SQUID is biased at its operating point ($3.4I_c$), the preamplifier gain was chosen to be 450, the components of the integrator are such that the resistance $R_{int} = 100\Omega$, the capacitance $C_{int} = 20$pF, and the gain is 10^{40}. The feedback resistance and inductance are $R_{fb} = 294.47$ kΩ and $L_{fb} = 36\mu$H respectively.

Figure 3.26 shows the output voltage of the FLL plotted as a function of time (left) and the output voltage of the FLL plotted as a function of the applied flux (right).

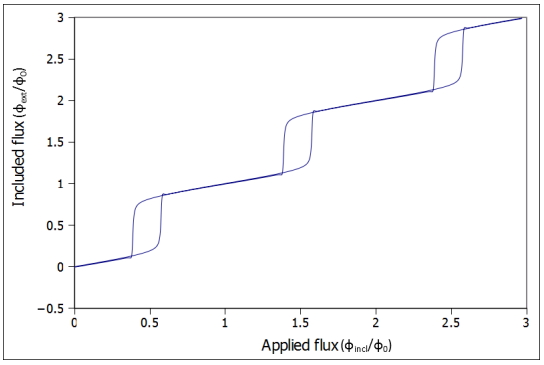

Figure 3.25: Included flux of the SQUID versus applied flux. The curve is hysteretic.

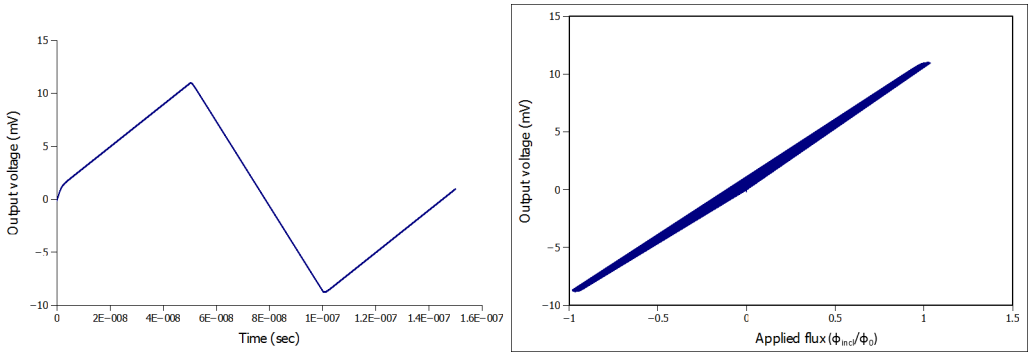

Figure 3.26: The flux locked loop simulated with NGSpice, with the applied flux linearly swept from 0 to Φ_0, then down to $-\Phi_0$, and back up to 0.

As can clearly be observed, the transfer relationship is linear.

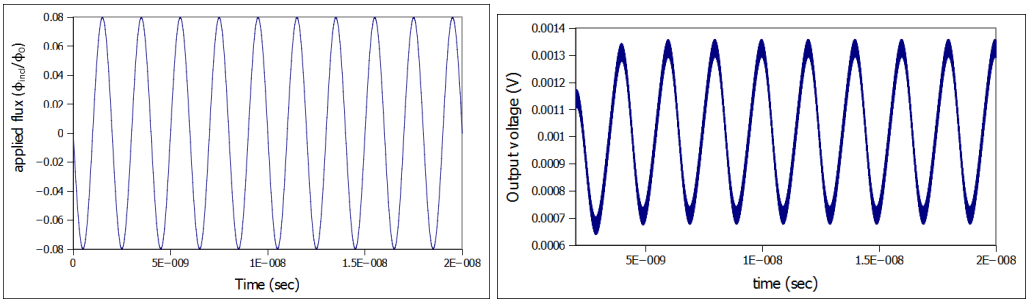

Figure 3.27: Flux locked loop simulations with a small input signal at 500 MHz. The applied flux (left) and the output voltage (right) are plotted against time.

Figures 3.27 and 3.28 show the results of simulations of a FLL when the SQUID is threaded by a small signal at 500 MHz and 50 MHz respectively. The voltage at the output of the FLL has a period of 2ns for the 500MHz input signal and a period of 20ns for the 500MHz input signal. In both cases, the applied flux, normalized with

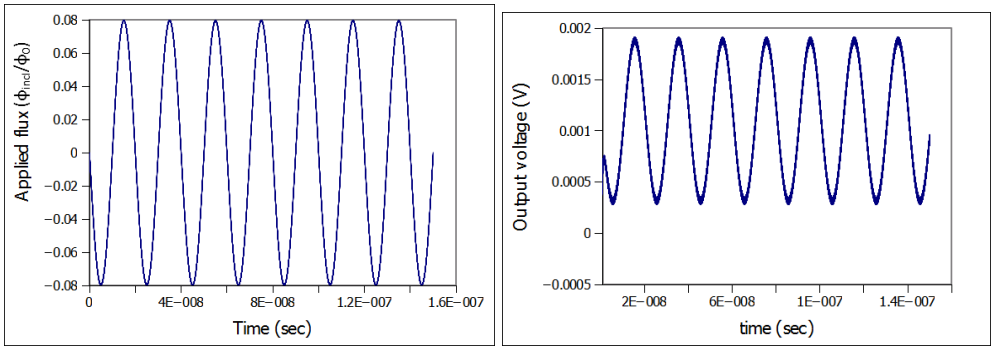

Figure 3.28: NGSpice small signal ($\Phi_0/4\pi$) simulations of a flux locked loop at 50 MHz. The figures show the applied flux (left) and the output voltage (right) versus time.

the flux quantum is plotted on the left hand side, and the output voltage at the right.

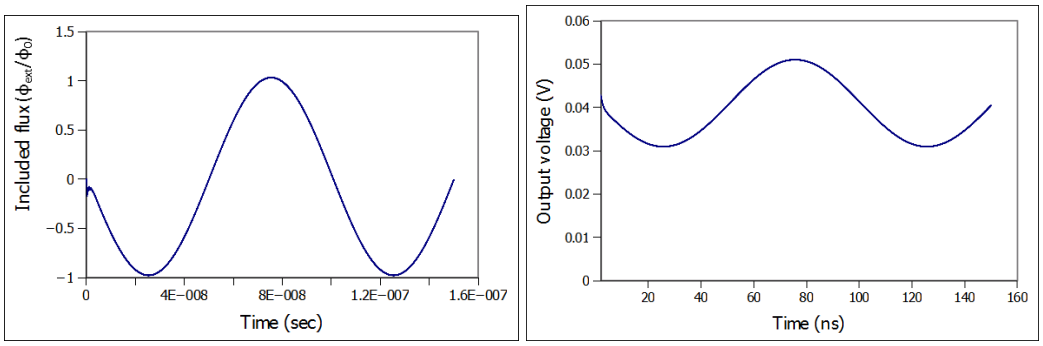

Figure 3.29: Flux locked loop simulations of a sinusoidal input signal with a single fluxon amplitude at 10 MHz. The figures show the included flux in the SQUID loop (left) and the voltage at the output of the flux locked loop (right), both as function of time.

In Fig. 3.29 the flux included in the SQUID loop and the FLL output voltage are both plotted against time. The input signal has a single fluxon amplitude and a frequency of 10MHz. The output voltage has period 75ns.

3.7 Summary

A brief theoretical background of superconductivity, the Josephson junction and the SQUID was given in this chapter. The models that explain the foundations of superconductivity, the dynamics of the Josephson junction, and the theory and applicability of a SQUID magnetometer were reviewed. The simulations of the Josephson junction and the SQUID dynamics were done by using the analogue behavioural facility of the NGSpice circuit simulator. The Spice circuit models representing both devices are presented, and the results of the simulations were presented in respective figures. The results of the simulations corresponded well with the theoretical principles given in Section 3.3, and will be used as reference to verify the results of the

manufactured devices in Section 4.2. The Spice model of a dc SQUID established in this chapter is a useful tool that can be used to extensively investigate and predict the flexibility of the dynamics of a dc SQUID. This is important and enables one to understand the results of testing such a device. In the next chapter a dc SQUID will be designed and manufactured, and the test results will be presented.

Chapter 4

Design, Fabrication and Testing of a DC SQUID

A dc SQUID utilises Josephson junctions a building blocks. The design and fabrication are determined in conjunction with the choice of the type of junctions to be used. In this work, micro-constriction junctions were used and implemented, using both AFM nano-ploughing and laser lithography. This choice of junction was favoured by the fact that it was an extension of the latest work [102] in our group and the availability of early training provision. Further matters of interest will be discussed in Section 4.1.1. An overview of the procedure which was followed to fabricate a working SQUID, and all the methods used from design to fabrication and testing, are given in this chapter.

4.1 Design of the DC SQUID

When designing a SQUID it is important to consider a number of points. The energy resolution is of key importance when it comes to magnetometer and gradiometer applications, and it is given by

$$\epsilon = \phi_n^2/2Lk^2, \tag{4.1.1}$$

with ϕ_n the rms flux noise, and k the coupling constant between the input coil and the SQUID loop [103]. Equation (4.1.1) suggests that, for a better energy resolution, one needs a small SQUID inductance L.

Another aspect to consider is the screening parameter

$$\beta_l = 2I_cL/\Phi_0, \tag{4.1.2}$$

which is optimum when $\beta_l = 1$. In this case the optimal energy resolution, when the RSJ model is used, is given by

$$\epsilon = 9k_BTL/R.$$

In the case of the RCSJ model, where real junctions have non-zero capacitance, the optimal condition for junctions is to be overdamped (non-hysteretic). The Stewart-

McCumber parameter, which is given by

$$\beta_c = 2\pi I_c R^2 C/\Phi_0, \tag{4.1.3}$$

needs to be such that $\beta_c \simeq 1$, as argued by Tesche and Clarke [103]. The energy resolution then becomes

$$\epsilon = 16 k_B T \sqrt{LC}/k^2. \tag{4.1.4}$$

Briefly, for a SQUID to have a small energy resolution, a small SQUID inductance and/or junction capacitance is required. The SQUID loop inductance can be made small by geometric dimensions, but a small L makes it difficult to couple the flux, thus reducing the sensitivity of the SQUID [104]. The effective area of the SQUID can be increased for compensation and, even better, a pickup loop can be used for easy coupling of the external flux.

There must be a lower limit on C, which is determined by the fabrication limitations or capabilities [101]. However, C is not a big issue in micro-bridges, as the capacitance is already known to be low enough.

Another consideration when dealing with the performance of a SQUID is the noise. The noise that affects the performance of dc SQUIDs can be characterized by the noise parameter

$$\Gamma = 2\pi k_B T/I_c \Phi_0. \tag{4.1.5}$$

By constricting the flux energy per flux quantum ($\frac{\Phi_0}{2L}$) to be smaller than the thermal energy,

$$\frac{\Phi_0}{2L} \geq 2\pi k_B T/I_c \Phi_0, \tag{4.1.6}$$

the negative effect due to the noise is minimized.

The SQUID inductance should then be such that $L < 320$pH. Typical values for high performance HTS SQUIDs range from 50pH$< L <$ 100pH [105].

As seen in Section 3.3.2.3, a SQUID of large area is preferred for enhanced sensitivity. For this reason a chrome mask of a washer SQUID (large area SQUID) was used to define a SQUID structure by means of UV-lithography (Section 4.2.3). This mask already existed at Stellenbosch University, and was made according to a previous design by Graser [97], where the designed washer SQUID had an inductance of 49.78pH. Another SQUID, with a simplified geometry for ease of the fabrication, was designed to have an inductance of 39.92pH. The implementation of Josephson junctions was done by means of AFM nano-ploughing [102].

The AFM nano-ploughing was not easily repeatable, so that a new method had to be adopted. Taking advantage of the new in-house developed laser lithography system, a new SQUID design was made and used for the "new" double resist laser lithography technique (Section 4.1.2) for implementing the micro-bridge Josephson junctions.

A G-code script to define the new design (see Appendix B) was written by using the EMC2 or NCplot program The code was then transferred to the EMC2 application, which was configured to run the laser lithography system in a Linux environment. The dimensions of the new design was made to be smaller or comparable to the ones used previously [97]. A mask for the deposition of the pads in the thermal evaporator was implemented using the Inkscape software drawing tool. The new designs used for the laser lithography and pad deposition mask are given in Appendix B.

4.1.1 Choice of Josephson junction type

The ultimate choice of a planar micro/nano-bridge (also called a Dayem-bridge) structure for a Josephson junction lies in the fact that most weak links have a considerably lower junction capacitance ($\beta_c << 1$) relative to tunnel junctions [106]. This is an advantage in the structuring of junctions for the fabrication of an optimal SQUID (Section 4.1).

The creation of a micro-bridge consists of leaving only a narrow region in a certain section of a superconducting track. While some weak links work by proximity effect (the ability of a superconducting condensate of Cooper pairs to conserve the amplitude and phase of its order parameter at distances of the order of the coherence length [96]), the micro-bridges behave like Josephson junctions, because the critical current in the constriction is much smaller than it is in the rest of the track. The reduced critical current in the narrow region causes the superconductor in the constriction to switch to the normal resistive state [96].

Anderson and Dayem [107] have shown in their theory that, if the dimensions of the micro-bridge are less than or equal to the coherence length ξ(T), it will display the Josephson effect! Nevertheless, even in wide bridges where the effective length/width ($L_{eff} \approx$ max(L,W)) is larger than the coherence length, due to the periodic motion of quantum vortices at the narrowest point of the bridge, this characteristic will still be displayed [108] (See Fig. 4.1).

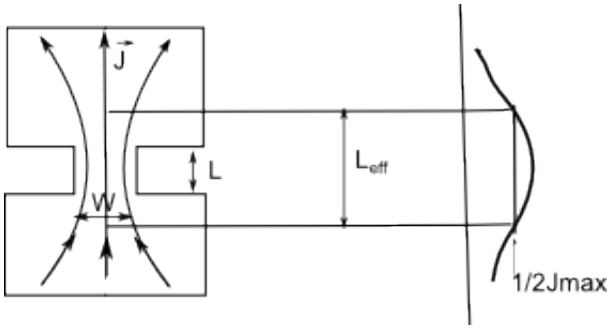

Figure 4.1: A schematic representation of a Dayem-bridge with its dimensional parameters (adapted from)[106].

4.1.2 Maskless SQUID design for laser lithography

The EMC2 application of Ubuntu LinuxCNC 10.4 is used to control machines and write scripts in the G-code format. This tool was used to write the code (See Appendix B) of the SQUID design and to operate the laser lithography system used in this project.

It has been reported that the closeness of the junctions' homology contributes to a well suited SQUID for its application [98]. It is thus important to preserve the symmetry of the critical currents. The new design aimed at keeping the geometric shape and dimensions of the constrictions, on an individual dc SQUID, as close to each other as possible.

The new design was made by accommodating the dimensions of the previous design by Graser, where two proposed shapes were intended for intrinsic Josephson junctions. The new shape was chosen as suitable to allow a loop that is small enough to allow for the superposition of structures during the laser lithography process. The EMC2 application gives a flexibility in making and modifying such structures, and can be used for a lot more than just SQUID design.

Two structures were designed, a small structure as an implementation of the constrictions, and a larger structure of the extended circuit, comprising the flux coupling loop to the SQUID and the contact pads, to connect with the outside circuitry. The designs are shown in Fig. B.1, and the real structures after lithography in Fig. 4.16.

4.2 Fabrication of a dc SQUID

SQUIDS are fabricated on superconducting thin films patterned by photolithography. In this project HTS $Y_1Ba_2Cu_3O_{7-\delta}$ thin films, deposited on MgO wafers, have been used. The preference for $Y_1Ba_2Cu_3O_{7-\delta}$ in superconductors lies in the fact that it has a high T_c, and thus requires a relatively cheaper cryogenic environment (liquid nitrogen). It also offers the possibility of manufacturing devices on single layered thin films, which is much easier than constructing multilayered devices.

The fabrication process consists of a number of steps as explained in this section.

4.2.1 Thin film deposition

Superconductors are made either as thin films or in bulk form. Superconducting thin films are commonly used to fabricate superconducting electronic circuits. Various techniques are used for thin film deposition.

Some of these methods are pulsed laser deposition (PLD), epitaxial growth, plasma and thermal chemical vapor deposition (CVD), rf and dc magnetron sputtering, etc.

These depositions can either be in situ or ex situ, depending on whether, after deposition, the film is superconducting or has to undergo another process. Further

details on deposition techniques can be found in [102].

Some of the most stringent prerequisites for the successful deposition of high-temperature superconductor (HTS) thin films of high quality are the stoichiometry (relative proportions of elements involved) control of metallic constituents and the correct oxygenation. The YBCO ($Y_1Ba_2Cu_3O_{7-\delta}$) used in this project has stoichiometry 1-2-3, and this needs to be conformed to, together with epitaxy[1], for the film to be superconducting.

A good choice of substrate is also important in making films suitable for SQUID fabrication. A good substrate should have good adhesion of the film, but not react chemically with the film. A good thermal expansion match, cleanliness[2] and uniformity of the surface are thus necessary. For epitaxial $Y_1Ba_2Cu_3O_{7-\delta}$ a singly oriented film is required. For film and substrate matching aspects such as crystallographic orientations, atomic positions and lattice parameters have to be taken into account [97]. A lattice mismatch of less than 15% is acceptable. Most HTS suitable substrate have a perovskite structure. MgO, that was mainly used in this project, has a rather NaCl-like structure. Though not a perovskite, it can still give high quality $Y_1Ba_2Cu_3O_{7-\delta}$ thin films, with a lattice mismatch of 9%, a dielectric constant of ϵ=9.65, and $\tan\delta = 5.10^{-4}$. $SrTiO_3$, that was alternatively used, has a perovskite structure with a lattice mismatch of 2%, $\tan\delta = 6.10^{-2}$, and a dielectric constant ϵ= 277. MgO was mainly used as it was available in the beginning. It is also cheap and quickly obtainable. More details about HTS substrate properties can be found in [102] and [97].

In this thesis, the deposition of $Y_1Ba_2Cu_3O_{7-\delta}$ thin films was done by using Inverted Cylindrical Magnetron (ICM) sputtering and Pulsed Laser Deposition (PLD), both available at Stellenbosch University. Samples with thicknesses of 150 nm to 250 nm were obtained, and the parameters of deposition are given in Table 4.1 and 4.2.

4.2.1.1 DC Magnetron sputtering

During dc magnetron sputtering a conducting target (source of material to be grown) is eroded by ions that are more energetic than the target atoms' binding energy. The ions are created as a plasma, by field emission of electrons from the cathode, in an inert gas (argon), and accelerated towards the target by a negative dc voltage. The target atoms are dislodged, and after undergoing multiple collisions with the plasma species, are deposited on a substrate to grow a film.

A radio frequency voltage can be used for non-conducting targets and this method is known as rf sputtering.

The formation of anions at the cathode (target side) leads to the problem of re-

[1] A process of deposition of a thin coat of monocrystalline material on a monocrystalline substrate. During epitaxy, the crystal lattice of the substrate is reproduced in the grown film.

[2] Cleaning the substrate consists of degreasing it in an organic solvent, and annealing (in oxygen for oxide substrates).

sputtering (which creates ripples, cones or pits on the growing film) or, in extreme cases, etching of the substrate instead of deposition [109]. The use of a cylindrical target to place the substrate off-axis is one of the solutions to the resputtering problem [102], [109]. Such a configuration is known as an Inverted Cylindrical Magnetron (ICM).

The ICM sputter deposition of YBCO thin films was used in this project and a number of critical parameters, which play an important role in determining whether the film will be superconducting or not, must be taken into consideration, such as the substrate-to-target distance, gas mixture ratio (Ar:O_2) and total pressure, the base vacuum attained before gas mixing, the substrate temperature, the power and cathode voltage.

The substrate-to-target distance determines the correct focus of particles projected from the target, determines the energy of the atoms reaching the substrate and influences the deposition rate. The oxygen environment and correct pressure during deposition play an important role in the stoichiometry of the layer. Zhai et al. [110] showed that, without oxygen during deposition, the film would have semiconducting behaviour, even though fully oxygen annealed. They also concluded that 97% of the stoichiometric oxygen is absorbed during deposition.

The substrate temperature has a big impact on the transition temperature and the sharpness of the transition. Viable deposition temperatures of YBCO films range from 680°C to 820°C, with different yields on the film properties. Habermeier et al. [109], studying the dependence of the transition characteristics (onset, midpoint and zero resistance temperature) to the deposition temperature, in the same range as mentioned above, showed that the highest T_c and transition sharpness were obtained at a deposition temperature of 750^{o}C.

The higher the vacuum attained before deposition, the better the evacuation of the deposition chamber, which minimizes the risk of possible contamination of the sample.

ICM deposition, as done in this thesis, was performed as follows:

> The MgO substrate was glued onto the substrate holder (mounted on a heater) by an even silver coating. Evacuation of the deposition chamber was done by creating a vacuum of 7μHg, using a roughing pump, after which Ar and O_2 were added, up to a pressure of 220μHg, in a 1:1 ratio. The substrate was heated to 750°C after which the plasma was ignited to start the deposition, which lasted for about an hour. Annealing at 490°C was performed afterwards in an oxygen atmosphere at atmospheric pressure. The oxygen annealing after deposition is important for structure reformation, as it leads to the superconducting orthorhombic structure [110].

Parameter	value
Deposition temperature	740°C
Gas ratio	1:1
Deposition gas pressure	220μHg
Annealing temperature	490°C
Current	400mA
Power	72W
Voltage	170V
Base Pressure (vacuum)	$8 \times 10^{-1}\mu$Hg

Table 4.1: Deposition parameters for ICM sputtering

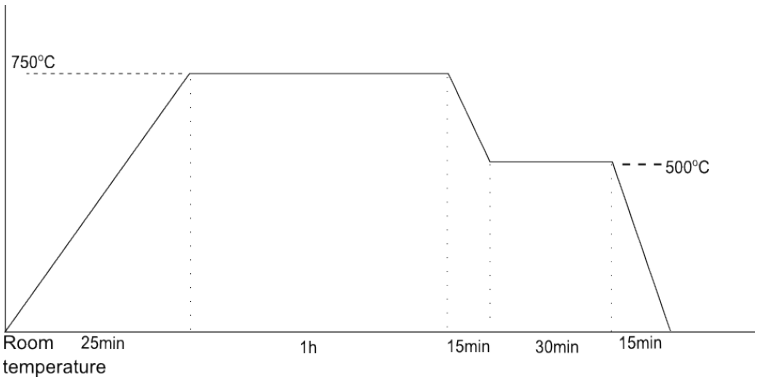

Figure 4.2: Sputtering deposition temperature profile

4.2.1.2 Pulsed Laser Deposition

The pulsed laser deposition (PLD) technique is one of the most successful physical vapor deposition methods. It is also commonly used for epitaxial growth of high-T_c superconductors. PLD works on the principle of pulsed laser ablation of the target, which results in a production of a plume comprising clusters, ions, atoms and oxide molecules. When a laser of high intensity is used, the evaporation process is above thermal equilibrium, and a plasma is generated at the target surface. A direct jet-like plasma stream follows and the plume deposits directly onto the substrate, which is placed in front of the target, preferably at the tip of the plume. The laser is focused onto the substrate at an angle that allows a forward direct jet-like ejection of the plume. This ensures the ability to precisely reproduce the target composition in the film. PLD does, however, have a few drawbacks, such as a large amount of particulates on the films. A typical example (AFM picture) is shown in Fig. 4.9.

An oxygen environment is always required for YBCO deposition, in order to complete the stoichiometry.

A PLD process takes a number of parameters into account and these need to be optimized for an optimal deposition process. These parameters are the oxygen background pressure, the substrate temperature, the target-to-substrate distance, the

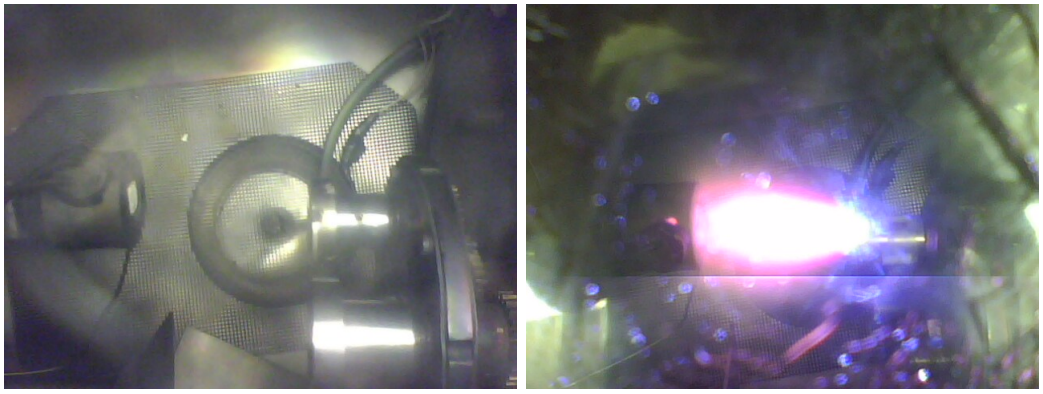

Figure 4.3: PLD interior at rest (left) and in action (right) showing plume projection focused on the sample

laser spot size on the target, the laser wavelength, the pulse duration and pulse energy density at the target site. More information on each parameter of the properties of the film can be found in [97] and [111]. The parameters used in this project are summarised in Table 4.2.

Parameter	Value
Deposition temperature	750°C
Oxygen pressure	8x10^{-2} mbar
Annealing temperature	500°C
Deposition laser frequency	10 Hz
Deposition laser energy	180 mJ
Laser spot size	2.5±0.5 mm
Base pressure (vacuum)	1×10^{-4} mbar
Target-to-substrate distance	6.5 cm

Table 4.2: Deposition parameters for PLD

In this project the PLD deposition process was performed as follows:

> The sample was mounted on the sample holder (on top of the heater), by application of an even coat of silver. A high vacuum (10^{-4} mbar) was created by means of a roughing pump and two turbo molecular vacuum pumps to ensure optimal evacuation of the deposition chamber. The chamber was brought up to an oxygen pressure of 8×10^{-2} mbar to serve as a reactive medium for the plume. The substrate was then heated up to the deposition temperature, and then the deposition stage was initiated. When the deposition period came to an end, the laser was switched off and the sample was cooled down to the annealing temperature (500°C). During cooling the oxygen pressure was increased to reach atmospheric pressure, and kept there for the duration of the annealing period. After annealing the sample was cooled down to room temperature, and taken out of the chamber. The deposition profile is given in Fig. 4.4.

It is always necessary to check that the laser is well focused onto the target and that the energy is directed to the target surface. This will ensure that the target rotator is working properly and that the sample is well placed at the plume tip.

The target used to be rotated during the deposition process, causing it to be eroded by the laser in concentric circles. This required sanding of the target surface before use. An improvement on the target rotator has now been made, which cancels out the need for sanding of the target. A second rotator motor has been incorporated, and is used to move the target up and down in short arcs, resulting in the target being evenly covered by the laser.

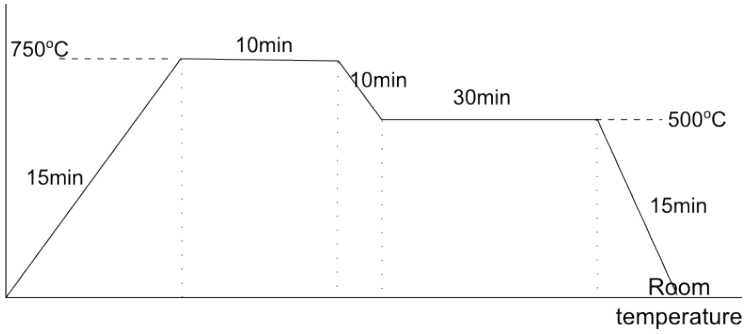

Figure 4.4: PLD deposition temperature profile

4.2.2 Characterization of the $Y_1Ba_2Cu_3O_{7-\delta}$ surface deposited on an MgO substrate by using the sputter deposition technique

The YBCO thin films used to fabricate the dc SQUIDs are required to meet certain quality standards to ensure that the devices made from them will have suitable properties that are required for the application. It is safer to analyse the films regularly during the manufacturing process, in order to have realistic expectations of the final product, or to establish a repeatable manufacturing process.

Various methods are used to characterize YBCO thin films and some of them were used in this project. The concepts, procedures and results of the characterization techniques that were used are given in this section.

4.2.2.1 X-Ray Diffraction

The X-Ray Diffraction (XRD) technique is commonly used for characterization of the structure of crystalline materials. It is based on the principle that crystals act as diffraction gratings for X-rays, as established by Max von Laue, winning him a Nobel Prize in 1914.

Figure 4.5 illustrates a simple explanation of the diffracted beams from a crystal, as explained by W. L. Bragg. An incident beam of X-rays is considered to be reflected, in partial amounts, by parallel planes of atoms spaced by a distance d. The beams

are diffracted if the reflection results from constructive interference.

This is only possible if the path difference GE+EH $= 2d\sin\theta$ is a multiple of the wavelength,

$$2d\sin\theta = n\lambda,$$

where n is a positive integer, and $\lambda \leq 2d$. A strong reflected beam is only obtained for certain angles though [88].

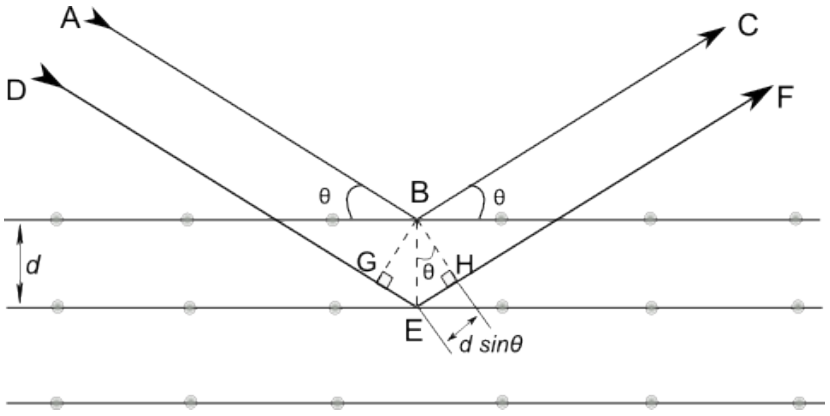

Figure 4.5: Schematic diagram of a diffraction grating of a crystalline material. The horizontal lines represent the atomic planes (Bragg planes) that reflect the incident X-ray after diffraction into the material (Adapted from [88]).

XRD characterization can be used to quatify the stoichiometry and oxygen content of YBCO films.It has been shown that the c-axis lattice parameter tends to diminish with increasing oxygen content [109]. The oxygen content can also be correlated to the structure. Wrong oxygenation results in wrong peak intensity ratios. The missing peaks tell about missing planes in the crystal lattice (See Fig. 4.6), which might be due to an incorrect stoichiometry.

The CuO_2-planes are parallel to the ab-plane, and common to cuprate HTS. By pumping the oxygen in and out through the CuO chains (along b), one can vary the oxygen content from 7.0 to 6.0. From the above, $O_{6.64}$ to $O_{7-\delta}$ will result in a superconducting YBCO crystal [88].

The c-axis oriented YBCO crystal lattice has seven planes superposed along the c-axis of its primitive cell. This means that the XRD characteristics of a c-axis grown YBCO film should show at least seven peaks that correspond to the planes. Figure 4.7 shows such an XRD characteristic of an YBCO thin film produced by ICM sputtering.

This technique was especially used to solve the problem of non-superconducting YBCO films deposited using ICM sputtering. This problem was noticed when all the tested SQUID structures, believed to be superconducting in the beginning, showed

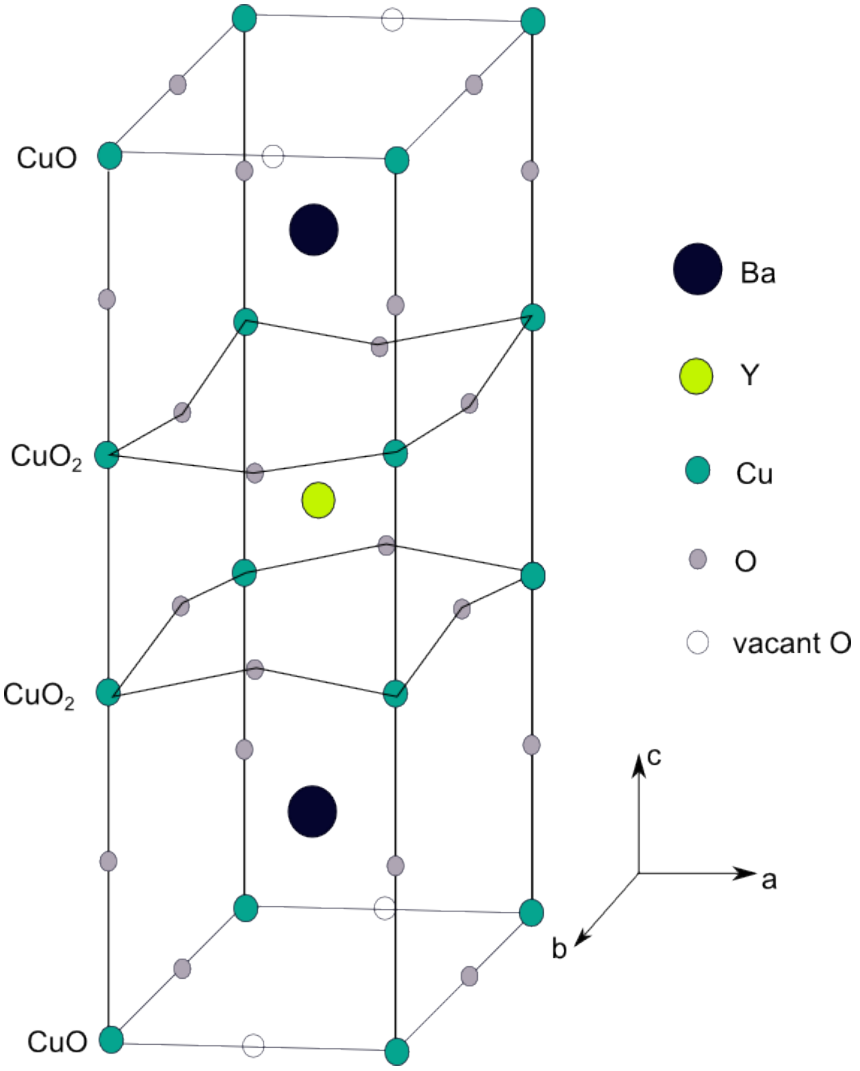

Figure 4.6: Orthorhombic primitive cell of an YBCO crystal structure. The cell dimensions of $YBa_2Cu_3O_7$ are a=3.88 Å, b=3.84 Å, and c=11.63 (Adapted from [88]).

a metallic or semiconducting behaviour.

Four samples were characterised by means of XRD, and compared to the XRD database of $Y_1Ba_2Cu_3O_{7-\delta}$, and to the XRD characteristics of the YBCO pellet, supposedly similar to the target used. The comparison turned out to be indecisive, and the reason for the difference was thought to result from either the wrong stoichiometry, or from the XRD source of rays that was used. Even if there was an error in the measuring instrument, it was still evident that something was wrong with the samples, according to the susceptibility tests that were done.

In this case, it was only possible to check the reasons that could have contributed to the wrong stoichiometry, and the sputtering unit had to be thoroughly serviced and the deposition chamber cleaned from impurities. The target had to be sanded

thoroughly, and run under plasma for a further cleaning. The annealing process had to be extended to ensure that no oxygen deficit was encountered. The problem was then solved. It was found that the YBCO target was prone to contamination and every time, when taken outside the deposition chamber, it had to be cleaned (by plasma ignition) before a proper deposition could be made.

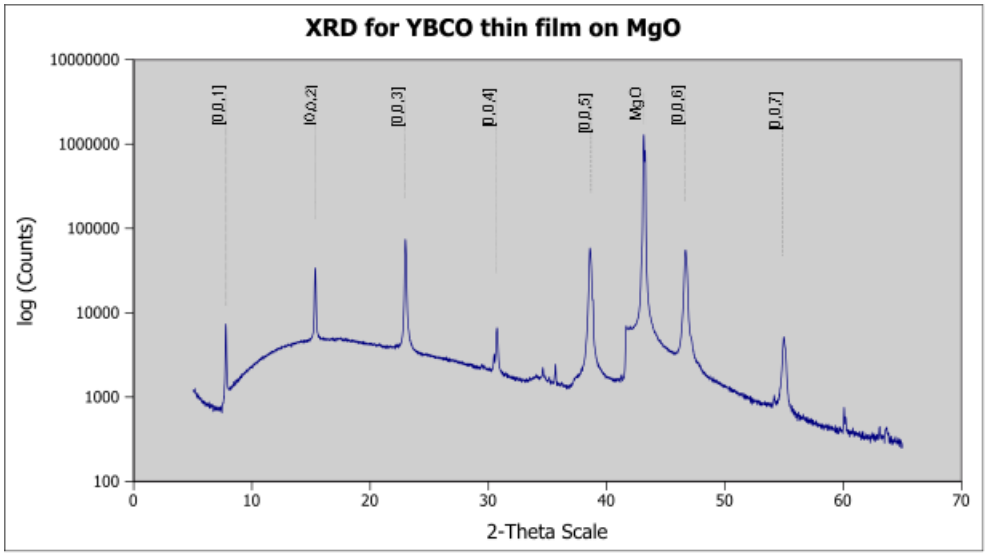

Figure 4.7: X-ray diffraction characterization of c-axis $Y_1Ba_2Cu_3O_{7-\delta}$ thin films deposited on MgO by a dc sputtering technique.

4.2.2.2 Susceptibility vs temperature

The second property that superconductors are known for, in addition to zero resistance, is that of perfect diamagnetism. They repel magnetic fields applied to them. These properties are commonly exploited to study the properties of superconductors.

Susceptibility measurements, which are based on this second property, were used to study the properties of YBCO thin films used in this thesis. The YBCO film, grown on a 10mm×10mm MgO substrate, was placed between two coils, one generating a magnetic field from the front of the film and another, at the back of the substrate, receiving the field transmitted through the sample undergoing the test. The sample is cooled down slowly. When the sample temperature is above its T_c, the field is fully transmitted to the receiving coil. When it reaches its critical temperature, it expels the field and the recorded susceptance becomes minimum (zero if the measuring device is well calibrated). The measured susceptance values were continuously recorded with the temperature controller software, together with the values of the temperature, and directly plotted on a computer.

The system used for these measurements comprises of a cryocooler working with liquid nitrogen, a cold finger where the sample is placed, the cryogenic measurement system, and a computer to view the graphical results of the measurements and save

the data file for later use. A typical example of the susceptance versus temperature graph is shown in Fig. 4.8. The sample was deposited using PLD and had a critical temperature of T_c = 89K, with a transition width of 0.25K. The graph shows lower values of the temperature (T_{offset} = 9K) and susceptance (min = 18%) due to calibration poblems.

This system was also intended to perform four point resistance measurements of the film, but this channel was already broken by the time the susceptibility measurement were done.

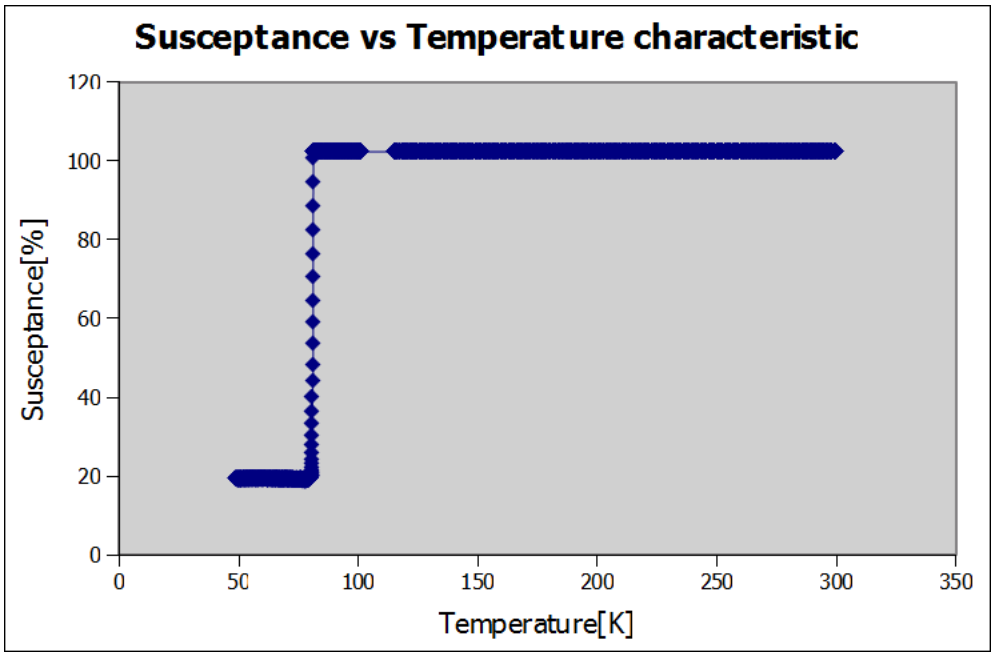

Figure 4.8: The susceptance versus temperature characteristics of a $Y_1Ba_2Cu_3O_{7-\delta}$ thin film deposited on MgO by PLD. The critcal temperature is T_c=89K and the transition width δT=0.25K.

4.2.2.3 Surface morphology

The surface of YBCO thin films is expected to be as smooth as possible to yield well defined device structures. For example, the boulders often encountered on PLD grown films, if they happen to be located at the junction site, are likely to impair the definition or even the properties of grain boundary or step-edge junctions [97], because they are not superconducting. The same could happen if a boulder happened to be placed along the constriction used to form the Josephson junction.

The surface morphology is known from the analysis of the surface roughness by means of the AFM. A roughness of 15 nm is needed for high quality DC SQUIDs, but a roughness of 300 nm is still acceptable [97]. The YBCO films that were fabricated had surface roughnesses ranging from 7 nm to 45 nm, which are acceptable

for DC SQUID fabrication. An example of the surface roughness of an YBCO thin film is shown in Fig. 4.9.

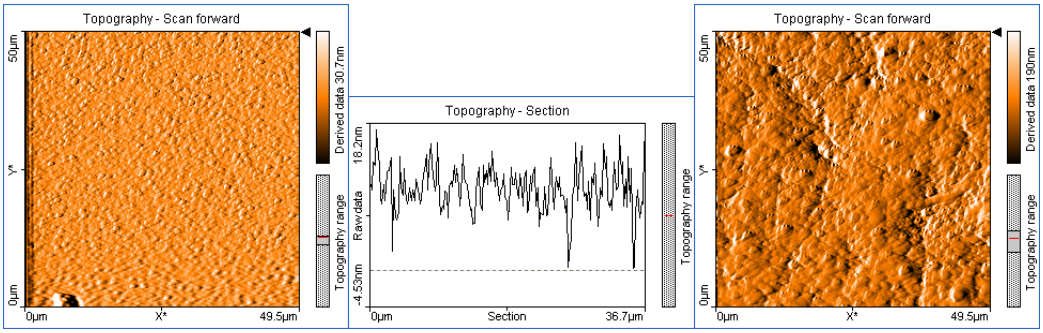

Figure 4.9: AFM picture of an YBCO film deposited by ICM sputtering, showing the roughness of the surface (left). The cross section of the surface of a superconducting YBCO thin film, with the surface roughness strictly less than 18 nm (middle). PLD YBCO film surface, showing a surface roughness much worse than the ICM sputtered case, with noticeable big boulders (right).

4.2.3 Lithography

Lithography is a process of engraving a desired structure onto a material surface. In HTS applications, it is commonly used on thin films to fabricate micron- or nano sized devices. It is a photographic process, where a light-sensitive plaque (film) is exposed to light and developed to give the image of the light source. In this project ultraviolet (UV) lithography was used. UV lithography uses UV light to make structures on a thin film by irradiating a photo sensitive material (photoresist) applied on top of the film. When exposed to UV light the photoresist will be altered, and when developed, an exposed positive photoresist will be eaten away, and an exposed negative one will remain.

In order to make a structure, a mask can be used that will cover the regions that are to remain when using a positive resist. For negative photoresist the mask will have the opposite layout.

For good lithography, parameters such as exposure time, the UV light properties, the development time, etc., have to be optimized.

In this project a chrome mask, on which a SQUID structure was defined, was used. The sample has to be aligned with the mask (chrome side facing the sample), using micrometric screws. It is very important that the sample touches the mask completely, as any spaces between them will lead to unresolved structures, or wide side angles.

Samples were exposed for 15 seconds and directly developed for 35 seconds. The development was done by rotating the sample clockwise, anti-clockwise, and moving

it up and down while immersed in the developer. Structures with 3μm linewidths were well defined. The exposure system that was used is available at Stellenbosch University and is able to define linewidths of about a micron. A positive photoresist (SPR700 from Microresist Technology) was used with its developer (MF-26A, also from Microresist Technology). Alternatively, the S1818 positive resist (with the same developer) was used only in cases where chemical etching was used, because its was found to be not hard enough to resist the Ar^+ milling process [102]. Figure 4.11 shows a SEM picture (with dimensions) of a washer SQUID patterned by UV lithography. The full UV lithography process is sketched in Fig. 4.10.

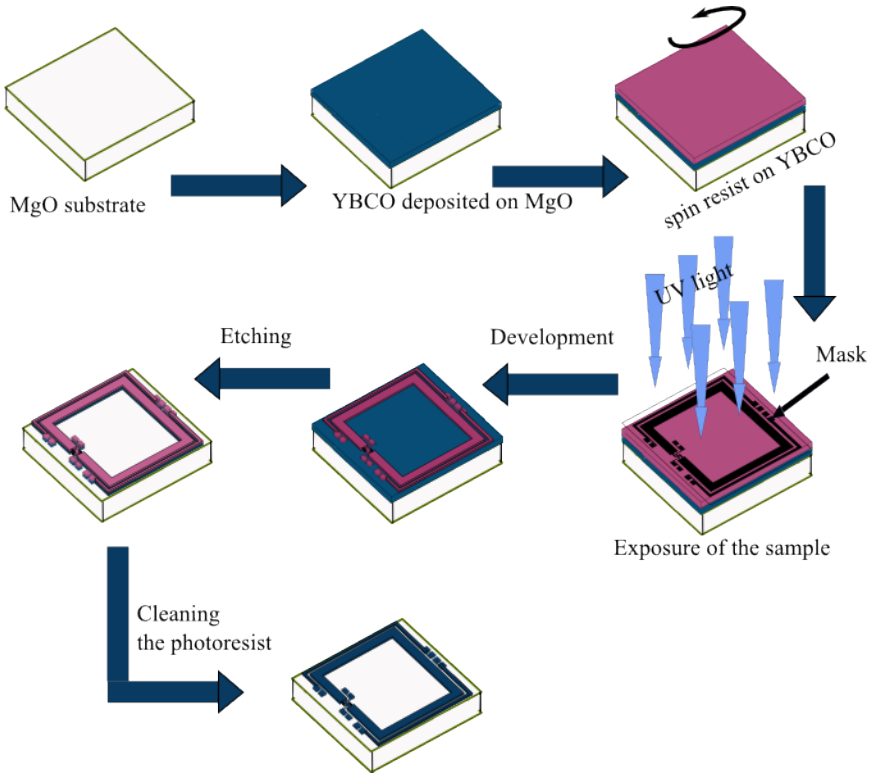

Figure 4.10: SQUID fabrication process using UV lithography. The chrome mask was designed at Stellenbosch University.

4.2.4 Etching of the circuits

Two types of circuit etching were used, namely wet etching and dry etching.

Wet etching consists of washing the sample in a proper chemical to remove the unwanted parts of the sample. The chemicals that are commonly used in this case are non-aqueous bromide in ethanol, sulphuric acid, nitric acid and citric acid, which was used in this case. An amount of 10g of citric acid was dissolved in 500ml of deionized water, which was the concentration used by previous students. The samples were etched by immersion in an ultrasonic bath with the mentioned etchant. The samples were completely etched in about 40 seconds. Unfortunately, after cleaning the resist

in acetone, the $Y_1Ba_2Cu_3O_{7-\delta}$ tracks appeared to have been undercut.

In order to solve this problem a weaker concentration of acid had to be used. Two drops of the previous solution were added to 50ml of deionized water, and the samples were etched slowly by blowing the resulting liquid onto the sample by using a pipette. A sample could be etched in about four to eight minutes, depending on the thickness of the $Y_1Ba_2Cu_3O_{7-\delta}$ film. This way of handling the wet etching was successful in the sense that the $Y_1Ba_2Cu_3O_{7-\delta}$ tracks were not eaten away. Less than a micron in total was eaten away from both sides of a SQUID leg.

Care has to be taken though, when performing wet etching in such a way. Leaving a sample for too long in a wet etchant solution will destroy its superconducting properties, which is bound to happen when etching thick layers of $Y_1Ba_2Cu_3O_{7-\delta}$ in very dilute solutions. Reasonable dilution of etchant and thickness of the thin films should be used. Exact values remain a decision of the manufacturer.

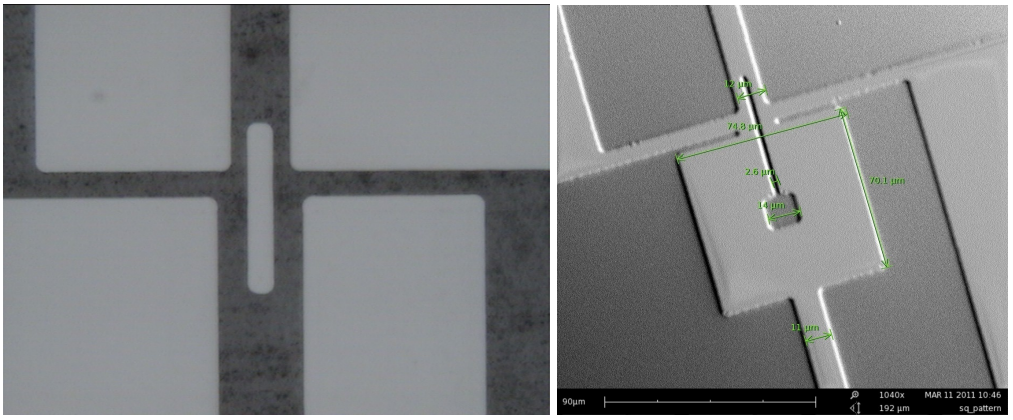

Figure 4.11: Left: A dc SQUID structure patterned by UV lithography and etched by wet solution of citric acid. The optical microscope picture shows no significant reduction of the YBCO lines in width. Right: Large area SQUID patterned by UV lithography and etched by Argon ion milling. Picture taken with a Scanning Electron Microscope from the microelectronic lab at the University of Stellenbosch.

In dry etching samples are milled by means of argon ions. After a sample has been hard baked, it is exposed to a beam of argon ions, continuously generated in the chamber as a plasma by an RF antenna. The ions are accelerated by attraction towards the sample, placed on a negatively grounded water cooled sample holder. The RF antenna is operated by a 50W source at 13.56 MHz. On contact with the sample, the energized ions erode the uncovered surface and leave the structure that is protected by the resist intact.

The bombardment erodes the sample surface, but can also cause damage by ion implantation. Rotation of the sample and the angle of attack are important factors that can be adjusted to solve this problem.

In the setup that was used the sample was tilted by about 20° relative to the vertical axis of the ion beam, and shut off at times by a rotating shutter mounted on the sample holder. The shutting and exposure timing was set to 1:2 periods of time respectively, and this protected the sample from ion implantation [104]. The etching time was about 1h 15min for a 200 nm thick sample. In [112] Mapar et al. used a rotating sample instead of a shutter, with a tilt angle of 5°, and were able to anisotropically etch a thickness of 270 nm within two hours. Parameters such as tilt angle, rotation, etc., can be varied according to the system setup, and the desired results.

4.2.5 Deposition of contact pads

In order to connect the SQUID to the external circuitry, contact pads were needed. Silver or gold are preferred as they do not react with $Y_1Ba_2Cu_3O_{7-\delta}$. Silver was chosen in our case, for it can be annealed at lower temperatures than is the case for gold. This prevents $Y_1Ba_2Cu_3O_{7-\delta}$ from losing oxygen, which easily happens at high temperatures. During annealing silver allows oxygen through to diffuse into the $Y_1Ba_2Cu_3O_{7-\delta}$ layer, which is another advantage of using silver pads.

The deposition of contact pads was done under vacuum, in a thermal evaporator. After etching, the sample is placed in a sample holder, covered with the pads mask and screwed tightly onto the holder. The mask is a copper sheet with holes placed exactly where the pads are prepared to fit onto the sample. The alignment between sample and mask was done under an optical microscope. After the sample was put in the vacuum dome, facing a crucible full of silver balls, a vacuum was created down to 10^{-6} mbar, and a current of $>$250 A was delivered to heat the crucible. The deposition rate of silver could be controlled well and monitored on a computer, until a fair thickness of pad was reached. After deposition, the vacuum had to be broken and the sample recuperated. A picture of the thermal evaporator used is shown in Fig. A.4 in Appendix A

After deposition of the pads they need to be annealed. During annealing the pads harden to allow better wire bonds and diffusion into the $Y_1Ba_2Cu_3O_{7-\delta}$, reducing the contact resistance. The anneal was done at 490°C in an oxygen environment to prevent the film from losing oxygen. The pressure is important here to ensure diffusion back into the superconducting material. The highest yield was obtained at atmospheric pressure. The annealing profile for contact pads is shown in Figure 4.12.

4.2.6 Wire bonding and packaging

The completed SQUID had to be put in a package that is appropriate for testing and the intended use or application. In this project a printed circuit board (PCB) was needed to test the SQUID. The sample was attached to a copper block, onto which a hollow PCB had been glued. The contact pads were bonded onto the copper tracks of the PCB with very fine gold wires, by using a sonic wire bonder (WEST · BOND, RRS 600637/2).

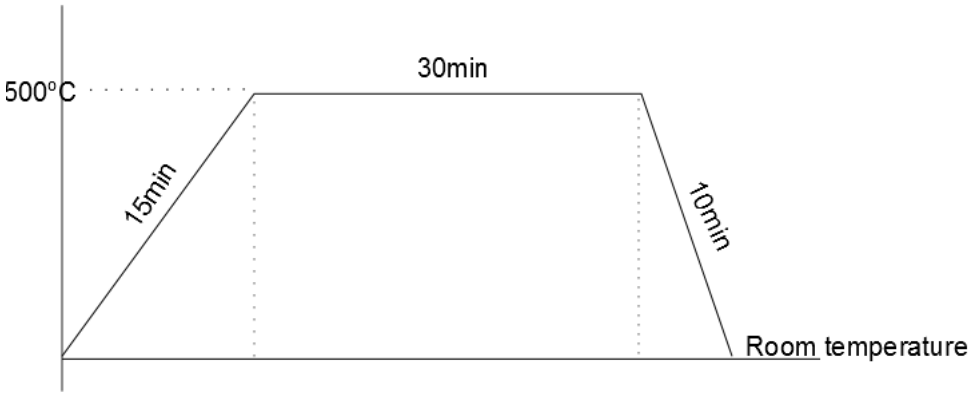

Figure 4.12: Annealing profile used for the films after deposition of the contact pads.

At least two bonds had to be made between a pad and a copper track of the PCB, to ensure that, if one breaks, the other would stay. The PCB and the sample had to be in tight contact with the copper block, so that no vibrations would dampen the vibrations from the tip of the wire bonder. The complete assembly is shown in Fig. 4.13.

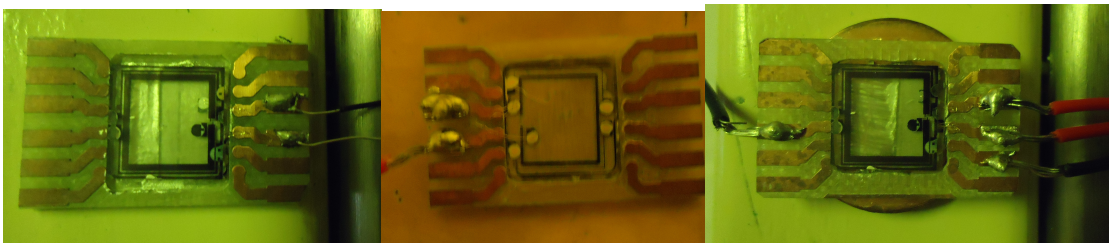

Figure 4.13: DC SQUID mounted and wire bonded onto a PCB for testing.

4.2.7 Fabrication of Josephson junctions on a SQUID template using AFM nanolithography

Josephson junctions are the building blocks of a SQUID. They were implemented by using two different methods, namely AFM nano-ploughing and a new double resist laser lithography method. AFM nano-ploughing comprises the scratching of micro-constrictions on the SQUID legs of the structure obtained after UV lithography.

Diamond coated silicon AFM tips were used for static ploughing AFM nanolithography [102]. This was done by directly scratching the SQUID legs with an AFM probe. Such a process was performed at a speed of 4 μm/s, with a tip loading force from 60 to 70 μN. The defined constrictions were about 700 nm wide and 400 nm long. The results of a typical AFM-scratched SQUID structure are shown in Fig. 4.14.

Micro-constriction structures are known to usually display the same characteristics

as Josephson tunnel junctions. Nevertheless, in this case no sample resulted in a working SQUID. This was mainly due to the difficulty of reproducing the desired results of the scratching process.

A characterisation of the scratching process was established (results not reported), but the implementation of a repeatable process was unsuccessful. This seemed to be due to the instrument itself, probably the deterioration of the tips. To address this problem a special and extensive examination of the complete process on the specific instrument will be required. The process itself was successfully used to implement micro-bridge Josephson junctions on YBCO, using a different AFM system from the Department of Chemistry & Polymer Science (Stellenbosch University).

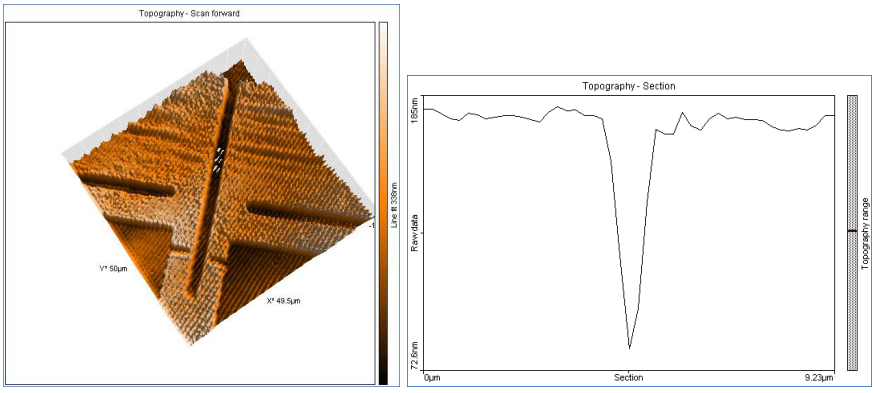

Figure 4.14: AFM-scratched bridges on the legs of a washer SQUID. The constrictions are of the order 0.9 and 1μm wide (left). Topographic cross section of a scratch by the diamond coated silicon AFM tip (right).

4.2.8 Nano-bridge based SQUID patterned using a Double-Resist Laser Lithography Method

Due to the difficulties in achieving the repeatability of the AFM implementation of micro-bridges, a novel method was used to implement nano-bridge weak links as Josephson junctions. A new in-house developed Double-Resist Laser Lithography (DRLL) system (see Fig. 4.18) was used to perform the tasks of engraving micro-structures of superconducting circuits on $Y_1Ba_2Cu_3O_{7-\delta}$ thin films, deposited on MgO substrates.

The system consists of a set of three stepper motors that allow motion in three dimensions. A laser pointer, fixed on top of the system, draws designed structures on a sample, placed on top of the stepper motor system, just below the laser. The resolution of the system is 3.6 μm, and the step size is 380 nm.

The DRLL method consists of superimposing two overlapping structures by performing the lithography in two successive steps. By applying positive photoresist, small structures were defined, followed by the definition of large structures, this time

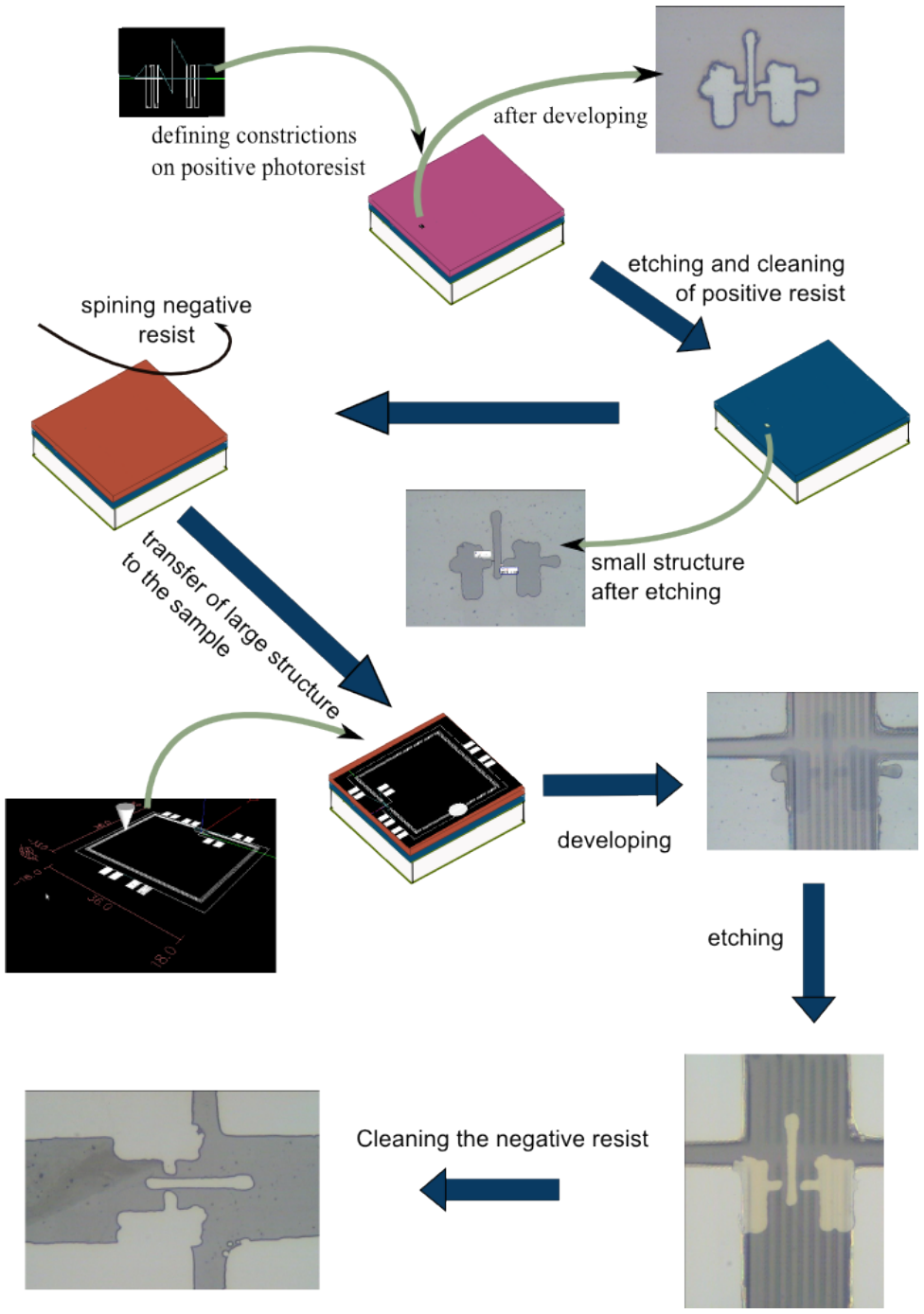

Figure 4.15: Lithography process using the laser system and the method described in Section 4.2.8.

with negative photoresist.

In this project the small structure consisted of the SQUID loop surmounted by two micro/nano-bridge structures. The big structure comprised the outside circuitry of the SQUID (external loop, circuit tracks and contact pad areas) and represented

the full size of the SQUID area.

Even though the resolution of the laser system is much larger than the dimensions of the smallest structure needed, the motors' step size and the laser source height adjustment, combined with the use of positive resist, allowed for the patterning of submicron structures. Figure 4.16 shows the micro- and nano-constrictions that were manufactured by means of this method. After the bridges were implemented, neg-

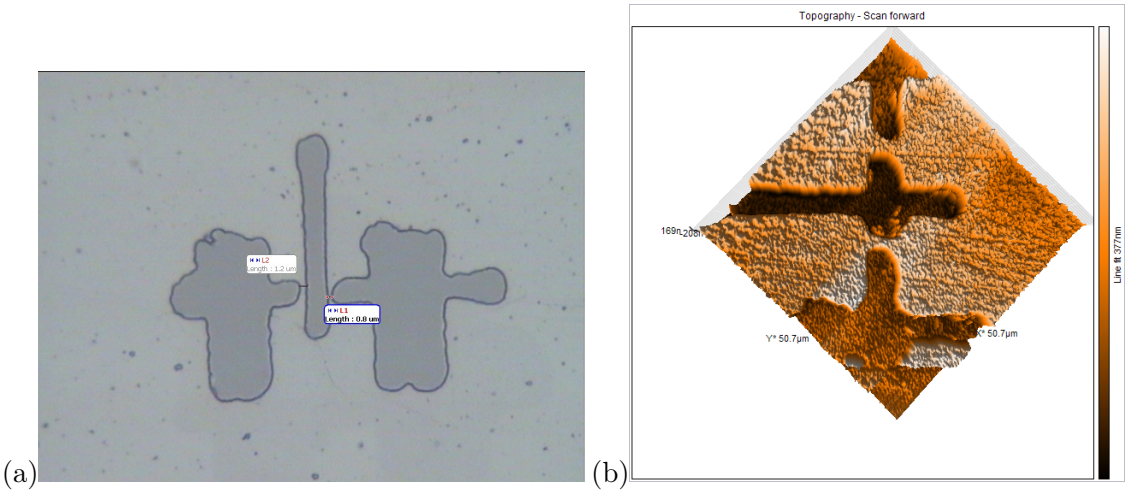

Figure 4.16: a) Micro-constrictions fabricated by laser lithography along a loop of superconducting $Y_1Ba_2Cu_3O_{7-\delta}$ film. The constriction widths are of the size 1.2μm and 0.8μm. b) AFM picture of nano-bridges defined by laser lithography.

ative photoresist was used to perform full lithography, on top of the constrictions. Figure 4.17 shows such a superposition after the full double lithography process. The most stringent issue to deal with in this method is the realignment of the sample to get a perfect fit of both structures. This is hindered by the stepper motors that do not move back to exactly its original rest point. The alignment of the sample in the groove is only manual, but it can be improved by incorporating a microscope into the system for better alignment. The full laser lithography method is shown in Fig. 4.15.

The laser system has shown some instability in terms of resolution. This is thought to come from either the overheating of the chips that control the motors' movements, or the way the laser is pulsed, switching the laser on and off as the drawing is executed. This is only an issue for very small structures, with dimensions less than the actual resolution of the system, and solving this problem would only require minor adjustments and replacement of a few parts with the correct specifications.

Another issue is that the laser has to be switched on and off all the time This results in broad lines at the points where the laser comes on. The resulting malformations are unwanted in SQUID structures, as they are the sources of $1/f$ noise.

The main advantage of this method is the flexibility in dealing with the design

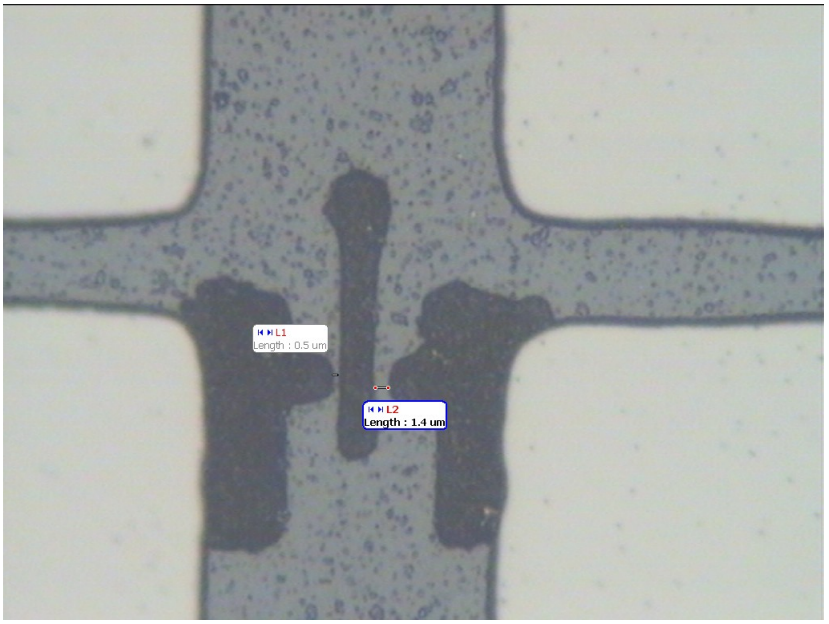

Figure 4.17: SQUID loop with bridges as junctions, fabricated by a laser lithography, double resist combination.

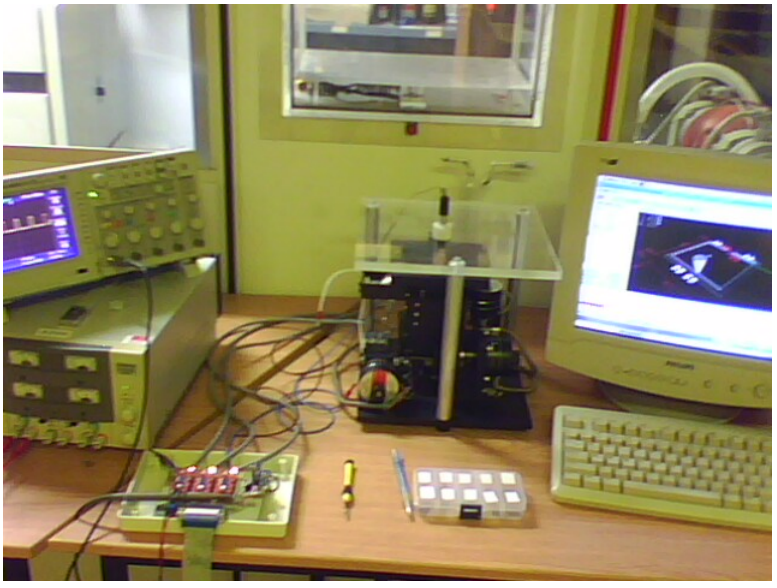

Figure 4.18: Laser lithography system

of devices. The constrictions can be made directly, without exposing an unprotected YBCO film to the atmosphere for hours, as is the case with AFM scratching. This process can easily be repeated, when compared to AFM scratching. It is, however, necessary to mention that repeatability will be enhanced by the improvements proposed above.

4.3 Testing

In this section the testing of the dc SQUID, that was manufactured as reported in Section 4.2, is discussed. The correct operation of the device with respect to the theoretical characteristics, such as the current-voltage relationship and its response to an externally applied changing magnetic field, was verified. This process also allowed for the deduction off the main characteristic parameters of the manufactured device, such as the critical current and the normal resistance, from the device's characteristic curves.

The test equipment used in this work consisted of a *Mr SQUID* system modified to supply enough current for junctions of higher critical currents than normal, the *Mr SQUID* probe circuitry (see Appendix B) adapted for supplying the bias current to the SQUID under test, a liquid helium cryogenic system or a liquid nitrogen dewar, which were alternatively used depending on whether the sample T_c was lower or higher than the liquid nitrogen temperature. A cryogenic measurement system, a cold finger, and an oscilloscope or computer for displaying the characteristic curves were also used.

Samples with a T_c lower than 77K were placed in the cold finger and connected to the *Mr SQUID* system via the channels for resistance measurements in the cryogenic measurement system. The *Mr SQUID* unit is used as the signal generator and low noise amplifier (10000×) of the SQUID output. The output of the SQUID supplies the signal for the Y-channel of the oscilloscope, which is plotted against the input and displayed on the oscilloscope's screen.

Samples with a T_c higher than 77K were immersed into a dewar full of liquid nitrogen and, after the liquid bubbling had stopped, the signal generator was turned on, which resulted in a display of a V-I curve on the screen of the oscilloscope. The SQUID testing setup is shown in Fig. 4.19

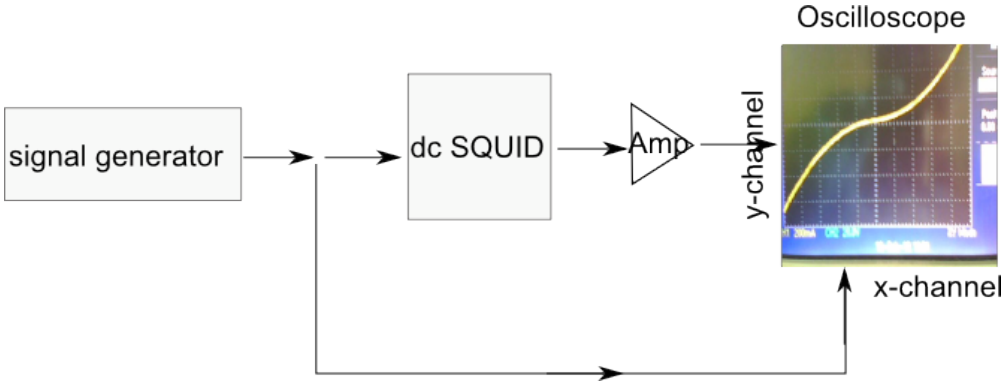

Figure 4.19: Setup of the apparatus used to test the SQUID in this project. The dc SQUID tested had $I_c = 20\ \mu$A, and $R_n = 5.5\Omega$.

A single valued V-I curve was observed for the tested dc SQUID, which corresponded well with the design expectations (Section 4.1). The characteristic parameters of the fabricated device were calculated from the V-I curve, and were found to be $I_c = 20\mu$A and $R_n = 5.5\Omega$. These results were also in accordance with the simulation results, as shown in Fig. 3.22 and Fig. 3.18(a), where, for an overdamped Josephson junction, the V-I curve of a dc SQUID is expected to be non-hysteretic.

An observation of the critical current modulation by a changing magnetic field was also performed. By approaching and retracting a magnet to and from the device under test, the V-I curve was shown to squeeze in and out respectively, which corresponded to the expected modulation, as indicated in Fig. 3.13 and predicted by simulation, as shown in Fig. 3.22. The measured V-I curves, at two different positions, obtained during flux modulation are shown in Fig. 4.20.

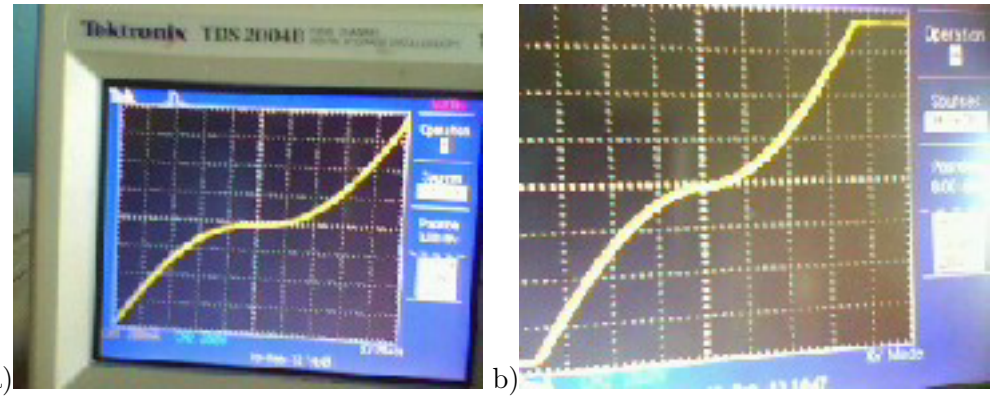

Figure 4.20: V-I curve of the tested SQUID at extreme positions during flux modulation: a) no magnetic field applied ($n\Phi_0$), b) magnet in the proximity of the device under test.

The *Mr SQUID* system provides channels to quantitatively measure the voltage flux modulation of a dc SQUID. This can be done by adapting the *Mr SQUID* probe, especially the C_{in} or C_X channels, which are shown on Fig. B.3. These channels could be connected to the outermost external loop of our dc SQUID chip. In this case, the *Mr SQUID* should be set to the $V-\Phi$ instead of the $V-I$ mode. The signal supplied to the outermost coil couples the flux into the SQUID via the pickup coil of the SQUID, as this is a directly coupled SQUID. This quantitative measurement could be done in the future, for further characterization of these devices.

4.4 Summary

In this chapter the design and manufacturing processes of a dc SQUID were presented. After completion of the fabrication processes, the device was tested, and the testing procedure and measured results were also given in this chapter. The methods used during the manufacturing process were emphasized, the failures and the solutions that were tried to achieve a successful fabrication process, including an improved wet etching process, were reported. A new laser based lithography method,

in which two different types of photoresist (positive and negative) are used to superimpose two complementary structures, was implemented in this project, and used to solve the problems related to the definition of nano-bridge Josephson junctions by AFM nanolithography.

A working high-T_c dc SQUID device was manufactured and the test results of the device were reported. The measured results corresponded well with to the predictions established in Chapter 3.

This device was designed and manufactured with the intention to provide a prototype usable in a high-T_c SQUID-NMR system. The integration of such a system presents many important aspects, and the main ones are presented in the next chapter, with a focus on the on-line application of such a system.

Chapter 5

Application of SQUID to NMR

The SQUID application to NMR has made low-field NMR possible and brought tremendous advantages of the latter over high-field NMR. Although the applications of SQUID-NMR are numerous, our attention will primarily be focused on the non-destructive evaluation of food products. In this chapter the design considerations of a low-field NMR system, where a SQUID is used as the sensor, will be summarized. A brief overview of low-field NMR is also given.

5.1 Low-field NMR/MRI

The active interest in very-low or ultra-low field NMR is motivated by the cost, size and ease of access to the sample. Both the cost and size can be drastically reduced, and for the latter, the sample need not be inside the magnet enclosure [31]. Imaging in the earth's magnetic field is also made possible in low field NMR [113].

It has also been shown that low-field MRI can give undistorted images (with some restrictions [8]) in the presence of a metal (e.g. an orthopedic screw), which is not possible at high fields [114].

The repeated call to reduce the cost of NMR can primarily be attributed to requirements for high magnetic fields. Low-field ($B < 1$T) NMR devices have been developed by different researchers, where normal electromagnets and permanent magnets are mostly used to generate the polarizing field, and not the extremely costly superconducting magnets.

In [24], Hills reiterated the enormous potential of low-field NMR in the food sciences, and many researchers have proved that in different applications [33], [32], [31], [6], [115]. Presently, most low-field relaxation studies on food articles, are one-dimensional, with a fixed spectrometer frequency, and a single target nucleus.

Progress is being made to produce a low cost, low-field instrument that is hand-held or that can be used on a sorting line [116], [25], [117], [118]. Industrial NMR systems are mainly for internal inspection, and need satisfactory performance under conditions of motion.

Such systems have been researched and applied on pit detection in cherries [4] at speeds from 0 to 250 mm/sec (2T), maturity in avocadoes [4], detection of freeze injury in citrus (50-100 mm/sec, 4.7T), seed identification by images [119], [120] and internal browning in apples (0.13T) [121].

All these technologies are still to be made reliable and cost effective for industrial application and this calls upon a closer collaboration between researchers and the industry.

5.2 Aspects of SQUID-NMR system development

According to Greenberg [99] a SQUID could be the only device able to measure the change in longitudinal spin magnetization. A SQUID converts magnetic flux to voltage independently of the frequency, at an exclusively high sensitivity. The homogeneity of measurement fields thus needs not be high for obtaining narrow spectral lines, with high S/N ratios. Substantially greater $T1$-weighted contrast is achievable at low field than at high fields [9], [8].

Due to the fact that SQUIDs detect the variations in the transverse and longitudinal magnetization, they do not depend on the resonance frequency. They can operate at frequencies lower than 200kHz. The SQUID has been used to measure both the longitudinal and transverse spin magnetization at low field, where different elements were targeted for various purposes [99].

In practice, a SQUID does not measure the magnetic field directly, but the change in the magnetic flux due to a varying magnetic field. The change in magnetic flux in the SQUID loop is given by

$$\Delta\Phi = \frac{k}{2}\sqrt{\left(\frac{L}{L_p}\right)}\Delta\Phi_c, \tag{5.2.1}$$

and is due to $\Delta\Phi_c$, the variation of the magnetic flux in the pickup coil. L and L_p are, respectively, the inductances of the SQUID and the pickup loop, and k is defined in (5.6.1).

5.3 Prepolarizing field

The low-field NMR technique requires the object under evaluation to be subjected to a pre-polarization magnetic field. It might be a single or multiple pulse pattern, produced by a single or pair of coaxial, fluid cooled, resistive, air core electromagnets [122].

Clarke et al. [8] performed the NMR expriments on mineral oil in the absence and in the presence of a prepolarization field. In the latter case they obtained an improved spectrum in terms of S/N ratio, line broadening, and signal height enhancement (by

a factor of B_p/B_0) [123]. Signal averaging also required a smaller number of scans to achieve a sufficient level of spectral resolution. They came to the conclusion that a relatively smaller constant magnetic field, with a prepolarization field, improves the quality of the spectrum in most aspects. With a prepolarizing field (1.8mT) three orders of magnitude higher than the constant magnetic field (1.8μT), they achieved a reduction of the line width and the resonance frequency by three orders of magnitude.

A typical prepolarizing pulse pattern can be seen from the examples in Appendix D. During the measurement time the prepolarizing field is turned off, and the cooling is fully effective. In the design of Sims et al. [122] the coil and power supply, for a 50% duty cycle, use perfluorocarbon fluid as the active liquid cooling to avoid overheating of the magnet windings. The coolant might have some restrictions, depending on whether or not it would affect the measurements, as in clinical applications where it should not be a conductor of electricity, etc. Charles et al. [124] used a continuous flow of water. Some designs use liquid nitrogen as coolant, when possible interference from the water protons of the coolant is to be avoided.

5.4 Configuration of the coils for magnetic fields.

Low-field NMR requires a number of coil systems, each one with a specific role. The main types are a magnet (or electromagnet) to produce a static field B_0, the transmitter coil to give the pulse sequences and a measurement coil that receives the spin magnetization response. To these are added the coils to cancel the magnetic field and the prepolarizing field coils. The frequencies and magnetic field strengths are greatly reduced with low-field NMR.

In the case of 3-dimensional MRI three sets of gradient coils are added in the X, Y and Z directions. A Maxwell pair of coils can be used for the diagonal field gradient ($\delta B_z/\delta z$), with biplanar coils for off-diagonal ones ($\delta B_z/\delta x$ and $\delta B_z/\delta y$) [8]. In most cases a couple of Helmholtz pairs are used to generate the static magnetic field.

A component of the earth's magnetic field can be used to supplement the field of the coils that are used to provide B_0. One or two Helmholtz pairs can be added for field homogeneity enhancement.

The values of the magnetic fields to be generated and the sizes of coils depend essentially on the designs and intended applications of the instruments, sample sizes, etc.

5.5 Noise considerations

One way of looking at the noise in SQUID-NMR systems is derived from the concept of S/N ratio in conventional NMR systems, in terms of the energy resolution of the SQUID.

The magnetic flux $\Delta\Phi_c$ coupled to the detection coil is related to the variation

in the sample magnetization ΔM as

$$\Delta\Phi_c = \Delta M \beta V_S, \tag{5.5.1}$$

where $\beta = B_c/I_c$, with B_c the magnetic field that would be induced in the coil by a current I_c, supposedly circulating in it, and V_S is the volume of the sample [99]. β is related to L_p and the volume V_c of the coil by

$$L_p = \frac{\beta^2 V_c}{\mu_0}. \tag{5.5.2}$$

The combination of (5.2.1), (5.5.2), and (5.5.1) leads to the following expression of the signal to noise ratio:

$$\psi_S = \frac{\Delta\Phi}{\sqrt{S_\Phi \Delta f_s}} = \sqrt{\left(\frac{\eta V_S \mu_0}{\epsilon_{SQ}^{(e)} \Delta f_s}\right)} \Delta M. \tag{5.5.3}$$

If the measuring procedure is taken into account, ΔM would be related to the intrinsic magnetization by $\Delta M = \alpha\chi B_0/\mu_0$, and finally

$$\psi_S = \alpha \sqrt{\frac{\eta V_S}{\mu_0 \epsilon_{SQ}^{(e)} \Delta f_s}} \chi B_0. \tag{5.5.4}$$

The entities in the two equations above, and what they represent, are as follows:

- Δf_s is the output bandwidth of the electronics;
- η is the filling factor. It contains the indirect dependence of the S/N ration to the geometry of the coil;
- $\alpha = 1 - \cos\theta_p$ for pulse excitation;
- $\epsilon_{SQ}^{(e)}$ is the energy resolution of the SQUID; and
- S_Φ is the flux noise.

One can easily estimate the value of the S/N ration by reasonably giving values to the entities above and replacing them in (5.5.4) [99].

5.6 Design of the pickup coils

The detection coil is a flux transformer in a gradiometric configuration [8], and coupled to the SQUID. Field fluctuations surrounding the gradiometer are thus rejected, and only the magnetic field from the sample, placed close to or in one of the loops of the gradiometer, is detected.

An important point to take into account is the way signals from the pickup coils are coupled into the SQUID. This is characterized by the mutual inductance between the transformer and the SQUID, which is given by

$$M_{CS} = k\sqrt{L_C L}, \tag{5.6.1}$$

with L_C the inductance of the input coil of the flux transformer and k the coupling constant. For a better coupling, k is expected to be optimal, the inductance of the pickup loop to be equal to that of the input coil [99] and the signal channelling wires to be lossless and noiseless.

5.7 Permanent magnets

In some cases low-field NMR constant magnetic fields and shimming fields are created by permanent magnets. The intrinsic properties of the magnets and their configuration are the important factors in defining the sample volume and the inhomogeneity, defined by local gradients. These magnets are very sensitive to temperature fluctuations, that can be due to either the outside temperature or the samples themselves (e.g. samples from cold storage). Eustace [125] reported a reduction of 1% in soluble solids (in the range of 0 to 20%) for a 1°C change. One should thus expect possible attenuation in the signal in such cases.

Magnet configurations and resulting field strength and homogeneity can be modelled and predictively studied for a design. Carsten Horch et al. [115] did such a study and reported the improved possibilities of circular and parallel arrangements of NdFeB permanent magnets, to provide the static polarizing magnetic field for low-field NMR. In their study they used the COMSOL magnetostatic models, and in optimized designs they attained a constant magnetic flux of 115 mT.

Permanent magnets have been used for on-line systems [116], open access systems [33], etc. Experimental techniques are another alternative which and can be used for this purpose.

5.8 Pulse sequences

Pulse sequences vary according to the targeted measurements and are applied to impose specific variations in the magnetization, which will allow the extraction of the desired information for the sample.

Examples of pulse sequences are shown in Appendix D. In the pulse sequence of 3-D imaging (see Fig. D.4), B_p is turned on first for a period of about T_1, while B_0 is constantly applied. Within a 15ms delay after removal, a 90° pulse is applied. A 180° pulse follows after a time τ, during which the gradient pulses are applied. The gradient applied along X remains even all along the measurement and allows the frequency space voxels encoding. The others allow phase encoding and 2-D imaging by omission of one of them [8].

The rf coil should be designed in a way that it will be possible to generate the desired pulses, taking into consideration the power supply feeding the current to the coil. In Figure D.2 an example of a pulse sequence used to measure the T_2 relaxation time is given.

5.9 Sample state considerations

Intensive research on in-line processes NMR systems produces reports almost every year [4], [126], [25], [117], [118], but a lot of technical drawbacks have made it a challenge to find a viable industrial system, and many problems are still to be solved [127].

First, it should be noted that all these problems can be solved, but at an extremely high cost! All considerations here are treated in the context of low cost possibilities.

The first hindrance is the polarization issue where, with a sample moving as fast as on an industrial conveyor, it is almost impossible for it to be fully polarized before the measurement. For a sample to be fully polarized, a polarization time of $5T_1$ (about 5 sec for $T_1 = 1$ sec) is needed. If a sample is moving at a normal conveyor speed (1 to 2 m/s), it would have traveled a distance of 5 to 10 m before the measurement. Actual reports have achieved sample speeds of up to 300 mm/s, which is at least three times less than is actually the case. To be practical, one would need to tolerate the polarization time required and calibrate the signals for relative measurements.

Moving spins tend not to refocus after the 180° refocusing pulses. They experience different local gradients and never return to their initial phase at the expected time. One gets more information about the field inhomogeneity rather than on the sample itself. This effect increases with sample velocity [4].

Chayaprasert and Stroshine [121], sorting apples for internal browning, used a CPMG pulse sequence and noticed an increased classification error as the conveyor speed increased. They did, however, report that improved pre-magnetization would make the measurements possible at high speeds.

Hills and Wright [127] reported a novel single-shot, on-line NMR acquisition protocol for samples moving at high speed. This protocol was used to measure the total soluble content in fruit and oil content in avocados. Such a protocol (see Fig. D.3) seems more successful, as it is time saving and does not require averaging over many scans.

It is undeniable that the use of a SQUID as the NMR sensor gives more flexibility to deal with such problems, and many more that have not been mentioned, can be significantly reduced as well. Nevertheless, this is still a subject of extensive study.

5.10 Summary

In this chapter different considerations regarding design, development and applicability of a SQUID-NMR system were discussed. A focus was drawn to the usage of the system for on-line quality testing and sorting. The use of high-T_c SQUIDs as NMR sensors allow a significant reduction in the cost of such systems, up to

seven times less than a high-field NMR system. High-T_c SQUIDs allowed for the first commercialization [124] of a SQUID-NMR system that can be used for non-destructive quality testing of fruits. This system utilizes a commercial SQUID from Star Cryoelectronics, with bi-epitaxial Josephson junctions. The manufacturing process used in this thesis (Section 4.2) demonstrated a simpler way of making high-T_c dc SQUIDs, with appropriate properties, for this application. A further extension of the application is on-line quality evaluation, but this is still to be realised. The work that was done and reported in the previous chapters was supplemented by an investigation of the practical application of the NMR technique to internal fruit quality testing. In Chapter 6 we present the results of this investigation with both a high-field NMR and a SQUID-NMR system.

Chapter 6

NMR fruit quality measurements

NMR technology is invariably considered to be the major analytical tool for obtaining a greater understanding of food composition and the factors affecting it. It is also commonly used for authentication of food products and fruit juices [22], [128].

The measurement of internal fruit quality by NMR is mainly aimed at identifying and quantifying the metabolites contributing to the internal quality. In this chapter we investigate the high-field NMR technique as an analytical method and use it to measure the sugar content in table grapes. The NMR technique is compared to a conventional method commonly used to measure the sugar content in fruits. The sugar components were identified, quantified and compared to the conventional refractometry measurements, taken as our standard reference. A short look at the validation of the method is also reported in Section 6.3.

Furthermore, we performed a predictive non-destructive measurement of sugar content in table grapes, using a low-field SQUID-NMR system, and the results are reported in this chapter (Section 6.5) as well.

6.1 NMR measurements of sugar content in table grapes

6.1.1 Quantitative NMR (QNMR)

Targeted analysis of the NMR data proposes a number of critical points for obtaining good results. Accuracy and precision depend on the conditions of signal acquisition and processing. Some of these points are:

1. A good choice of reference standard makes the quantification of analytes easy. A good standard should be unrelated to the analyte in terms of structure, containing the targeted nucleus, and preferably with a single resonance that doesn't overlap with that of the analyte. A good standard is also preferably chemically inert, equally soluble, with low volatility and a reasonable T_1 .

2. A well chosen set of acquisition parameters guarantee the good quality of results. Such parameters are:

- A high S/N ratio (scales with the square root of the number of scans) improves precision of determination in quantification. A S/N ratio of 250 would be enough for a measured integral to fall within 1% of the true value. A minimum of 8 scans (the total number of scans is in multiples of 8) is always used to reduce hardware related mismatches.
- The detection time for the FID (acquisition time typically 1-5 sec) does not need to be longer than $3T_2$, as at this point the signal has decayed by 95% (into noise) [129].
- Related to the acquisition time are the spectral width (SW), the number of data points (NP) and the digital resolution, given respectively by $AT = \frac{NP}{2SW}$ and $DR = \frac{SW}{NP(real)}$.
- The receiver gain of the circuitry which is responsible for detecting and amplifying the signal, prior to digitization by an ADC, should be well set in order to properly fill the ADC[1].
- The time between the start of acquisition of two consecutive FIDs (repetition time) needs to be long enough to allow the magnetization to relax essentially completely (by about 99%). Such a time is of the order $5T_1$ when a pulse width of 90°is used.
- The pulse width is expressed in terms of the tip angle ($\theta = \gamma B_1 \tau$) or its duration in μs. For optimal measurement results a pulse width equivalent to 90° is preferable.

3. With regard to the sample, one should consider the sensitivity, which depends on the homogeneity[2] of the magnetic field surrounding the sample, the gyromagnetic ratio and natural abundance of nuclei and the absence of solid particles for solution samples.

4. Good data processing depends on a number of factors such as phasing, integration, Fourier transform, etc. Each of them should be performed optimally for accurate results.

6.1.2 Sample preparation

White seedless grape berries were purchased from a shop (Shoprite, Stellenbosch), transported on ice (to simulate their normal storage conditions) to the laboratory. The whole grapes were rinsed with distilled water to make sure there was no residual dirt that could affect the spectra. The berries were then detached one by one from the bunch of grapes and quickly ground by hand and kept overnight at -80°C to freeze. After being frozen, they were placed in the freeze dryer for 4 days of lyophilization. The freeze dried berries were blended into a fine powder and then kept in the desiccator to prevent them from reabsorbing moisture, until the day of the experiments.

[1] Analogue to Digital Converters used in NMR have a limited dynamic range of 16-18 bits. A low receiver gain results in a poor S/N ratio and, if too high, clips the FID, and the quantification of resonance intensity becomes incorrect.

[2] This can be adjusted by a process called shimming.

Before the berry powder could be used for NMR measurements, it had to be directly extracted in deuterated NMR solvents. The procedure was done as follows:

- A sample of 100mg of berry powder was measured and transferred to a tube of 2.5ml capacity.
- A quantity of 750μl of D_2O(KH_2PO_4 buffer, pH 6.0) containing 0.01% TMSP-d_4 and, 750μl of methanol-d_4, were added to the tube.
- The mixture above was vortexed for 1min, ultrasonicated for 20 min, and centrifuged at 10 000rpm for 10min, all at room temperature.
- An aliquot of 800μl of the supernatant was transferred to a 5mm NMR tube and used for the ^{1}H NMR experiment.

The extraction method mentioned above was chosen, as it was shown in [130] to be the best in determining sugars, especially together with the main acids present in grape berries.

Grape powder is very hygroscopic! Care should be taken when handling it not to keep it in a humid place for long, for it absorbs moisture quickly and becomes sticky. That makes it difficult to weigh for sample preparation, and increases the amount of unwanted water in the sample. It is advisable to avoid contact with light, heat, shocks due to transport, etc., for they all affect the metabolite content.

6.1.3 Conditions for experiments

After preparation of the samples they were taken to the NMR laboratory to perform the measurements. The NMR measurements were carried out under the conditions as explained below:

- The ^{1}H NMR spectra of grape berries were recorded on a 600MHz Varian spectrometer at 25°C, using the Vjnmr software. Each ^{1}H NMR spectrum consisted of 8 scans, thus 32768 complex points, requiring 45s, of which 1.707s was the acquisition time, with the following parameters: 0.292945Hz/pt, observe pulse (PW)=45° (4.55μs), and relaxation delay (RD)=1s. The observe pulse was later on updated to 90° to yield a maximum polarization. More parameters were changed in the second series of experiments (see Section 6.3.5).
- Regarding the solid state NMR, the experiments were conducted on a 600MHz VARIAN spectrometer available at Stellenbosch University. The samples, in a powder form, were packed in a 4mm NMR rotor, and loaded into the Spectrometer (magnet chamber) by means of the probe. The ^{1}H decoupled ^{13}C NMR spectra were taken in 256 scans. The tancpx pulse sequence was used for decoupling, the samples were rotated at 8000rpm and the CPMAS measurements were performed. The measurements were preceded by the optimization of the spectrum acquisition settings. Some of the parameters that were optimized are contact time, recycle delay, rotation speed and the signal to noise

ratio. A number of critical points have to be taken into account when running the ^{13}C solid state NMR experiments, namely:

- It is important to ensure that the acquisition parameters are good enough and optimized, in order to get a well resolved spectrum;
- One has to make sure that the peaks in the spectrum are not the side-bands. These are spikes that appear on the spectrum in a regular pattern with a spacing that is equal to the rotation frequency;
- The signal to noise ratio must be as high as possible. This can be enhanced by increasing the number of scans performed per sample to acquire a spectrum.

The chemical shifts were referenced to the lowest down-field peak of adamantane which is 38.4.ppm higher than the TMS one. The latter is often used as the zero reference for the chemical shifts. The deionized water can be added to the solid samples to enhance the mobility of atoms (^1H), making the spectrum better resolved, and the peaks narrower.

6.1.4 Processing of the NMR spectra

After acquisition of the spectra, the files were saved for data analysis related treatment at a later stage. FIDs thus saved were Fourier transformed by using the Gaussian mode, with LB=0.5 Hz, twice the number of complex points acquired and auto-phased. A further manual phasing was needed and then performed, and baseline corrected. All this pre-treatment was done by using the SpinWorks software (Version 3.1).

6.1.5 Visual analysis of ^1H NMR spectra

The proton NMR spectrum is shown in Fig. 6.1. The spectrum ranges from 0 to 5.5 ppm and can be divided into two parts, from 0.8 to 2.3 ppm, and from 3.15 to 5.4 ppm, which correspond to a region of aliphatic compounds (some organic acids and some amino acids) and a region predominated by carbohydrates, respectively. The region between 5.5 to 8.5 ppm, which is supposedly dominated by phenolic compounds, does not show any peaks, which is in accordance with the extraction method used (direct extraction in deuterated NMR solvents) [131].

As already known, both the height and the area below the peak is proportional to the density of nuclear spins [132]. The spectra present very high peaks in the carbohydrates region, which suggests a content high in sugars (glucose, fructose and sucrose). Very short peaks in the region of acids suggest a content low in acids.

A full spectrum, showing actual relative heights of the peaks, is given in Fig. D.1. The figure is a screenshot of the spectrum after Fourier transformation in the Spinworks software.

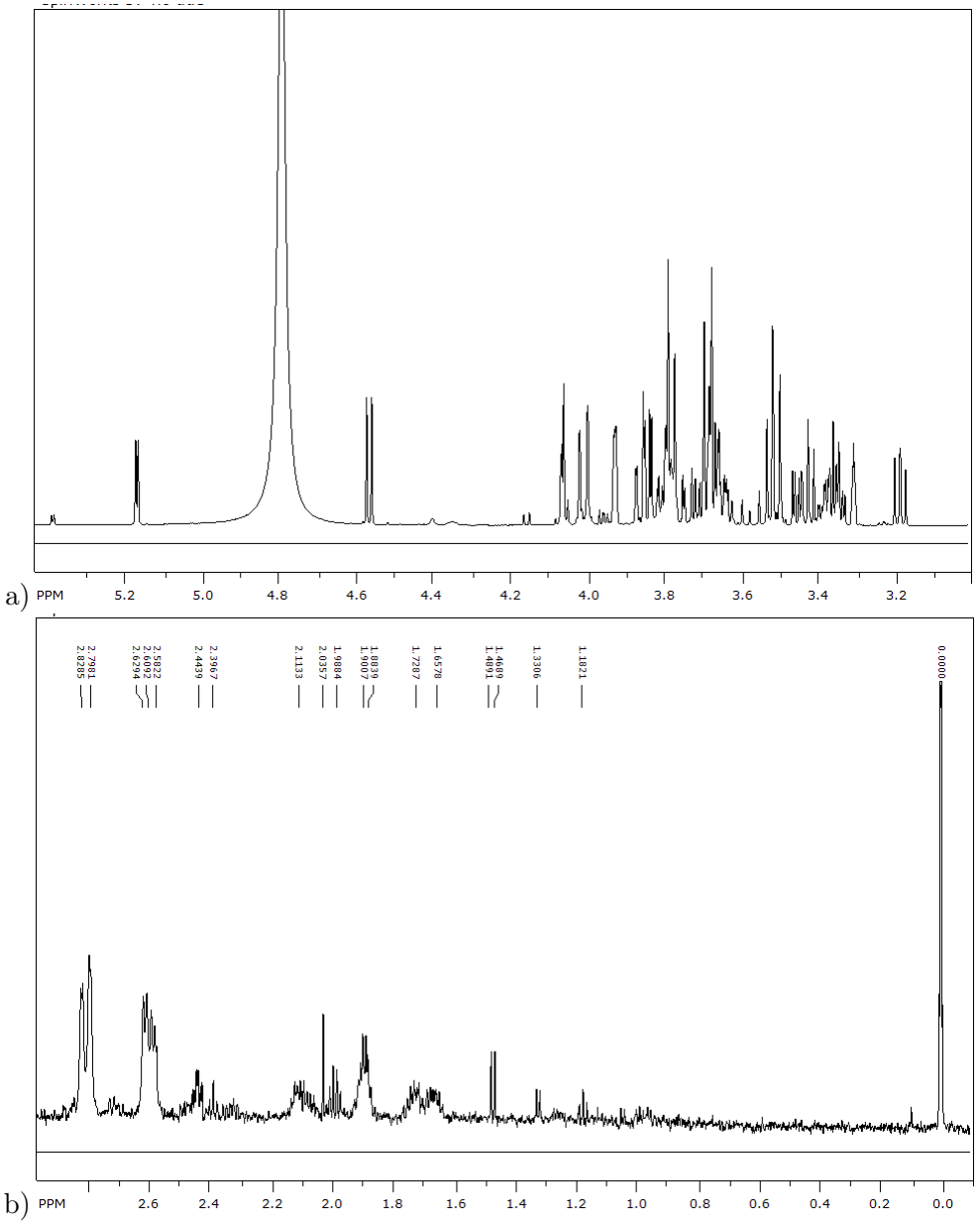

Figure 6.1: ^{1}H NMR spectrum of a grape berry: a) Predominantly sugars, b) Aliphatic components.

6.1.6 Identification of metabolites

Though NMR has many advantages in metabolomics, the identification of metabolites in samples with a high carbohydrate content, as it is in our case, remains a challenge. This is due to the fact that signals overlap. To solve this problem, one needs to carry out two dimensional experiments, such as ^{1}H-^{1}H COSY, J-resolved, HMBC and HSQC [131]. Even though our spectrum was not 100% resolved, it was good enough to allow quantification of the sugars.

The identification was performed by comparing the experimental spectra to the spectra found in the literature [133][134], [135], [136], [137], [138] and free NMR databases [139]. The identified metabolites are listed in Table 6.1.

The unidentified individual signals were counted in a targeted group, where needed (especially for carbohydrates), and left out where not needed. About 20 components were identified in the whole NMR spectrum, 17 of them being the metabolites of the fruit, and three used in the solvent mixture.

Peak	Start(ppm)	End(ppm)	Intensity(rel.)	Intensity(abs.)	Metabolite
1	4.932	4.689	0.4303	1181708	Residual water
2	5.4	5.387	0.0017	4701	Sucrose
3	5.182	5.166	0.0123	33683	Glucose
4	4.588	4.583	0.0004	1013	"
5	4.581	4.571	0.0083	22712	"
6	4.569	4.557	0.0083	22709	Glucose
7	4.523	4.518	0.0003	755	
8	4.49	4.486	0.0001	376	malate
9	4.417	4.394	0.002	5479	Tartrate
10	4.371	4.331	0.0022	6141	malate
11	4.172	4.163	0.0008	2196	Fructose
12	4.155	4.148	0.0009	2461	"
13	4.088	4.082	0.0005	1314	Glucose,Fructose,Sucrose
14	4.078	4.044	0.0217	59603	"
15	4.034	3.985	0.0276	75897	"
16	3.976	3.966	0.0012	3205	"
17	3.964	3.953	0.0017	4726	"
18	3.952	3.943	0.0012	3241	"
19	3.942	3.918	0.0222	60837	"
20	3.906	3.892	0.0006	1759	"
21	3.887	3.764	0.1143	313774	"
22	3.759	3.741	0.0069	18891	"
23	3.737	3.615	0.1101	302393	"
24	3.612	3.606	0.0003	890	"
25	3.603	3.59	0.0021	5652	"
26	3.583	3.571	0.0012	3202	"
27	3.561	3.549	0.0025	6940	"
28	3.542	3.482	0.0422	115891	"

Peak	Start(ppm)	End(ppm)	Intensity(rel.)	Intensity(abs.)	Metabolite
29	3.472	3.457	0.007	19216	"
30	3.455	3.435	0.0096	26484	"
31	3.434	3.326	0.06	164643	"
32	3.318	3.299	0.0131	35838	Methanol
33	3.296	3.29	0.0002	527	Glucose,Fructose,Sucrose
34	3.244	3.237	0.0003	825	"
35	3.234	3.224	0.0006	1752	"
36	3.221	3.211	0.0003	905	"
37	3.207	3.168	0.0161	44160	"
38	2.849	2.776	0.0025	6936	Malate
39	2.742	2.703	0.0005	1241	"
40	2.7	2.69	0.0001	274	Citrate
41	2.649	2.56	0.0026	7198	Malate+Succinate
42	2.509	2.427	0.0011	2951	Gaba
43	2.425	2.377	0.0005	1269	Proline
44	2.15	2.045	0.0014	3812	"
45	2.04	2.031	0.0002	502	"
46	2.025	1.973	0.0007	1795	"
47	1.94	1.865	0.0015	3983	GABA
48	1.775	1.626	0.0019	5231	Arginine
49	1.486	1.475	0.0002	424	Alanine
50	1.474	1.46	0.0002	502	Alanine
51	1.339	1.311	0.0003	705	Lactic acid+Treonine
52	1.2	1.159	0.0003	840	
53	1.133	1.127	0	129	
54	1.06	1.039	0.0001	357	Valine+isoleucine
55	1.012	0.95	0.0004	1226	Leucine
56	0.012	-0.009	0.0052	14405	TMSP
57	5.413	-0.009	1	2746186	

Table 6.1: ^{1}H NMR chemical shifts of grape metabolites and integral of peaks in one of the samples used in experiments. Compounds were identified by references and using 1D NMR spectra (CD_3OD-KH_2PO_4 in D_2O, pH 6.0)

Phenolic components are of key importance in determining the quality traits of grapes, wine colour, flavour and some variants of taste [131]. Phenolic components were not detected in the present experiments, due to the extraction method used. The "solid phase extraction" process can be used to enhance their detection [131], [140].

6.1.7 Quantification of total sugars

The NMR quantification (QNMR) of metabolites is a data processing procedure. It entails a number of steps, such as:

- Pre-processing of the raw data to reconstruct the spectrum (e.g. acquisition of the FID, fast Fourier transform (FFT), phasing, base-line correction).
- Estimation of the relative signal for each identified metabolite (integration of targeted signals).
- Calibration of the integrated quantities by performing the quantification scheme on a standard of known concentration [132].

Sugar content is commonly known as a good indicator in assessing ripeness [131]. The ratio sugar:acid, known as the maturity index, is of high importance in determining the internal quality of grapes.

Single or multiple peaks of sugars were identified, integrated (measure of mean peak area) and normalized over the internal standard (TMSP in this case). The latter allowed the expression of the mean peak areas in Brix-like concentration units, in order to allow a richer comparison to the measurements performed by refractometry. The refractometer measurements were taken as our conventional reference measure of the sugar content. The total sugars amounted to 96.1% of all the metabolites (see Table 6.1). Table 6.2 gives the values of the concentration of total sugars as measured by refractometry, and by high-field NMR with the QNMR process for quantification.

6.1.8 Quantification of total acids

The main organic acids in grape (tartaric, malic, citric, succinic, and lactic acids) and eight amino acids (proline, gaba, valine, leucine, isoleucine, alanine, threonine, and arginine) have also been identified, and are reported in Table 6.1. The acids in ripe table grapes account for a negligibly small percentage of the total metabolite content. The maturity is thus usually based on the sugar content. We will present only a brief outcome of the quantification of acids. The total acids were quantified by the same procedure as the sugars, and were evaluated to be 3.7% of the overall metabolites, with the organic acids accounting for 2.1%.

6.1.9 Quantification using an internal standard

The integrated intensity (I) of a resonance is proportional to both the molar concentration (C) of the corresponding analyte and the number of nuclei (N) generating it,

$$\frac{I}{N} \propto C.$$

By comparison of the analyte to a standard of known concentration, it is possible to determine the concentration of the analyte. The relationship

$$C_{an} = \frac{\frac{I_{an}}{N_{an}} \times C_{std}}{\frac{I_{std}}{N_{std}}}. \tag{6.1.1}$$

can be used, where the subscripts "std" and "an" stand for standard used, which is TMSP in our case, and analyte, respectively [141]. The ^{1}H spectrum of TMSP gives a single peak at 0.0 ppm, from the contribution of three methyl groups (N_{std}

Sample no	Powder mass(mg)	NMR TS(g/100ml)	TSS(Brix)
1	104.5	13.71	17.25
2	101.6	14.80	18.56
3	110.2	16.64	18.75
4	103.2	16.01	18.38
5	102.8	16.02	18.19
6	105.4	14.97	17.44
7	108.2	15.73	18.19
8	106.2	15.81	18
9	108.1	15.48	17.44
10	107.5	16.07	17.81
Mean	105.77	15.52	18
Stdev	2.76	0.84	0.51

Table 6.2: Total sugar concentration measured by refractometry and NMR on the same samples. The measurements were carried out on the same batch of grapes

= 9). Another peak from OH overlaps with the water peak. The singlet at 0.0 ppm also served as the reference for quantification. The N_{an} = 28, as calculated from the chemical formulas of glucose, fructose and sucrose altogether. The C_{std} was calculated from its concentration in the D_2O solution, and the C_{an} was finally expressed relative to the total mass of grape powder per sample (mg/100mg).

6.2 ^{1}H NMR vs standard measurements

The TSS refractometry, a well known and commonly used method, was chosen as an alternative method to measure the total sugars, in order to validate the results obtained from the proton NMR.

The integrated peak areas corresponding to the sugars' peaks in the NMR spectrum were expressed in terms of concentration units comparable to °Brix. The concentration of the standard (TMSP) in the solvent, was expressed in terms of g/100ml, which is similar to the definition of °Brix, and used in (6.1.1) to find the total sugar concentration from the integrated quantities.

In Figure 6.2 the values of total sugars determined by means of NMR and by refractometry, on the same samples, were plotted together.

6.3 Validation of the method

Analytical methods intended for a specific application may need to meet particular requirements to be rated as valid. These must be proved, based on objectively tested evidence. This validation is a must for non-standard methods. The NMR definitely falls into this context [142]. Through validation a number of features such as linearity, robustness, parameters of accuracy (repeatability, comparability, and measurement

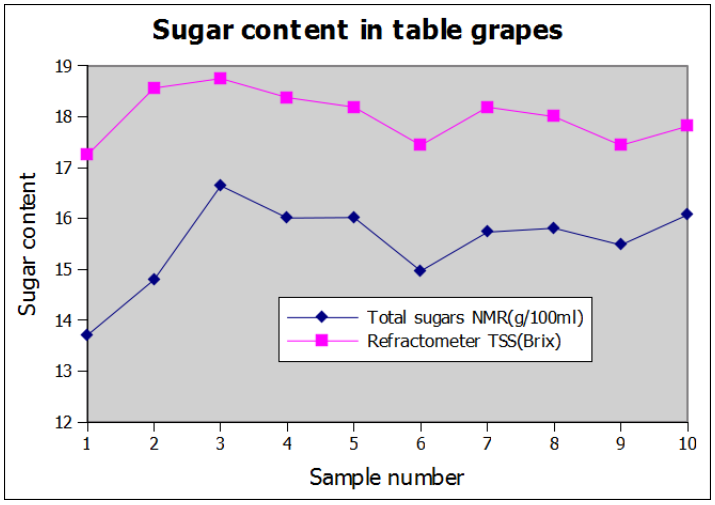

Figure 6.2: Comparison of total sugars measured by refractometry and NMR

uncertainty), etc., are examined [143]. We will limit our testing to only selectivity and specificity, linearity, accuracy, precision, repeatability and comparability.

6.3.1 Selectivity and specificity

The selectivity and specificity of QNMR are measures that estimate how reliable the measurements are in the midst of interferences (impurities or closely related compounds) [142].

Selectivity is examined by the ability to discriminate between compounds of closely related structures. From the NMR spectrum, it is noticeable that the extent of specificity of the detected components depends on the spectrometer mode used (pulse sequence, dimension of the spectrum). One can be very specific to the targeted components by using 2-dimensional spectrometry, but that is not needed within the limits of this thesis.

The specificity of NMR spectroscopy is already known for its superiority relative to many other analytical instruments in this regard. It is the ability to measure only that which it is intended [142].

The specificity also depends on the sensitivity of the nucleus detected, which is due to the fact that each detectable nucleus has a characteristic magnetogyric ratio (γ) and a fixed resonance frequency

$$\nu_r = \gamma B/2\pi. \tag{6.3.1}$$

In this case, where ^{1}H (the most sensitive of the NMR nuclei) is the targeted nucleus, the extraction method used during the sample preparation has a big influence on the components obtained upon measurement.

6.3.2 Linearity

The linearity of an analytical procedure expresses the direct proportionality of the measurement results to the amount of analyte in the sample. The test of linearity was performed by correlating the quantities determined by QNMR to those obtained by refractometry. The linear regression gave a correlation coefficient of 0.85 and a regression line $y = 2.1586x - 24.939$, where y is the value of the TSS taken with the refractometer, and x is the total sugars measured by NMR. Figure 6.3 shows the NMR values versus the refractometer values.

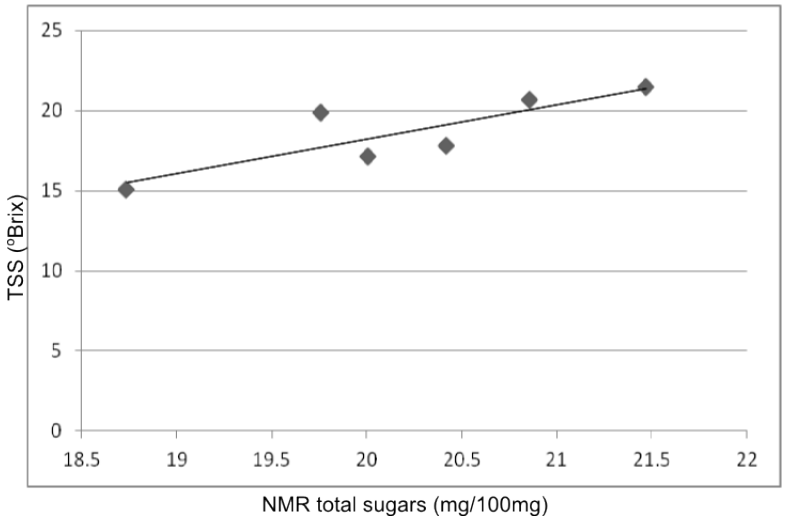

Figure 6.3: QNMR values versus TSS values by refractometry.

6.3.3 Precision

Precision is a measure of how close to each other the measured values are. The precision was determined from the measured values of concentration, as the ratio $\frac{Stdev}{C_{mean}}$, and the average precision as $\sum_i^n (Precision_i)/n$ [144]. The average precision of the NMR measurements performed here was found to be 5.34% (See Table 6.3).

6.3.4 Accuracy

The accuracy of a measurement is the measure of its closeness to the exact value. It was determined by using the relationship $\frac{C_{mean}-C_{exact}}{C_{exact}}$, and the average accuracy, by $\sum_i^n (Accuracy_i)/n$. C_{mean} (mg/100mg) represents the average of the measured total sugars per sample, and C_{exact} (°Brix), the corresponding value of the TSS obtained by refractometry. The average accuracy was found to be 9.29% (See Table 6.3).

6.3.5 Repeatability and comparability

The repeatability and comparability were performed by repeating the experiments on a different batch of samples with a defined variability (different sources: see Table 6.3) and rerunning the experiments on a different spectrometer. The measurements

that were performed to check for repeatability showed a better correlation to the reference values than the first ones (Table 6.2), and had a better spread of variability. This improvement in the results could have been due to the fact that the acquisition parameters were improved.

For the comparability check, six samples were measured on a different spectrometer (400MHz) and at a different field. The quantities determined were higher than those previously measured on a 600MHz spectrometer. This was due to shimming that was not good enough and the fact that the samples were left overnight, which could have affected the internal standard (TMSP) [129]. The spectra were less resolved than in the previous case and signals were evidently overlapping, reducing the accuracy of the measurements. The 400MHz spectrometer also had a relatively difficult shimming, and the samples had to be rotated, similar to the technique used in the solid state NMR. All these are an indication that the higher the NMR frequency (or the magnetic field), the better the results, if one decides to use the high-field NMR spectrometer.

6.4 ^{13}C NMR experiments

The resonance peaks of solid samples tend to have large line widths (about tens of kHz). This would be undetectable in the spectrum of a conventional high-resolution liquid-state NMR spectrometer. This is mainly due to the large hetero-nuclear dipolar ^{1}H and ^{13}C nuclei interaction [17].

When the samples are in a magnetic field, the orientation dependence of shielding constants, which is responsible for the distribution of chemical shifts and subsequent broadening of the observed resonances, contributes to the above mentioned problem. Another problem with solid samples is that of a short T_1 relaxation time and the fact that the ^{13}C nucleus has low sensitivity. All of these difficulties can be overcome by using the ”cross-polarization” and/or ”magic-angle spinning” (MAS) technique [145].

The carbon NMR measurements of sugar content were performed on a solid state NMR spectrometer (Varian-600MHz) available at Stellenbosch University. Solid state NMR was performed on dry grape powder, packed in a 4 mm rotor. Proton decoupled MAS (Magic Angle Spinning) experiments were performed to acquire the ^{13}C spectra of the sample. The spectrum acquisition was preceded by optimization of a number of parameters, such as the rotation speed, the acquisition time, the number of scans AND the signal-to-noise ratio, all subsequent to the probe calibration.

The acquisition of one spectrum took about 45 min, and to achieve a viable resolution of the spectrum, so that the peaks do not overlap, would require several hours of measurement.

The ^{13}C NMR was thus found to be too time consuming and cannot be used in the context treated here, within a real time frame. The spectra were not resolved,

Sample	NMR TS	NMR stdev	Conc.mean	Conc.stdev	Precision	Accuracy	TSS(Brix)	TSS stdev
400Mhz								
sb	193.46	4.75	23.32	0.57	0.02	0.13	20.7	
srg	202.28	7.14	24.38	0.86	0.04	0.37	17.8	
sw	195.51	17.07	23.57	2.06	0.09	0.18	19.9	
600Mhz								
pr	178.13	15.02	21.47	1.81	0.08	0.00	21.5	0.1
pw	155.42	5.03	18.73	0.61	0.03	0.24	15.1	0.2
sb	173.03	3.68	20.86	0.44	0.02	0.01	20.7	0.2
srg	169.38	7.22	20.42	0.87	0.04	0.15	17.8	0.0
sw	163.90	11.69	19.76	1.41	0.07	-0.01	19.9	0.1
wr	165.95	11.37	20.00	1.37	0.07	0.17	17.1	0.1
Mean			20.2061		5.34%	9.29%	18.7	0.1
Stdev			0.9463				2.4	

Table 6.3: Values of total sugar concentrations measured by refractometry and NMR on samples bought from different shops in Stellenbosch. The abbreviations are explained as follows: sb: **B**lack grapes from **S**hoprite, srg: **R**ed **g**lobe grapes from **S**hoprite, sw: **W**hite grapes from **S**hoprite, pr: **R**ed grapes from **P**ick and pay, pw: **W**hite grapes from **P**ick and pay, wr: **R**ed grapes from **W**oolworth

all the peaks were overlapping, so that neither the identification nor quantification of metabolites was possible with the spectra acquired. Figure 6.4 shows a ^{13}C NMR spectrum of a powder of a freeze dried table grape.

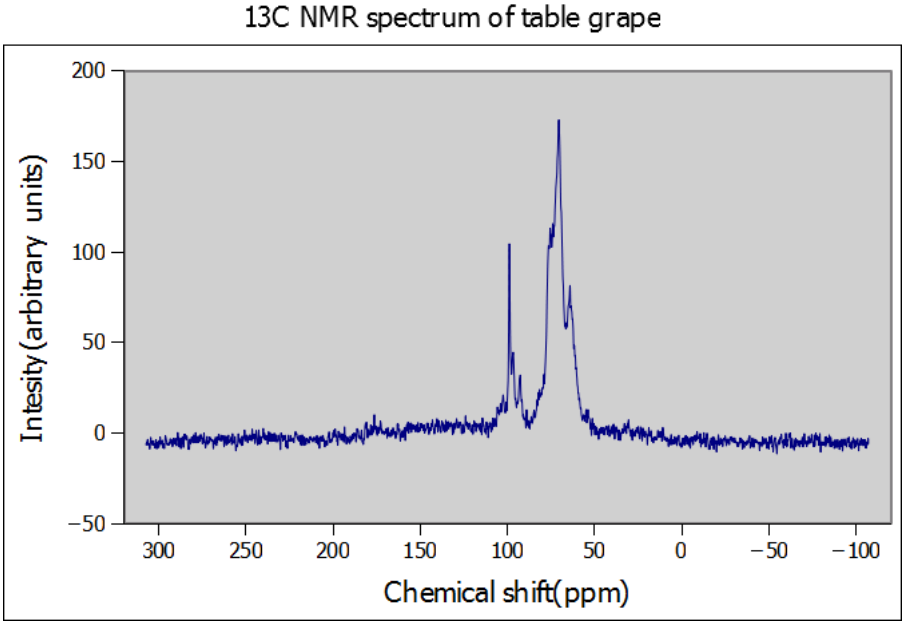

Figure 6.4: NMR ^{13}C spectrum of a table grape powder

6.5 Relaxometry measurements by SQUID-NMR

Relaxation, in terms of NMR, is perceived as how fast the spins forget the direction they were oriented in upon exposure to a magnetic field. NMR relaxometry consists of the exploitation of the relaxation times T_1 and T_2 of the spin magnetization and is commonly used in MRI applications [18], spectrometry, etc.

A SQUID-NMR spectrometer from MagQu in Taiwan (first commercial high-T_c SQUID-NMR system) was used to perform the measurements of the relaxation times on concentrations of sugar and random samples of table grapes, and the results are reported here. The low-field SQUID-NMR system used here works at a constant magnetic field of 1 *Gauss*, and is available at the Department of Electrical and Electronic Engineering at Stellenbosch University.

6.5.1 T_1 measurements

The T_1 relaxation time is a measure of the time required for the spin magnetization to regain the longitudinal component after an rf signal has been applied. It emanates from thermal interactions between resonating protons, other protons and magnetic nuclei in the lattice, and is thus called the spin-lattice relaxation time. In terms of the pulse sequence used to measure T_1, the so-called inversion recovery is commonly

used. The total magnetization is flipped by 180°, followed by a 90° pulse, before recording the FID.

Many factors influence the value of T_1 and these should be taken into account when interpreting the measured values. Some of these factors are the presence of paramagnetic substances in the sample, the NMR frequency and how close the latter is to the frequency of molecular motions [18], etc. The dilution is taken as the num-

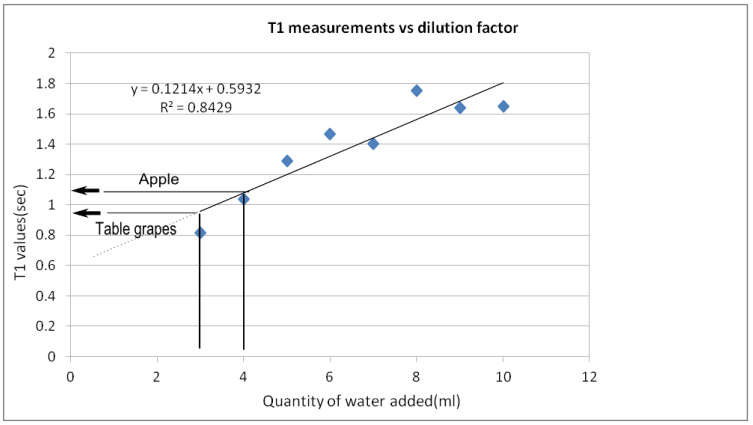

Figure 6.5: Correlation of T_1 values measured on solutions of sugar versus the dilution factor

ber of ml of water mixed with 1g of table sugar (sucrose). The trend line and the correlation coefficient show that the T_1 values increase as the sugar concentration decreases. This is exactly what is expected, as, when the concentration is decreased, the mobility of the water molecules is increased, not allowing the magnetization to relax [18], [145].

6.5.2 T_2 measurements

T_2, also called the spin-spin relaxation time, is the measure of how long the resonating protons precess in phase (remain in a coherent state) after a 90° pulse. It is less dependent on the magnetic field and only involves the phases of other nuclear spins. During the measurement, a number of evenly spaced 180° pulses follow the 90° pulse, and the decay of the whole spin echo is used to calculate the T_2 relaxation time. Figure 6.7 shows typical spectra and spin echo measured by the SQUID-NMR system.

The T_1 and T_2 variation shown in Figures 6.5 and 6.6 is quite similar, as is expected in a water solution [146]. The measured grape samples yielded the T_1 values that are around 0.95 sec. This, compared to the sugar concentrations, would suggest a closeness to the highest of the concentration ($0.25\text{g.ml}^{-1} = 25\%$) that were used. The NMR measurement results that were previously performed and reported in Table 6.3, show a sugar content that is close to 25°Brix, which is also in agreement with the literature [3]. This also confirms the possibility of direct sugar content measurement

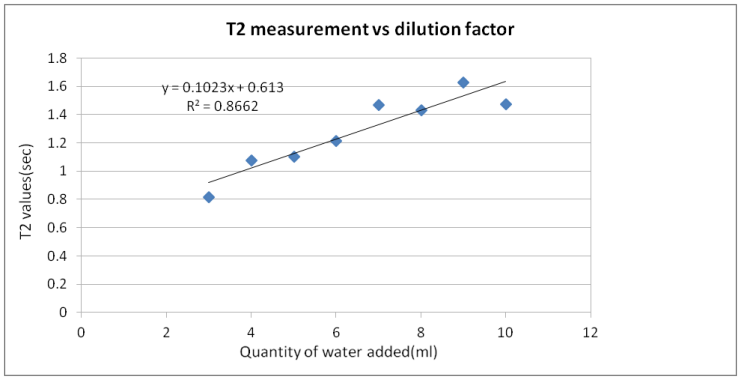

Figure 6.6: Correlation of T_2 values measured in solutions of sugar versus the dilution factor

in table grapes, using the T_1 relaxation time.

Additional measurements were performed on apples (Golden delicious), and lead to a value of $T_1 = 1.11sec$. By using the standard curve, we found a correspondence of sugar concentration of 1g:4ml (= 20%: 20°Brix), which also falls in the acceptable range for ripe apples.

The T_2 value measured on the grape samples is close to 0.78 sec, which is a bit lower, but close to the T_2 value of the highest sugar concentration used in these measurements. This suggests a value of sugar content that is a bit higher than 25°Brix, falling out of the acceptable range of °Brix in table grapes. The decision on what is the best method between T_1 and T_2 remains a subject of extensive investigation. Nevertheless, it has already been noticed that the T_1 measurement is easier to perform on this machine, in terms of spectra stability, than the T_2 measurement. Thus, we would suggest in conclusion, limited to the present system, that the T_1 could be the best way of measuring the sugar content in grapes non-destructively, using SQUID-NMR techniques.

6.6 Summary

This chapter encompasses a brief review of the QNMR as an analytical method for evaluating the internal quality of fruits. The method was practically applied to quantifying the sugars in table grapes, measured by a high-field NMR spectrometer. The ^{1}H spectra of samples of grapes in solution were processed, the sugars identified and quantified, the quantities were converted to °Brix-like units and compared to the refractometry measurements of total soluble solids. The non-destructive relaxation measurements of sugar content of table grapes by SQUID-NMR were also reported in this chapter. In conclusion, the SQUID-NMR is found to be more advantageous than the high-field NMR, due to the fact the fruits need not be destroyed, it is time saving, requires less work and it is less costly than conventional NMR machines.

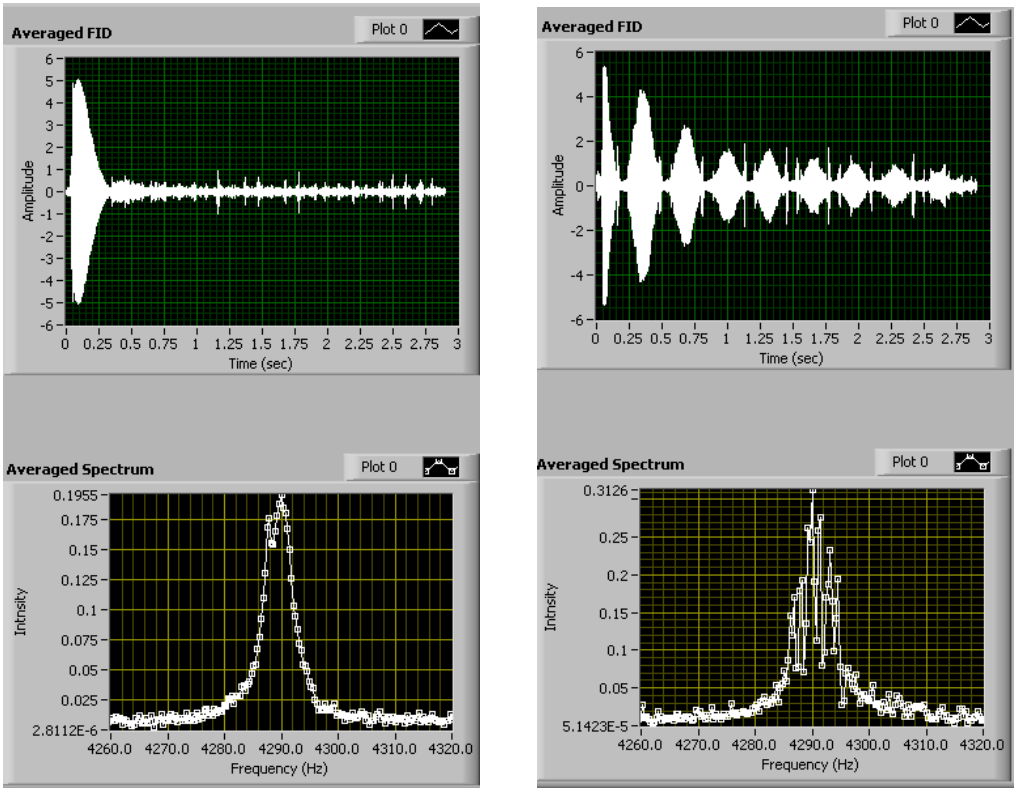

Figure 6.7: Screen capture of the FID(top) and Fourier transformed spectrum (bottom). The figure at the right shows spin echoes for the T_1 measurement.

Chapter 7

Summary and conclusions

An overview of the research presented in this thesis, highlighting the important accomplishments, and outlining the possibilities and ideas for future research, is given.

7.1 Summary of the thesis

This thesis is a compilation of the work that was done in order to attain the objectives of this project, as stated in Chapter 1. The thesis was subdivided into two parts, namely the manufacturing of a SQUID magnetometer and the investigation of NMR technology as applied to fruit quality evaluation.

NMR technology was theoretically reviewed, with some focus on low-field NMR. The concept of fruit quality evaluation was also reviewed, in order to establish standard measurements for the validation of NMR as an analytical method.

A literature review on the theory of superconductivity, Josephson junctions and the SQUID was given in Chapter 3, followed by simulations of the dynamics of the Josephson junction and of the SQUID.

The design of a SQUID, based on the theory previously reviewed, the manufacturing process with an emphasis on the double resist laser lithography method, together with the results of manufacturing and testing of the device, are reported in Chapter 4.

The applicability of the NMR technique to internal fruit quality testing was investigated by carrying out quantitative measurements of metabolites contained in table grapes. These measurements were performed using high-field NMR spectrometers.

In order to validate the NMR method, measurements of sugar content by refractometry were conducted on freshly blended fruits, before freeze-drying. The measurements of both methods were correlated afterwards.

Furthermore, a quick study of non-destructive probing of the sugar content in ta-

ble grapes was conducted on a SQUID-NMR system, by correlating the T_1 and the T_2 values measured on grapes to those measured on samples with varying sugar concentration.

7.2 Conclusions

During the manufacturing process YBCO thin films were deposited on MgO substrates, by either sputtering (ICM) or PLD techniques. The thin films were characterised by conducting susceptibility measurements to test the samples for superconductivity, X-ray diffraction for correctness of the molecular structure and AFM microscopy for surface roughness.

The deposited YBCO films had a T_c varying from 80K to 89K (with a transition width $\Delta T = 2$K (ICM) and $\Delta T = 0.25$K (PLD)), were 150nm to 220nm thick, with an average surface roughness of 8nm (ICM) and 25nm (PLD).

The films deposited by PLD were characterized as *c*-axis oriented with correct stoichiometry. Those made by sputter deposition had good XRD characteristics originally, but later showed unstable characteristics, and repeatability proved a problem. The latter XRD tests showed a non-exact structure of the films, which could suggest the presence of extra components in the film, probably causing a wrong structure of the film. The problem was solved by servicing the ICM chamber. Another problem that was encountered was a low T_c in the sputtered films, and this was solved by extending the annealing time to get enough oxygen in the YBCO films. Later films were not characterized by XRD, but had good superconducting characteristics.

The YBCO thin films were patterned into SQUID structures in two ways, conventional UV lithography followed by the AFM scratching of submicron constrictions, and by double resist laser lithography.

In the first case, the method presents the advantage of fast lithography, but fails on the scratching, which is long, and unpredictably difficult to repeat. A characterization of the scratching technique was done, in terms of the system parameters versus the depth attained, but repetition of previous results was not tangible. This was believed to be mainly due to the performance of the microscope, or the drawing accuracy of the software. A possible solution to this problem would be either to use the script facility of the software to define the tracks to be scratched, instead of drawing with a mouse pointer.

In the second case, double resist laser lithography (DRLL) was implemented as a solution to the scratching problem. The implementation of this method provided a more repeatable process and was faster to perform. The DRLL method was found to be more reliable in terms of the ease of repeatability. It offers a better possibility to make structures with much smaller dimensions, compared to UV lithography. It is also very flexible in restructuring and resizing, or even redesigning, structures. Circuits can thus be very easily improved as far as their physical features are concerned.

It is also less costly, both financially and in terms of time.

Constrictions ranging from 500nm to 1.8μm in width were obtained, and the method resulted in a working SQUID.

An interesting case was envisaged, that of combining both lithography methods, where the implementation of the junctions would be done on the laser system, and the extended circuit of the SQUID would be by UV exposure. This would significantly shorten the time required to complete the full patterning of a SQUID, where the junctions are implemented as micro/nano-bridges.

The etching process was performed by argon ion milling and resulted in well resolved structures with good square shaped side angles. No destruction of the films was noticeable by either optical microscopy or by the SEM. Nevertheless, this etching method was found to be time consuming when dealing with many samples. A wet etch process thus had to be used. In addressing the problem of underetching reiterated by previous students, a much lighter aqueous solution of citric acid than previously used, with gentle pipette blowing instead of a ultrasonic bath, was used. The etched structures were always well defined (with a maximum undercut of less than 1μm), and the superconducting properties of the film subsisted. One should be careful, however, when dealing with wet solutions and superconductors, for their properties are prone to be destructed if they are in contact for a long time, depending on how rich the film is. Contact time should thus be minimized.

The testing of the SQUID device was done in liquid nitrogen using a *Mr SQUID* system as the signal generator. A non-hysteretic current-voltage characteristic of the device was obtained. The characteristics of the tested SQUID, obtained from the measured I-V curve, were $I_c = 20\mu$A and $R_n = 5.5\Omega$. The effect of modulation of the I-V curve, under the effect of a changing magnetic field, was also observed, while a magnet was approached to and retracted from the proximity of the SQUID under test.

Destructive measurements of the sugar content in table grapes were done by refractometry in two series. The first series was done on the samples already prepared for the NMR measurements, and the second was done on the blended fruits as homogenate.

The destructive NMR measurements were performed on the basis of two different methods, solid state NMR and solution state NMR.

The solid state NMR, where the targeted nuclei was ^{13}C, resulted in an unresolved spectrum with broad peaks, and was time consuming ($\sim$45 min per sample). Therefore, neither the identification or quantification of the metabolites was possible in real-time experiments. In order to get a well resolved spectrum one would need to run a sample for several hours (e.g. overnight). This was thus not a recommendable method to use in the context here treated.

The ^{1}H solution state NMR was used on most of the samples and proved to be efficient. The spectra were better resolved, so as to allow for the identification of different metabolites in the samples, mainly the sugars. The acquisition of the spectrum took only about 25 seconds, and the signal to noise ratio reached a few thousand, with narrow peaks. The quantification of the sugars was performed subsequent to processing the spectrum. A comparison of the measurements so acquired to the ones obtained by refractometry was performed and a correlation coefficient of 0.85 was obtained. The accuracy of the NMR measurements was found to be 9.3% and the precision was 5.3%. A full identification of metabolites and a better accuracy can be achieved by proceeding from a further resolved spectrum, obtained by two dimensional spectrometry, and also by improved expertise with the NMR equipment. These results prove that the NMR technique is a good method to quantify the metabolites in table grapes specifically, and can be used for other fruits in general.

The last investigation was carried out on sugar (sucrose) concentrations and on table grapes. These measurements were conducted on a full commercial SQUID-NMR system and the aim was to quickly check the feasibility of non-destructive measurements on the internal quality of table grapes. The study was based on NMR relaxometry and the T_1 and T_2 values of increasing concentrations of sugar in water were found to decrease in a comparable way.

The values of T_1 and T_2 relaxation times of the grape samples were found to fall close to those of a sugar concentration of 25%, and by extrapolating the standard curve, the sugar content in the grape sample was found to be 23%. This concentration is in the range of ripe table grape °Brix, and that suggests that by measuring the relaxation time of an entire berry, one can predict its sugar content.

It is possible, therefore, to predict the sugar content of grapes/fruits non-destructively by using the SQUID-NMR system. As far as the present SQUID-NMR system is concerned, the T_1 relaxation time is achieved more quickly and direct prediction of ripeness can be done without further processing of the spectrum, as must be done in high-field NMR applications.

A further in-depth study of internal fruit quality can be done subsequent to establishing a database of sugar content by means of conventional measurements of °Brix. Maturity index can be predicted by measuring fruit samples at different stages of development and a lot more can be done with the SQUID-NMR system.

Lastly, it is important to note the many advantages of the low-field SQUID-NMR technique as applied to fruit quality testing. These advantages include:

- The non-destructive nature of the method; one can measure an entire fruit without having to destroy it.
- The targeted quality can be measured directly without a need of further processing of the spectrum, which is time saving.

- The T_1 measurement time is extremely short (a few minutes) compared to conventional high-field NMR spectrometers (several hours).
- The measurements are much faster to perform than other non-destructive methods such as NIR, X-ray CT, etc.
- A single spectrum can be used in convenient cases, instead of the T_1 measurement, and a much shorter measurement time (a few seconds) would be required.

Appendices

Appendix A

Lab equipment

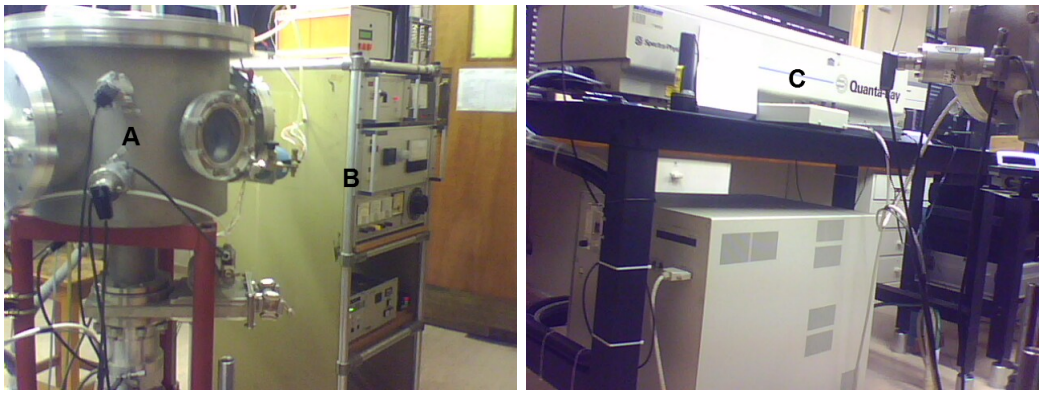

Figure A.1: PLD system and accessories: deposition chamber(A), control unit (B) and the laser unit (C)

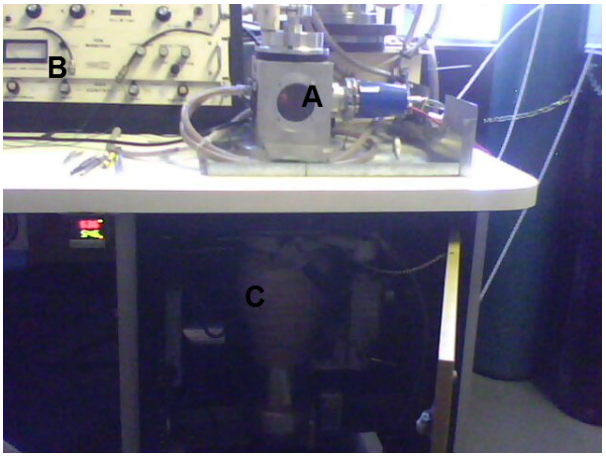

Figure A.2: The sputtering unit showing the deposition chamber (A), the control unit (B), and the vacuum pumps (C)

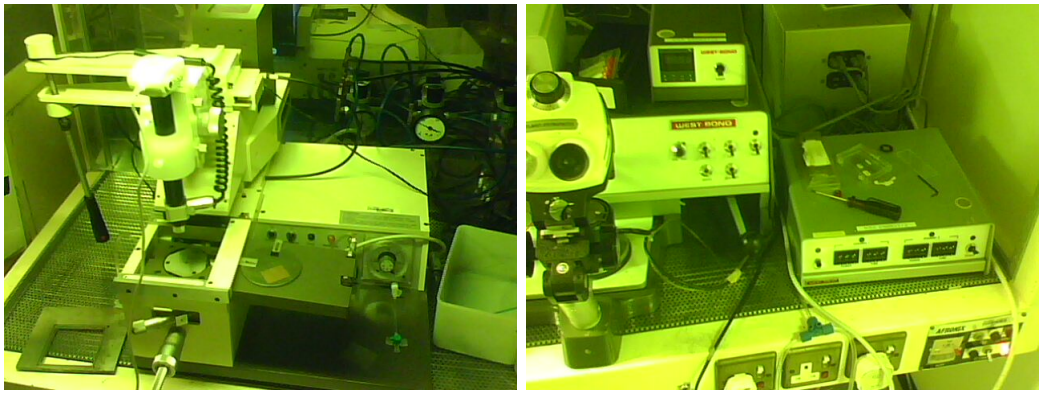

Figure A.3: The aligner system for UV photolithography (left) and the wire bonder (right).

Figure A.4: The thermal evaporator used to deposit the silver pads on the SQUID chip.

Figure A.5: Equipment for testing the SQUID: Mr. SQUID system (A), power supply (B) for an external heater of the cold finger (F) during warm up, Oscilloscope (C), cryogenic measurement system (D), computer monitor for digital display (E), vacuum pump (G) to evacuate the cold finger while cooling down with the cryogenic system (H) operated with liquid helium.

Appendix B

EMC2

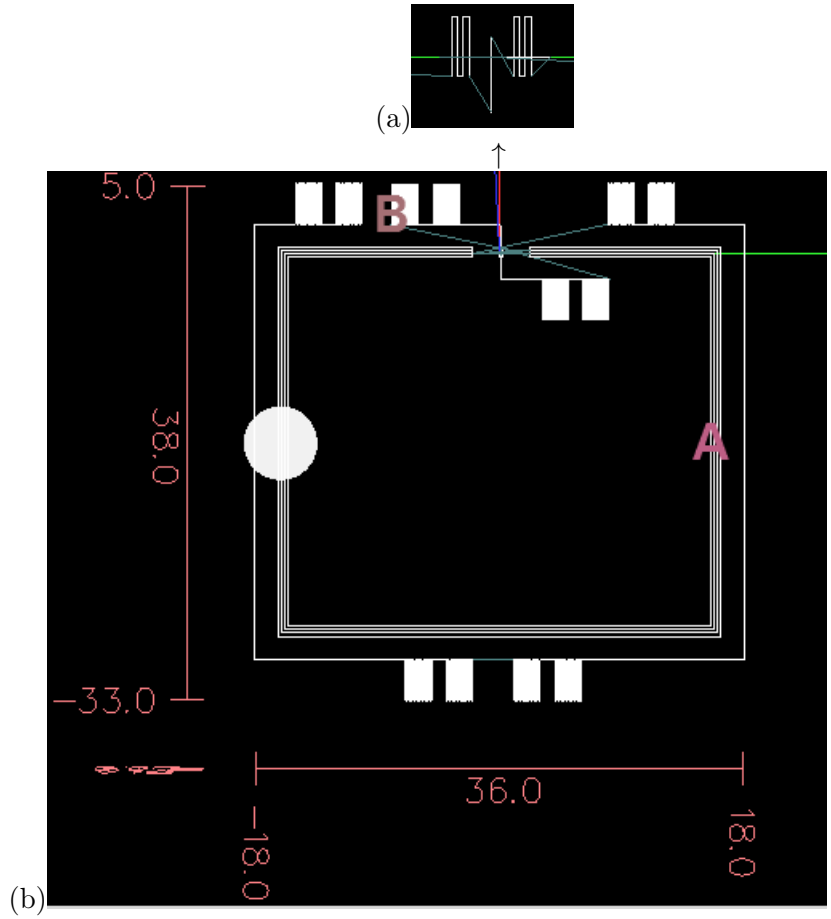

Figure B.1: SQUID chip circuitry, showing the external loop (pickup loop : A) and areas for contact pads (B)

```
G21 (Unit in mm)
G90 (Absolute distance mode)
G64 P0.01 (Exact Path 0.001 tol.)
G17
G40 (Cancel diameter comp.)
G49 (Cancel length comp.)

#1 = 0.02
#2 = 0.0
#3 = 0.0

S100 (Spindle SPEED)
F20

G0 X#1 Y-0.3 Z#3
M3

O1 REPEAT[4]
G1 X#1 Y0.3
X[#1 + 0.02] Y0.3
X[#1 + 0.02] Y-0.3
X[#1 + 0.04] Y-0.3

#1 = [#1 + 0.04]

O1 ENDREPEAT
X#1 Y0.3

M5(SPINDLE OFF)

F10

G0 X[#1 - 0.09] Y-0.3 Z0.3
M3

G1 X[#1 - 0.09] Y-2
X[#1 + 3] Y-2
```

```
#1 = [#1 + 3]

F20

O2 REPEAT[10]
X#1 Y-5 Z0.4
X[#1 + 0.1]Y-5
X[#1 + 0.1]Y-2
X[#1 + 0.2]Y-2

#1= [#1 + 0.2]
O2 ENDREPEAT

X[#1 + 1] Y-2
#1 = [#1 + 1]
O21 REPEAT[10]
X#1 Y-5
X[#1 + 0.1]Y-5
X[#1 + 0.1]Y-2
X[#1 + 0.2]Y-2

#1= [#1 + 0.2]
O21 ENDREPEAT

M5

F10

G0 X[#2 + 0.08] Y0.3 Z0.3
M3

G1 X[#2 + 0.08] Y2
X[#2 - 3] Y2
#2 = [#2 - 3]

F20
```

```
O3 REPEAT[10]
X#2 Y5 Z0.4
X[#2 - 0.1]Y5
X[#2 - 0.1]Y2
X[#2 - 0.2]Y2

#2= [#2 - 0.2]
O3 ENDREPEAT

X[#2 - 1] Y2
#2 = [#2 - 1]
O31 REPEAT[10]
X#2 Y5
X[#2 - 0.1]Y5
X[#2 - 0.1]Y2
X[#2 - 0.2]Y2

#2= [#2 - 0.2]
O31 ENDREPEAT
M5

F10

#4 = 0.0

G0 X[#4 + 2.2] Y-0.095 Z0.13
M3
G1 X[#4 - 2] Y-0.095
M5

F20

G0 X[#4 - 2] Y-0.0 Z1.0
M3
G1 X[#4 - 16] Y-0.0
X[#4 - 16] Y-28
X[#4 + 16] Y-28
```

```
X[#4 + 16] Y-0.0
X[#4 + 2.2] Y-0.0
M5
G0 X[#4 - 2] Y-0.25 Z1.0
M3
G1 X[#4 - 15.75] Y-0.25
X[#4 - 15.75] Y-27.75
X[#4 + 15.75] Y-27.75
X[#4 + 15.75] Y-0.25
X[#4 + 2.2] Y-0.25

M5

G0 X[#4 - 2] Y-0.25 Z1.0
M3
G1 X[#4 - 2] Y0.25
X[#4 - 16.25] Y0.25
X[#4 - 16.25] Y-28.25
X[#4 + 16.25] Y-28.25
X[#4 + 16.25] Y0.25
X[#4 + 2.2] Y0.25
X[#4 + 2.2] Y-0.5
X[#4 + 15.5] Y-0.5
X[#4 + 15.5] Y-27.5
X[#4 - 15.5] Y-27.5
X[#4 - 15.5] Y-0.5
X[#4 - 2] Y-0.5
X[#4 - 2] Y-0.25
M5

F20

#5 = 8

G0 X#5 Y2 Z0.6
M3
O4 REPEAT[10]
```

```
G1 X#5 Y5
X[#5 + 0.1]Y5
X[#5 + 0.1]Y2
X[#5 + 0.2]Y2

#5= [#5 + 0.2]
O4 ENDREPEAT

X[#5 + 1] Y2
#5 = [#5 + 1]
O41 REPEAT[10]
X#5 Y5
X[#5 + 0.1]Y5
X[#5 + 0.1]Y2
X[#5 + 0.2]Y2

#5= [#5 + 0.2]
O41 ENDREPEAT

F10

X[#5 + 5] Y2
X[#5 + 5] Y-30
X[#5 - 7] Y-30

F20
#5 = [#5 -7]
O5 REPEAT[10]
X#5 Y-33
X[#5 - 0.1] Y-33
X[#5 - 0.1] Y-30
X[#5 - 0.2] Y-30

#5 = [#5 - 0.2]

O5 ENDREPEAT
```

```
X[#5 - 1] Y-30
#5 = [#5 - 1]
O51 REPEAT[10]
X#5 Y-33
X[#5 - 0.1]Y-33
X[#5 - 0.1]Y-30
X[#5 - 0.2]Y-30

#5= [#5 - 0.2]
O51 ENDREPEAT

M5

G0 X[#5 - 3] Y-30
M3
#5 = [#5 - 3]
O6 REPEAT[10]
G1 X#5 Y-33
X[#5 - 0.1] Y-33
X[#5 - 0.1] Y-30
X[#5 - 0.2] Y-30

#5 = [#5 - 0.2]

O6 ENDREPEAT

X[#5 - 1] Y-30
#5 = [#5 - 1]
O61 REPEAT[10]
X#5 Y-33
X[#5 - 0.1]Y-33
X[#5 - 0.1]Y-30
X[#5 - 0.2]Y-30

#5= [#5 - 0.2]
O61 ENDREPEAT
```

```
F10

X[#5 - 11] Y-30
X[#5 - 11] Y2
X[#5 - 8] Y2

#5 = [#5 - 8]

F20

O7 REPEAT[10]
G1 X#5 Y5
X[#5 + 0.1]Y5
X[#5 + 0.1]Y2
X[#5 + 0.2]Y2

#5= [#5 + 0.2]
O7 ENDREPEAT

X[#5 + 1] Y2
#5 = [#5 + 1]
O71 REPEAT[10]
X#5 Y5
X[#5 + 0.1]Y5
X[#5 + 0.1]Y2
X[#5 + 0.2]Y2

#5= [#5 + 0.2]
O71 ENDREPEAT


M5
M2
```

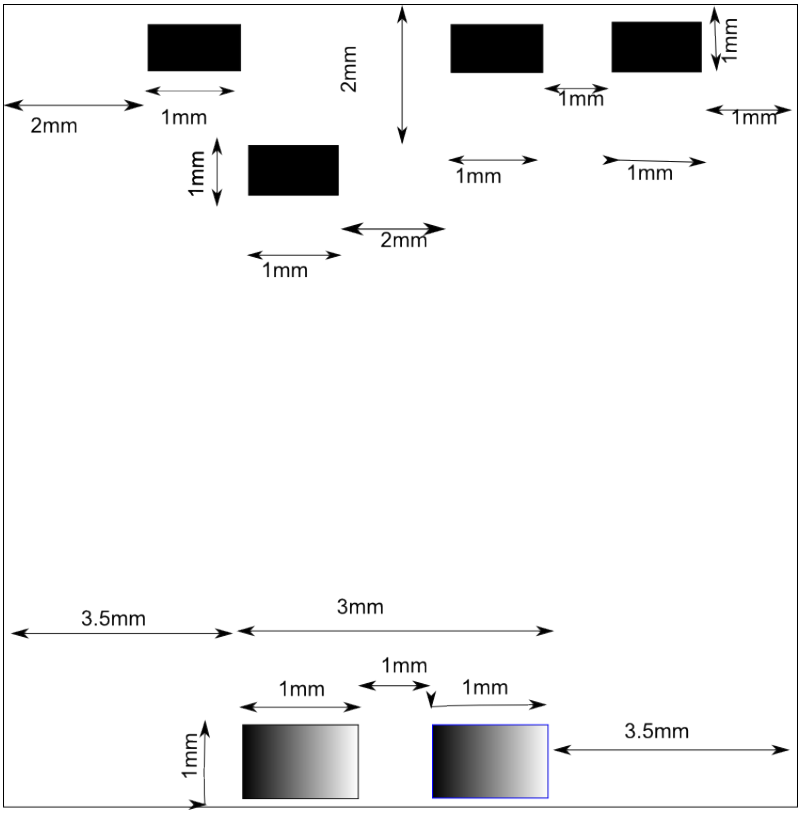

Figure B.2: Mask for the contact pads evaporation

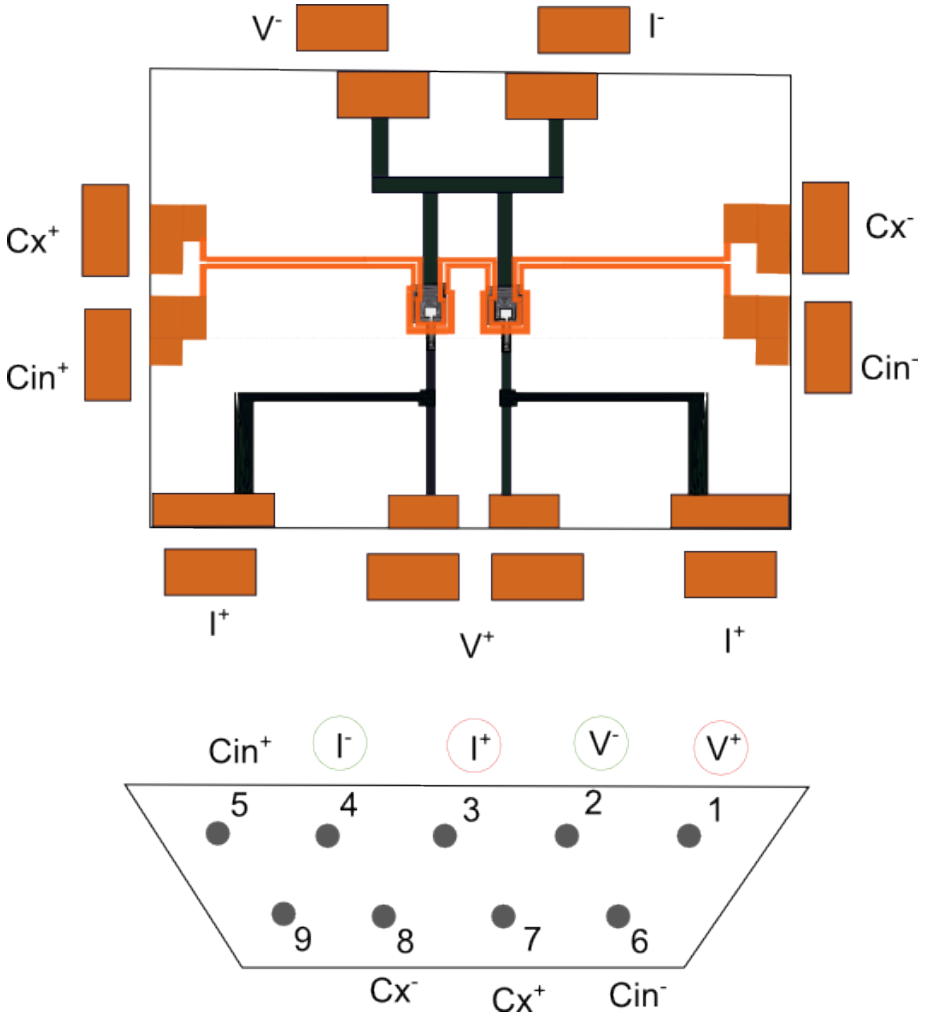

Figure B.3: The Mr. SQUID chip and circuitry adapted to test the SQUID fabricated in this project. Dimensions are not to scale.

Appendix C

Simulation codes

SIMULATIONS SCRIPT CODE

**Josephson junction circuit simulation
**_____-

**source c:\Users\Fredric\Desktop\Assing-simuls\simultsk.cir

**main circuit_____

IJ 0 2 DC=0 pwl(0 0 2n 500u 4n 0)

**sinusoidal source_____
*IJ 0 2 DC=0 pwl(0 0 1n 2m)
*Isin 0 2 sin(0 50u 2G)
_____

**voltage source_____
*VIN 2 0 pwl(0 0 1n 50m 2n 0)
*Rs 2 3 1
*vc 3 1 DC=0
_____
VC 2 1 DC=0

** Filter
Bfil 5 0 v=v(2)
Rfil 5 6 1
Cfil 6 0 3.18e-11;(c=3.5,betac<<)

**subcircuit call
XJ 1 0 4 JJS
Rshunt 1 0 1

**JJ subcircuit_____
.SUBCKT JJS 1 3 6
Isw 3 5 1
Sw 5 3 1 3 Smodel

```
**__
**Betac<<1(=0.1)
CJ 1 3 0.1638p
**Betac=4
*CJ 1 3 6.55p
**Betac>>1(=20)
*CJ 1 3 65.540p
**__
Bsw 1 3 I=V(1,3)/V(5,3)
BJOS 1 3 I=200u*sin(v(4,3)*1e4)
BPH 3 4 I=V(1,3)
CPH 4 3 3.291090p IC=0

Bphase 6 0 V=V(4,3)*1e4
Rphase 6 0 1

.MODEL Smodel SW VT=2.6m RON=26 ROFF=26;RON=10 ROFF=10
.ends
--------------------

**Analyses___

*.PRINT tran v(6)
.TRAN 400p 4n 0 0.1p
*.SAVE v(2) v(6) I(vc)
*.PROBE v(1) v(2) v(4) v(6) I(vc)
-------------
.end
---------------------------------------



**SQUID simulation
**_____-

**current of the external coil__________
ICPL 0 1 DC=0 pwl(0 0 50n 114.737u)
```

```
**coupled inductance----------
LCPL1 1 2 indmod1
LCPL2 2 3 indmod1
vc 3 0 DC=0
Bflux apl 0 v=i(vc)*sqrt(80p*103.39p)

**SQUID loop----------
IBIAS 0 a pwl(0 0 5p 20u);34u-operating point
vmeas a 5
LSQ1 6 5 indmod2
vmeas1 6 7
X1 7 0 r JJS

LSQ2 5 8 indmod2
vmeas2 8 9
X2 9 0 s JJS

**Circulating current and included flux--
BIcir 10 0 v=(i(vmeas2)-i(vmeas1))/2
Bincl 11 0 v=v(apl)+v(10)*103.39p

* Filter1
Bfil1 12 0 v=v(5)
Rfil1 12 13 1
Cfil1 13 0 9.18e-10

* Filter2
Bfil2 x 0 v=v(10)
Rfil2 x y 1
Cfil2 y 0 3.18e-10

* Filter3
Bfil3 p 0 v=v(11)
Rfil3 p q 1
Cfil3 q 0 3.18e-10

**coupling external coil to SQUID loop---
```

```
K1 LCPL1 LSQ1 1
K2 LCPL2 LSQ2 1

**Inductance model definition----------
.model indmod1 L ind=40p
.model indmod2 L ind=51.695p; for Betal=1
.model indmod3 L ind=18u

**Analyses----------
.control
tran 1p 50n .1p .5p UIC
.endc

*.SAVE v(apl) v(13) v(5) v(y) v(q)
*.PROBE v(apl) v(13) v(5) v(y) v(q)
*.PRINT tran v(13)
*.hardcopy tran.ps V(13) V(apl)
*.hardcopy tran.txt V(12) V(apl)
**Flux locked loop
*_____
Vfll 1 20 154.15u
Eamp 21 0 20 0 450
Rint 21 22 100
Cint 22 23 20p
Eint 23 0 22 0 1e40
Rfb 23 24 294.47k
Lfb1 24 25 indmod3
Lfb2 25 0 indmod3
K3 Lfb1 LSQ1 1
K4 Lfb2 LSQ2 1
.END
```

Appendix D

Pulse sequences

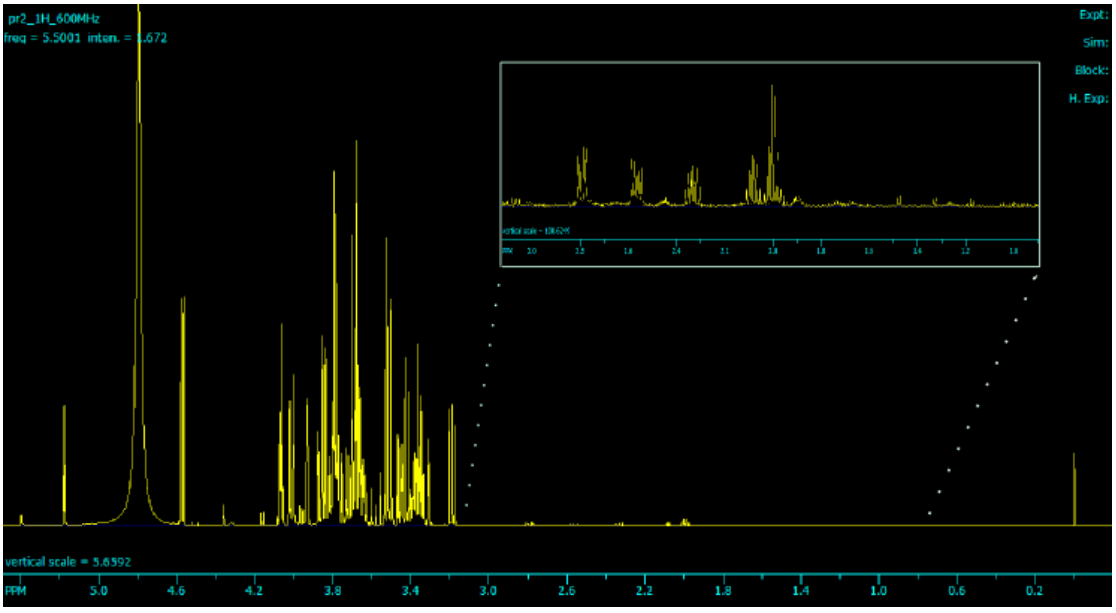

Figure D.1: Full ^{1}H NMR spectrum of a table grape.

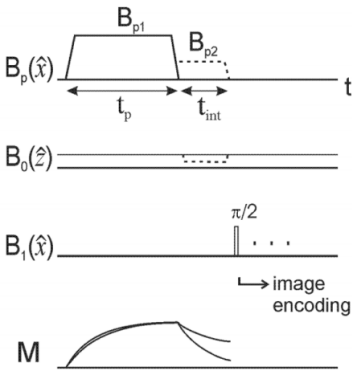

Figure D.2: An example of pulse sequence used for measuring the T_1 relaxation time [8]

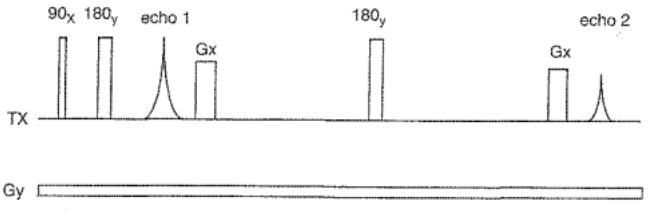

Figure D.3: Single-shot pulse sequence on-line determination of sugar content in fruit [24].

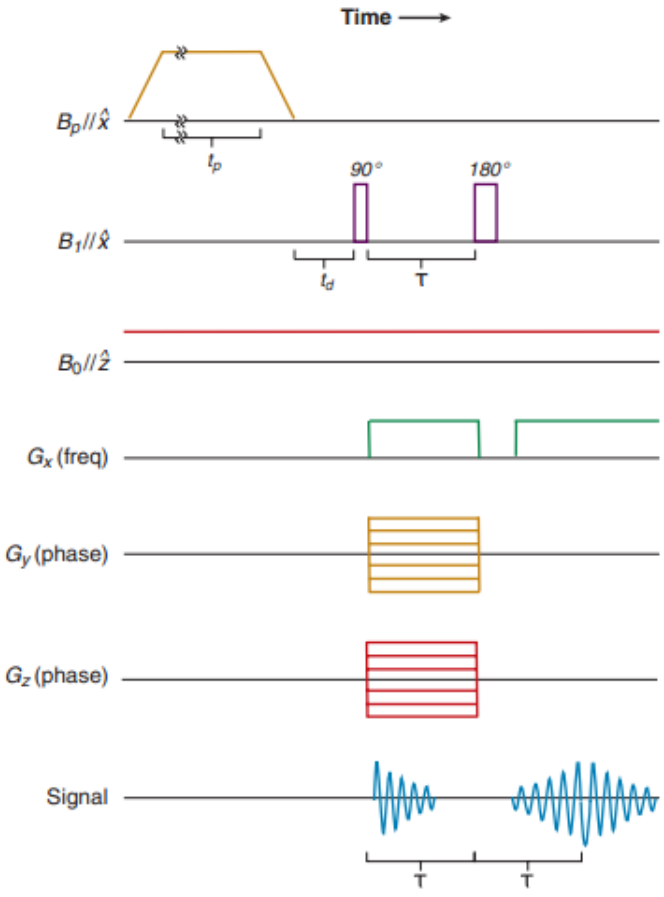

Figure D.4: Pulse sequence used in three dimensional imaging (extracted from [8])

List of References

[1] D. C. Slaughter, "Non-destructive maturity assessment methods for mango," *University of California, Davis*, pp. 1 – 18, 2009.

[2] M. Ruiz-Altisent et al., "Sensors for product characterization and quality of specialty crops - A review," *Computers and Electronics in Agriculture*, vol. 74, pp. 176 – 194, 2010.

[3] D. Van Zyl, "SQUID detected low-field NMR for the evaluation of internal fruit quality," Master's thesis, University of Stellenbosch, 2010.

[4] B. Hills and C. Clark, "Quality assessment of horticultural products by NMR," *Annual reports on NMR spectroscopy*, pp. 75–120, 2003.

[5] B. M. N. et al., "Non-destructive evaluation: Detection of external and internal attributes frequently associated with quality and damage," *Postharvest Handling: A Systems Approach*, pp. 421 – 441, 2009.

[6] A. Constantinesco et al., "Low-field dedicated and desktop magnetic resonance imaging systems for agricultural and food applications," *Magnetic Resonance in Chemistry*, vol. 35, pp. 69 – 75, 1997.

[7] T. Haishi, T. Uematsu, Y. Matsuda, and K. Kose, "Development of a 1.0 T MR microscope using a Nd-Fe-B permanent magnet," *Magnetic Resonance Imaging*, vol. 19, pp. 875 – 880, 2001.

[8] J. Clarke, M. Hatridge, and M. Möβle, "SQUID-detected magnetic resonance imaging in microtesla fields," *Annual Review of Biomedical Engineering*, vol. 9, pp. 389 – 413, 2007.

[9] A. N. Matlachov, P. L. Volegov, M. A. Espy, J. S. George, and R. H. Kraus, "SQUID detected NMR in microtesla magnetic fields," *Journal of Magnetic Resonance*, vol. 170, pp. 1 – 7, 2004.

[10] J. Chudek and G. Hunter, "Magnetic resonance imaging of plants," *Prog. Nucl. Magn. Reson. Spectrosc.*, vol. 31, 1997.

[11] R. Verel, "Solid-state nmr spectroscopy - An introduction," 2010.

[12] T. H. Huang, "Introductory to NMR spectroscopy."

[13] Griffiths, *Introduction to Quantum Mechanics*. Prentice Hall Inc., 1995.

[14] M. Levitt, *Spin Dynamics: Basics of Nuclear Magnetic Resonance*. John Wiley & Sons, 2001.

[15] J. Keeler, *Understanding NMR Spectroscopy*. John Wiley & Sons, 2005.

[16] M. Duer, *Introduction to solid-state NMR.* Blackwell Science Ltd (Oxford), 2004.

[17] S. Causemann, "Introduction to solid state NMR spectroscopy," Solid State NMR workshop: CAF Stellenbosch University, 2011.

[18] W. G. Bradley, "Fundamentals of MRI: PartII."

[19] Radical, *Nuclear Magnetic Resonance Spectroscopy (NMR).*

[20] J.Baugh, "Introduction to NMR and NMR QIP," *Institute for quantum computing, Summer School*, 2009.

[21] A. C. o. Excellence, "Teacher notes on NMR spectroscopy."

[22] I. naki Berregi, G. del Campo, R. Caracena, and J. I. Miranda, "Quantitative determination of formic acid in apple juices by ^{1}H NMR spectrometry," *Talanta*, vol. 72, pp. 1049 – 1053, 2007.

[23] R. K. W. Buckel, *Superconductivity Fundamentals and Applications.* Wiley, 2000.

[24] B. Hills, "Applications of low-field NMR to food science," *Annual Reports on NMR Spectroscopy*, vol. 58, pp. 177 – 230, 2006.

[25] S.-M. Kim, P. Chen, M. J. McCarthy, and B. Zion, "Fruit internal quality evaluation using on-line nuclear magnetic resonance sensors," *J. agric. Engng Res.*, vol. 74, pp. 293 – 301, 1999.

[26] K. Miyamoto, M. Kuwauchi, and T. Fukuda, "Classification of high acid fruits by partial least squares using the near infrared transmittance spectra of intact Satsuma mandarins," *J. Near Infrared Spectrosc.*, vol. 6, pp. 267–271, 1997.

[27] C. Y. Wang and P. C. Wang, "Non-destructive detection of core breakdown in Bartlett pears with nuclear magnetic resonance imaging," *Hortic. Sci.*, vol. 24, pp. 106 – 109, 1989.

[28] S. Y. Wang, P. C. Wang, and M. Faust, "Non-destructive detection of watercore in apple with nuclear magnetic resonance imaging," *Scientia Horticulturae*, vol. 35, pp. 227 – 234, 1988.

[29] P. Chen, M. J. McCarthy, and R. Kauten, "NMR for internal quality evaluation of fruits and vegetables," *Transactions of the ASAE*, vol. 32, pp. 1747 – 1753, 1989.

[30] N. Ishida, M. Koizumi, and H. Kano, "The NMR microscope: a unique and promising tool for plant science," *Annals of Botany*, vol. 86, pp. 259–278, March 2000.

[31] B. Manz et al., "A mobile one-sided NMR sensor with a homogeneous magnetic field: The NMR-MOLE," *Journal of Magnetic Resonance*, vol. 183, pp. 25 – 31, 2006.

[32] B. Blümich, J. Perlo, and F. Casanova, "Mobile single-sided NMR," *Progress in Nuclear Magnetic Resonance Spectroscopy*, vol. 52, pp. 197 – 269, 2008.

[33] B. P. Hills, K. M. Wright, and D. G. Gillies, "A low-field, low-cost Halbach magnet array for open-access NMR," *Journal of Magnetic Resonance*, vol. 175, pp. 336 – 339, 2005.

[34] M. Koizumi et al., "A dedicated MRI for food science and agriculture," *Food Sci. Technol. Res.*, vol. 14, no. 1, pp. 74 – 82, 2008.

[35] G. Gamble, "Non-invasive determination of freezing effects in blueberry fruit tissue by magnetic resonance imaging," *J. Food Sci.*, vol. 59, pp. 571 – 573, 1994.

[36] S. M. Glidewell, B. Williamson, B. A. Goodman, J. A. Chudek, and G. Hunter, "An NMR microscopic study of grape (Vitis vinifera L.)," *Protoplasma*, vol. 198, pp. 27 – 35, 1997.

[37] Goodman et al., "Beta-arrestin acts as a clathrin adaptor in endocytosis of the beta2-adrenergic receptor," *Nature*, vol. 383, pp. 447 – 450, 1996.

[38] J. M. Pope, D. Jonas, and R. R. Walker, "Applications of NMR micro-imaging to the study of water, lipid, and carbohydrate distribution in grape berries," *Protoplasma*, vol. 173, pp. 177 – 186, 1993.

[39] J. L. Maas and M. J. Line, "Nuclear magnetic resonance microimaging of strawberry flower buds and fruit," *Acta Hort Science*, vol. 30, pp. 1090 – 1096, 1995.

[40] N. Ishida, H. Ogawa, M. Koizumi, and H. Kano, "Ontogenetic changes of the water status and accumulated soluble compounds in growing cherry fruits studied by NMR imaging," *Magnetic Resonance in Chemistry*, vol. 35, pp. 22 – 28, 1997.

[41] S. Cho, R. Stroshine, I. Baianu, and G. Krutz, "Nondestructive sugar measurement of intact fruit using spin-spin relaxation times (T_2) measurements by pulsed ^1H magnetic resonance," *Trans. ASAE*, vol. 36, pp. 1217 – 1221, 1993.

[42] N. Ishida, H. Ogawa, M. Koizumi, and H. Kano, "In vivo NMR in agricultural and food sciences: (non-destructive estimation of quality of foods and agricultural products by NMR)," *J. Magn. Reson. Anal*, vol. 43, pp. 103 – 109, 1996.

[43] B. Zion, M. J. McCarthy, and P. Chen, "Real-time detection of pits in processed cherries by magnetic resonance projections," *Lebensm. Wiss. U. Technol.*, vol. 27, pp. 457 – 462, 1994.

[44] B. Zion, S. M. Kim, M. J. McCarthy, and P. Chen, "Detection of pits in olives under motion by nuclear magnetic resonance," *J. Sci. Food Agric.*, vol. 75, pp. 496 – 502, 1997.

[45] B. Zion, P. Chen, and M. J. McCarthy, "Nondestructive quality evaluation of fresh prunes by NMR spectroscopy," *J. Sci. Food Agric.*, vol. 67, pp. 423 – 429, 1995.

[46] M. P. Williamson, "Thestructure andfunction of proline-rich regions in proteins," *Biochemical Journal*, vol. 297, pp. 249 – 260, 1994.

[47] M. McCarthy, B. Zion, and P. Chen, "Diamagnetic susceptibility changes in apple tissue after bruising," *J. Sci. Food Agric.*, vol. 67, pp. 13 – 20, 1995.

[48] J. J. Gonzalez, R. C. Valle, S. Bobroff, W. V. Biasi, E. J. Mitcham, and M. J. McCarthy, "Detection and monitoring of internal browning development in Fuji apples using MRI," *Postharvest Biology and Technology*, vol. 22, pp. 179 – 188, 2001.

[49] K. H. Jung, R. Stroshine, P. Cornillon, and P. M. Hirst, "Low field proton magnetic resonance sensing of water core and internal browning in whole apples," *ASAE Annual international meeting*, no. 986020, p. 20, 1998.

[50] J. B. Golding, V. Sarafis, S. Crozier, and S. E. Rose, "Nuclear magnetic resonance imaging of superficial scald in granny smith apples," *Hortscience*, vol. 32, pp. 112 – 113, 1997.

[51] C. Clark, J. MacFall, and R. Bieleski, "Loss of watercore from Fuji apple observed by magnetic resonance imaging," *Scientia Hort.*, vol. 73, pp. 213–227, 1998.

[52] K. Keener, R. L. Stroshine, and J. A. Nyenhuis, "Evaluation of low field (5.40MHz) proton magnetic resonance measurements of D_w and T_2 as methods of nondestructive quality evaluation of apples," *Journal of the American Society for Horticultural Science*, vol. 124, pp. 289 – 295, 1999.

[53] K. M. Keener, R. L. Stroshine, and J. A. Nyenhuis, "Proton magnetic resonance measurement of self-diffusion coefficient of water in sucrose solutions, citric acid solutions, fruit juices, and apple tissue," *Transactions of the ASABE*, vol. 40, pp. 1633 – 1641, 1997.

[54] P. Barreiro, A. Moya, E. Correa, M. Ruiz-Altisent, M. Fernàndez-Valle, A. Peirs, K. M. Wright, and B. P. Hills, "Prospects for the rapid detection of mealiness in apples by nondestructive NMR relaxometry," *Applied Magnetic Resonance*, vol. 22, pp. 387 – 400, 2002.

[55] P. Chen, M. J. McCarthy, R. Kauten, Y. Sarig, and S. Han, "Maturity evaluation of avocados by NMR methods," *Journal of Agricultural Engineering Res.*, vol. 55, pp. 177 – 187, 1993.

[56] P. Chen, M. McCarthy, S.-M. Kim, and B. Zion, "Development of a high-speed NMR technique for sensing maturity in avocados," *Trans ASAE (Am. Soc. Agric. Eng.)*, vol. 39, pp. 2205 – 2209, 1996.

[57] R. Stroshine, W. Wai, and G. Krutz, "Non-destructive ripeness sensing of intact avocado, nectarine and orange using proton magnetic resonance," *ASAE*, no. 93 - 6535, 1993.

[58] A. Raffo, R. Gianferri, R. Barbieri, and E. Brosio, "Ripening of banana fruit monitored by water relaxation and diffusion ^{1}H-NMR measurements," *Food Chemistry*, vol. 89, pp. 149–158, 2005.

[59] M. T. M. noz Barrio and C. Merodio, "Magnetic resonance imaging: a non-destructive approach to ripening state in fruits," *Acta Hort.*, vol. 463, pp. 385 – 390, 1997.

[60] N. Jagannathan, V. Govindaraju, and P. Raghunathan, "In-vivo magnetic resonance study of the histochemistry of coconut(Cocos nucifera)," *Magnetic Resonance Imaging*, vol. 13, no. 6, pp. 885 – 892, 1995.

[61] T. Yantarasri, J. Sornsrivichai, and P. Chen, "X-ray and NMR for nondestructive internal quality evaluation of durian and mangosteen fruits," *Acta hort.*, vol. 464, pp. 97 – 102, 1998.

[62] S. M. Kim, M. McCarthy, and P. Chen, "Development of a real time on line magnetic resonance sensor for fruit sorting," *CIGR*, vol. 98, 1998.

[63] J. S. MacFall and G. A. Johnson, "The architecture of plant vasculature and transport as seen with magnetic resonance microscopy," *Canadian Journal of Botany*, vol. 72, pp. 1561 – 1573, 1994.

[64] C. A. Eustace and R. B. Jordan, "Sugar content evaluation using earth's field proton magnetic resonance," *Transactions of the ASABE*, vol. 38, no. 5, pp. 1563 – 1571, 1995.

[65] C. J. Clark, L. N. Drummond, and J. S. MacFall, "Quantitative NMR imaging of kiwifruit (Actinidia deliciosa) during growth and ripening," *J. Sci. Food Agric.*, vol. 78, pp. 349 – 358, 1998.

[66] C. J. Clark, A. C. Richardson, and K. B. Marsh, "Quantitative magnetic resonance imaging of Satsuma mandarin fruit during growth," *Hort. Sci.*, vol. 34, no. 6, pp. 1071–1075, 1999.

[67] C. J. Clark, P. D. Hockings, D. C. Joyce, and R. A. Mazucco, "Application of magnetic resonance imaging to pre and post-harvest studies of fruits and vegetables," *Postharvest Biol. Technol.*, vol. 11, no. 1, pp. 1 – 21, 1997.

[68] D. C. Joyce, P. D. Hockings, R. A. Mazucco, A. J. Shorter, and I. M. Brereton, "Heat treatment injury of mango fruit revealed by non-destructive magnetic resonance imaging," *Postharv. Biol. and Tech.*, vol. 3, pp. 305 – 311, 1993.

[69] L. D. Hall, S. D. Evans, and K. P. Nott, "Measurement of textural changes of food by MRI relaxometry - dependence on concentration, molecular weight and structure," *Magnetic Resonance Imaging*, vol. 16, no. 5, pp. 485 – 492, 1998.

[70] S. I. Cho, V. Bellon, T. Eads, R. Stroshine, and G. Krutz, "Sugar content measurement in fruit tissue using water peak suppression in high resolution ^{1}H magnetic resonance," *Journal of Food Science*, vol. 56, no. 4, pp. 1091 – 1094, 1991.

[71] L. Sonego, R. Ben-Arie, J. Raynal, and J. C. Pech, "Biochemical and physical evaluation of textural characteristics of nectarines exhibiting woolly breakdown: NMR imaging, X-ray computed tomography and pectin composition," *Postharvest Biol. Technol.*, vol. 5, no. 3, pp. 187 – 198, 1995.

[72] P. Barreiro, C. Ortiz, M. Ruiz-Altisent, J. Ruiz-Cabello, M. E. Fernández-Valle, I. Recasens, and M. Asensio, "Mealiness assessment in apples and peaches using MRI techniques," *Magnetic Resonance Imaging*, vol. 17, pp. 275 – 281, 2000.

[73] C. J. Clark and J. S. MacFall, "Magnetic resonance imaging of persimmon fruit (Diospyros kaki) during storage at low temperature and under modified atmosphere," *Postharvest Biology and Technology*, vol. 9, pp. 97 – 108, 1996.

[74] T. Yantarasri and J. Sornsrivichai, "Internal quality evaluation of tangerines in northern Thailand," *Acta Hort.*, vol. 464, pp. 494–494, 1998.

[75] K. Saito, T. Miki, S. Hayashi, H. Kajikawa, M. Shimada, Y. Kawate, T. NishizawaS, D. Ikegaya, N. Kimura, K. Takabatake, N. Sugiura, , and M. Suzuki, "Application of magnetic resonance imaging to non-destructive void detection in watermelon," *Cryogennics*, vol. 36, pp. 1027 – 1031, 1996.

[76] C. Y. Wang and P. C. Wang, "Differences in nuclear magnetic resonance images between chilled and non-chilled Zucchini squash," *Environ. Expt. Bot.*, vol. 32, pp. 213 – 219, 1992.

[77] T. Naruke, S. Oshita, S. Kuroki, Y. Seo, Y. Kawagoe, and J. H. Walton, "T_1 relaxation time and other properties of cucumber in relation to chilling injury," *Acta Hort.*, vol. 599, pp. 265 – 271, 2003.

[78] H. C. W. Donker, H. V. As, H. J. Snijder, and H. T. Edzes, "Quantitative ^{1}H-NMR imaging of water in white button mushrooms (Agaricus bi-sporus)," *Magn. Reson. Imag.*, vol. 15, pp. 113 – 121, 1997.

[79] P. C. Wang, H. F. Song, and Z. J. Yan, "Detection of hollow heart and brown center of potatoes by nmr," *Proceedings of the 35th Experimental NMR Conference, Pacific Grove, CA*, 1994.

[80] A. K. Thybo, H. J. Andersen, A. H. Karlsson, S. D⊘nstrup, and H. St⊘dkilde-J⊘rgensen, "Low-field NMR relaxation and NMR-imaging as tools in differentiation between potato sample and determination of dry matter content in potatoes," *Journal of Food Science*, vol. 36, pp. 315 – 322, 2003.

[81] A. K. Thybo, I. E. Bechmann, M. Martens, and S. B. Engelsen, "Prediction of sensory texture of cooked potatoes using uniaxial compression, near infrared spectroscopy and low field ^{1}H-NMR spectroscopy," *Lebensmittel-Wissenschaft und-Technologie*, vol. 33, pp. 103 – 111, 2000.

[82] A. K. Snijder, S. M. Glidewell, and B. A. Goodman, "NMR microimaging of healthy and diseased potato tubers," *Int. conf. reson.microscopy, Wurzburg, Germany*, 1995.

[83] N. Ishida, M. Koizumi, and H. Kano, "Ontogenetic changes in water in cherry tomato fruits measured by nuclear magnetic resonance imaging," *Scientia Horticulturae*, vol. 57, pp. 335 – 346, 1994.

[84] H. T. Edzes, D. van Dusschoten, and H. V. As, "Quantitative T_2 imaging of plant tissues by means of multi-echo MRI microscopy," *Magn. Reson. Imag.*, vol. 16, pp. 185 – 196, 1998.

[85] M. E. Saltveit, "Determining tomato fruit maturity with non-destructive in vivo nuclear magnetic resonance imaging," *Postharvest Biology and Technology*, vol. 1, pp. 153 – 159, 1991.

[86] N. Ishida, T. Kobayashi, M. Koizumi, and H. Kano, "^{1}H-NMR imaging of tomato fruits," *Agricultural and Biological Chemistry*, vol. 53, pp. 2363 – 2367, 1989.

[87] S. Kim, M. J. McCarthy, and P. Chen, "Feasibility of tomato quality grading and sorting using magnetic resonance," *ASAE Winter Meeting, Atlanta, GA*, vol. 94, pp. 13 – 16, 1994.

[88] C. Kittel, *Introduction to Solid State Physics*, 7th ed. John Wiley & Sons, 1996.

[89] G. B. Peacock, I. Gameson, and P. P. Edwards, "Bulk synthesis of the 135K superconductor $HgBa_2Ca_2Cu_30_{8+\delta}$," *Advanced Materials*, vol. 9, no. 3, pp. 248 – 251, 1997.

[90] J. SU, "Fabrication and characterization of mercurocuprate superconductors on silver substrates," Ph.D. dissertation, The Florida State University college of engineering, March 2004.

[91] W. A. Burger, "The design and analysis of a DC SQUID for a SQUID microscope," Master's thesis, University of Stellenbosch, December 2008.

[92] W. J. Perold, "Quantum electronics," Course Notes, 2011.

[93] T. P. Orlando and K. A. Delin, *Fundations of applied supercondictivity.* Addison Wesley, 1990.

[94] J. Axnäs, "Superconducting fluctuations in the magnetoconductivity of $YBa_2Cu_3O_{7-\delta}$ and other high-temperature superconductors," Ph.D. dissertation, Stokholm Royal Institute of Technology, March 2000.

[95] H. A. C. d. Villiers, "A process of the manufacture of the high temperature bi-epitaxial josephson junctions," Masters Thesis, University of Stellenbosch, March 2007.

[96] K. K. Likharev, *Dynamics of Josephson Junctions and Circuits.* Gordon and Breach Science Publishers, 1991.

[97] F. W. Graser, "A reproducible design and manufacturing process for SQUID magnetometers," Master's thesis, University of Stellenbosch, 2005.

[98] T. Z. Y. Hu, "Simulation research of DC SQUID composed of josephson junctions and intrinsic josephson junction arrays," *College of Information Technology Science*, 2008.

[99] Y. S. Greenberg, "Applications of superconducting quantum interference devices to nuclear magnetic resonance," *Reviews of Modern Physics*, vol. 70, no. 1, pp. 175 – 201, 1998.

[100] J. Pleikies, O. Usenko, G. Frossati, and J. Flokstra, "Optimization of a low-tc DC SQUID amplifier with tightly coupled input coils," *IEEE Transactions on Applied Superconductivity*, vol. 19, no. 3, pp. 199 – 205, June 2009.

[101] C. D. Tesche and J. Clarke, "DC SQUID: Noise and optimization," *Journal of Low Temperature physics*, vol. 29, pp. 301 – 331, 1977.

[102] A. A. Elkaseh, "Fabrication of josephson junctions using AFM nanolithography," Ph.D. dissertation, University of Stellenbosch, 12 2010.

[103] V. d. Waal, T. M. Klapwijk, and P. v. d. Hamer, "High-performance DC SQUIDs with submicrometer niobium josephson junctions," *Journal of Low Temperature Physics*, vol. 53, pp. 287–312, 1983.

[104] J. F. I. Nturambirwe, "Superconducting quantum interference device (SQUID) magnetometers: Principles, fabrication and applications," Postgraduate diploma assay, May 2010, African Institute for Mathematical Sciences AIMS.

[105] H. C. Yang, "SQUID: The most sensitive detector of magnetic flux," *Tamkang Journal of Science and Engineering*, vol. 6, no. 1, 2003.

[106] K. K. Likharev, "Superconducting weak links," *Reviews of Modern Physics*, vol. 51, no. 1, pp. 101–159, 1979.

[107] P. W. Anderson and A. H. Dayem, "Radio-frequency effects in superconducting thin film bridges," *Bell Telephone Laboratories, Murray Hill, New Jersey*, vol. 13, no. 6, pp. 195 – 197, 1964.

[108] L. Aslamanov and A. Larkin, "Josephson effect in wide superconducting bridges," *L. D. Landau Theoretical Physics Institute, USSR Academy of Sciences*, vol. 68, pp. 766–775, 1975.

[109] H. U. Habermeier et al., "Y-Ba-Cu-O high temperature superconductor thin film preparation by pulsed laser deposition and rf sputtering: a comparative study," *Physica C*, vol. 180, pp. 17 – 25, 1991.

[110] H. Y. Zhai, Z. H. Zhang, and W. K. Chu, "Accurate comparative measurement of oxygen content variations in $YBa_2Cu_3O_{7-\delta}$ films due to postdeposition annealing," *Applied Physics Letters*, vol. 78, no. 5, pp. 649 – 651, January 2001.

[111] L. H. Snetler, "High-temperature superconductor step-edge fabrication for the implementation of RSFQ circuits," Master's Thesis, University of Stellenbosch, April 2005.

[112] M. Mapar et al., "Fabrication of DC SQUID for MEG/MRI application," *Chalmers University of Technology*, no. 12, 2008.

[113] S. H. Liao et al., "A study of J-coupling spectroscopy using the earth's magnetic field nuclear magnetic resonance inside a laboratory," *Review of scientific instruments*, vol. 81, pp. 1 – 6, 2010.

[114] R. D. Venook et al., "Prepolarized magnetic resonance imaging around metal orthopedic implants," *Magnetic Resonance in Medicine*, vol. 56, pp. 117 – 186, 2006.

[115] C. Horch, S. Schlayer, and F. Stallmach, "Permanent magnet arrangements for low-field NMR," in *Excerpt from the Proceedings of the COMSOL Conference.*

[116] P. J. McDonald, *Food Processing: Recent Developments.* Elsevier Science B.V., 1995, ch. The use of nuclear magnetic resonance for on line process control and quality assurance.

[117] M. Maiwald et al., "Quantitative high-resolution on-line NMR spectroscopy in reaction and process monitoring," *Journal of Magnetic Resonance*, vol. 166, pp. 135 – 146, 2004.

[118] M. Abdollahi and M. Sharifpour, "A new simple procedure to calculate monomer reactivity ratios by using on-line ^1H NMR kinetic experiments: Copolymerization system with greater difference between the monomer reactivity ratios," *Polymer communication*, vol. 48, pp. 25 – 30, 2007.

[119] N. Hernandez-Sanchez, P. Barreiro, M. Ruiz-Altisent, J. Ruiz-Cabello, and M. Fernandez-Valle, "Detection of freeze injury in oranges by magnetic resonance imaging of moving samples," *Applied Magnetic Resonance*, vol. 26, pp. 431 – 445, 2004.

[120] N. Hernandez-Sanchez, P. Barreiro, and J. Ruiz-Cabello, "On-line identification of seeds in mandarins with magnetic resonance imaging," *Biosystems Engineering*, vol. 95, no. 4, pp. 529 – 536, 2006.

[121] W. Chayaprasert and R. Stroshine, "Rapid sensing of internal browning in whole apples using a low-cost, low-field proton magnetic resonance sensor," *Postharvest Biology and Technology*, vol. 36, pp. 291 – 301, 2005.

[122] J. R. Sims et al., "Low-noise pulsed pre-polarization magnet systems for ultra-low field NMR," *IEEE Transactions on Applied Superconductivity*, vol. 20, no. 3, pp. 752 – 755, 2010.

[123] C. Kegler, H. Seton, and J. Hutchison, "Prepolarized fast spin-echo pulse sequence for low-field MRI," *Magnetic Resonance in Medicine*, vol. 57, pp. 1180 – 1184, 2007.

[124] C. Yang and Chen, *High-sensitivity Low-field NMR System SQNMR-I: Operation and Maintenance Manual*, www.magqu.com, 03 2012.

[125] C. A. Eustace and R. B. Jordan, "Sugar content evaluation using earth's field proton magnetic resonance," *Transactions of the ASABE*, vol. 38, pp. 1563 – 1571, 1995.

[126] P. Chen, M. J. McCarthy, S. M. Kim, and B. Zion, "Development of a high-speed NMR technique for sensing maturity of avocados," *Transaction of the ASAE*, vol. 39, no. 6, pp. 2205–2209, 1996.

[127] B. P. Hills and K. M. Wright, "Motional relativity and industrial NMR sensors," *Journal of Magnetic Resonance*, vol. 178, pp. 193 – 205, 2006.

[128] A. J. Charlton, "The food sector and nuclear magnetic resonance spectroscopy," *Food and Environment Research Agency, Department for Environment, Food and Rural Affairs, issue one*, pp. 9 – 12, 2010.

[129] "Practical aspects of quantitative NMR experiments."

[130] K. ali, F. Maltese, A. M. Fortes, M. S. Pais, R. Verpoorte, and Y. H. Choi, "Pre-analytical method for NMR-based grape metabolic fingerprinting and chemometrics," *Analytica Chimica Acta*, pp. 1–8, 2011.

[131] K. Ali et al., "Monitoring biochemical changes during grape berry development in portuguese cultivars by NMR spectroscopy," *Food Chemistry*, vol. 124, pp. 1760 – 1769, 2011.

[132] G. Helms, "The principles of quantification applied to in vivo proton MR spectroscopy," *European Journal of Radiology*, vol. 67, pp. 218–229, Feb 2008.

[133] G. Pereira et al., "^1H NMR metabolic fingerprints of grape berries produced in different plots in Bordeaux, France," in *Proc. VIIthIS on Grapevine*, E. L. E. Williams, Ed., vol. 689. Acta Hort, 2005, pp. 257 – 263.

[134] G. E. Pereira, J.-P. Gaudillere, and C. van Leeuwen, "^1H NMR metabolite fingerprints of grape berry: Comparison of vintage and soil effects in Bordeaux grapevine growing areas," *Analytica Chimica Acta*, vol. 563, pp. 346–352, 2006.

[135] G. E. Pereira and J.-P. Gaudillere, "^1H NMR and chemometrics to characterize mature grape berries in four wine-growing areas in Bordeaux, France," *J. Agric. Food Chem.*, vol. 53, pp. 6382 – 6389, 2005.

[136] A. Cazor et al., "Sucrose, glucose, and fructose extraction in aqueous carrot root extracts prepared at different temperatures by means of direct NMR measurements," *J. Agric. Food Chem.*, vol. 54, pp. 4681 – 4686, 2006.

[137] G. Mulas et al., "NMR analysis of seven selections of Vermentino grape berry: Metabolite composition and development," *J. Agric. Food Chem.*, vol. 59, pp. 793–802, 2011.

[138] G. E. Pereira, J. P. Gaudillere, and P. Pieri, "Microclimate influence on mineral and metabolic profiles of grape berries," *Journal of Agricultural and Food Chemistry*, vol. 54, pp. 6765–6775, 2006.

[139] "http://NMRshiftdb.NMR.uni-koeln.de/."

[140] H. K. Kim and R. Verpoorte, "Sample preparation for plant metabolomics," *Phytochemical Analysis*, vol. 21, pp. 4 – 13, 2010.

[141] "Q-NMR-based metabonomics of blood samples," http://www.asdlib.org/onlineArticles/ecourseware/Larive/qNMR7.htm.

[142] T. S. Al-Deen, "Validation of quantitatie nuclear magnetic resonance(QNMR) sectroscopy as a primary ratio analytical method for assesing the purity of organic compounds: A metrological approach," Ph.D. dissertation, School of Chemical Sciences, Analytical Department, University of New South Wales, September 2002.

[143] F. Malz and H. Jancke, "Validation of quantitative NMR," *Journal of Pharmaceutical and Biomedical Analysis*, vol. 38, pp. 813 – 823, 2005.

[144] K. Hu, J. J. Ellinger, R. A. Chylla, and J. L. Markley, "Measurement of absolute concentrations of individual compounds in metabolite mixtures by gradient- selective time-zero $^{1}H-^{13}C$ HSQC with two concentration references and fast maximum likelihood reconstruction analysis," *Analytical Chemistry*, vol. 83, pp. 9352 – 9360, 2011.

[145] S. Ablett, "Overview of NMR applications in food science - review," *Trends in Food Science and Technology*, vol. 3, pp. 246 – 260, 1992.

[146] J. Brand, "Personal communication," Tecnical conversation: SQNMR system demonstration, 20 April 2012.